Modeling Interactions of Graphene with Electrolyte in the Field-Effect Transistor Configuration

by

Puneet Sharma

A thesis
presented to the University of Waterloo
in fulfillment of the
thesis requirement for the degree of
Doctor of Philosophy
in
Applied Mathematics

Waterloo, Ontario, Canada, 2015

Author's Declaration

I hereby declare that I am the sole author of this thesis. This is a true copy of the thesis, including any required final revisions, as accepted by my examiners.

I understand that my thesis may be made electronically available to the public.

Abstract

Understanding interactions of graphene with an electrolyte is fundamental to its applications for chemical and biological sensors, where graphene operates in the configuration of a field-effect transistor with its surface exposed to liquid containing mobile ions. By applying a gate potential through an electrolyte one may achieve a control of graphene's conductivity that is extremely sensitive to the presence of adsorbed molecules, ion concentration, or the pH in an aqueous solution. In addition, charged impurities in the oxide layer underneath graphene also affect its conductivity by causing fluctuations of the scattering potential for charge carriers in graphene. Since the gate potential used for graphene doping in such applications is usually large, it is necessary to consider nonlinear effects in the equilibrium doping of graphene using a full density of states for its π-electron bands, while in the electrolyte it is necessary to assess the effects due to finite size of ions and dielectric saturation of water near highly doped graphene.

We first explore the capacitance of a graphene-electrolyte interface using well established continuum models from electrochemistry that generalize the Poisson-Boltzmann (PB) theory: the Bikerman model for steric effects due to ion size and the Booth model for dielectric saturation. Next, we develop a model to describe the screening of the electrostatic potential that arises in the plane of graphene due to charged impurities in the oxide. For the polarizability of charge carriers in graphene we explore two models, one based on the Thomas-Fermi approximation and the other based on the Random Phase approximation for graphene's π-electron bands in the Dirac cone approximation. On the other hand, the ion distribution in the electrolyte is described by a fully linearized PB model known as Debye-Hückel PB (DHPB) model, which is suitable for a low gating potential, as well as by a partially linearized PB (PLPB) model, which contains full information on the equilibrium gating conditions of graphene. The screened potential due to charged impurities is described by a dielectric response formulation of the problem, which is derived from the Green's function for the Poisson equation for the entire structure containing graphene. Statistical properties of the fluctuations in the potential are analyzed by means of its auto-correlation function, which is expressed in terms of a structure factor for the geometric positions of charged impurities in the oxide.

We have found that for the gate potentials $\lesssim 1$ V, which are of interest in most graphene applications, the total capacitance is dominated by the quantum capacitance of graphene. Moreover, we have found that the capacitance of the electric double layer in the electrolyte may be adequately described for the same range of gate potentials $\lesssim 1$ V by using the PB model in its standard, nonlinear form, without the need of additional modifications. Furthermore, we have confirmed that the PLPB model yields the doping density of graphene and the potential drop across the diffuse layer, with better accuracy and in a broader range of values of the external parameters than the DHPB model. We have found that both the DHPB and the PLPB models exhibit a very weak dependence on ion concentration for both the auto-correlation and variance of the potential when compared to the uncorrelated charged impurities.

Last but not least, results reported in this thesis are geared towards the first stage of a long-term undertaking to develop a comprehensive and computational model for biological and chemical sensors in the context of graphene based field-effect transistors.

Acknowledgements

I am especially thankful to my PhD supervisor Professor Z. L. Mišković whose continuous support, help, and guidance made it possible to achieve this milestone in my life. I'll always remain indebted to him for being a wonderful mentor. My heartfelt thanks goes to Late Professor F. O. Goodman, who left us during the course of this program, for teaching the best tactics for coding techniques. Special thanks to my PhD Committee members, Professor Matthew Scott, Professor Mohammad Kohandel and Professor Wing-Ki Liu and my external examiner, Professor Mahi R. Singh.

A very special thanks to my better half, Riddhi Sharma, and my sweetest daughters, Saumya Sharma and Shreeya Sharma for their indomitable love and support. I am grateful to my all family members including Raj Kumari, Varinder Sharma, Kavita Sandhir, Poonam Sharma, Ashish Vashisht, Priyanka Vermani, and Kapil Vermani, for their unconditional love throughout the journey. I am thankful to my all teachers, colleagues, students, and friends, living in Canada and abroad, for keeping me in high spirits for the success of this project.

In addition, I would also like to express appreciation to Dr. Tankeshwar Kumar, Dr. Arvinder Singh, Dr. Rohan Kaushal, Dr. Andree Susanto, Subasha Wickramarachchi, Shivang Vyas, Kunal Sonone, Yingying Zhang, Keenan Lyon, Naijing Kang, and Vivek Thampi, for their valuable advice in my research and for all the joy they brought.

With all humbleness, I am thankful to Almighty for making this venture successful and giving me strength to keep it up.

Dedication

In the memory of my beloved father, Parmod Kumar Sharma

Table of Contents

List of Figures

List of Acronyms

1D	One-dimensional
2D	Two-dimensional
BC	Boundary condition
BF	Bikerman-Freise
DH	Debye-Hückel
DHPB	Debye-Hückel Poisson-Boltzmann
DL	Diffuse layer
DOS	Density of states
DS	Dyson-Schwinger
EDL	Electrostatic double layer
FET	Field effect transistor
FT	Fourier transform
FTGF	Fourier transform of the Green's Function
GB	Grahame-Booth
GBBF	Grahame-Booth-Bikerman-Freise
GC	Gouy-Chapman
GF	Green's Function
HD	Hard disc
ISFET	Ion-sensitive field effect transistor
MC	Matching condition
MPB	Modified Poisson-Boltzmann
PB	Poisson-Boltzmann
PDE	Partial differential equation
PLPB	Partially linearized Poisson-Boltzmann
QC	Quantum capacitance
RPA	Random Phase Approximation
SL	Stern Layer
TF	Thomas-Fermi

Chapter 1

Introduction

1.1 Graphene: an outstanding material and an ultimate destiny of nano research and applications

Graphene, one of the allotropic forms of carbon, is a smooth single layer of sp^2 bonded carbon atoms densely packed into a honeycomb crystal lattice. Graphene is a fundamental integrant of the other forms of carbon including carbon nanostructures such as buckyballs and carbon nanotube, and graphite. In 1947 [6], Professor P. R. Wallace, a prominent Canadian theoretical physicist, was a pioneer to apply tight binding approximation in the band theory of solids to investigate the electronic properties of three dimensional graphite, in addition to underlying theory of graphene, the subject of 2010 Nobel prize in Physics. He demonstrated an astonishing semimetallic behavior of graphene due to a linear dispersion relation of energy to the crystal momentum in the graphene lattice in the Dirac cone regime, which is explained in chapter 2.

Carbon nanostructures are currently studied with an increased focus on their applications as biological and chemical sensors [7, 8, 9]. In particular, graphene-based devices are typically operated for such applications in the regime of a field effect transistor (FET) with the surface of graphene exposed to an electrolyte containing mobile charges [10, 11]. In that respect, graphene-based FETs show great promise for biochemical sensor design in comparison to the more traditional devices based on the electrolyte-insulator-semiconductor FETs [12]. It was recently demonstrated by Tao *et al.* [13] that the current through a graphene FET may be much more efficiently controlled by an electrochemical gate immersed in the electrolyte than by a metallic back gate applied though a few hundred nanometers thick insulating layer of SiO_2, which is typically used for electronics applications of graphene [14].

The top gating of a graphene based FET with a liquid electrolyte presents several advantages compared to the conventional back gating with a metallic electrode. Among the many possible types of solvents that are currently used in graphene electrochemistry

[15], particularly important for biomedical applications is the interaction of graphene with aqueous solutions [11]. It is well known that application of the gate voltage through an aqueous electrolyte causes a redistribution of ions dissolved in water, which gives rise to an electrostatic double layer (EDL) at the interface between graphene and the electrolytic solution [16]. Depending on the ion concentration, the EDL may only be a few nanometers thick, while still providing efficient shielding of the graphene channel. As a consequence, the capacitance of the EDL in an electrolyte can be much higher than the capacitance of a typical metallic back gate [13, 14]. This property of the EDL enables a much better control of the surface potential on the graphene layer, while requiring a much lower operating voltage that needs to be applied to the reference electrode in the electrolyte than voltages currently used with back gates. The applied voltage then modifies the chemical potential of graphene and hence changes its conductance in a manner that can be used in a transistor mode, e.g., for detecting the amount of salt or the pH in the solution [17, 18].

On the other hand, it was recently demonstrated that operating a graphene field effect device in the capacitor mode exhibits more sensitivity to variations in both the ion concentration and the pH of an aqueous solution of salt than operating such device in the transistor mode [19]. This is related to the well-known fact that, when a semimetal such as graphite [20] or the conductive single crystalline diamond [21, 22] are used as electrodes in an aqueous electrolyte, the overall capacitance of the EDL is dominated by the so-called quantum capacitance (QC) of such electrodes, which is in contrast to the case of an ideal metallic electrode [16]. The QC of a single-layer graphene [23] was first measured by Xia *et al.* in an ionic liquid and in an aqueous solution of salt [24]. Some of the more recent studies of the graphene QC in aqueous solutions involve a correlated *in situ* electrochemical Raman spectroscopy [25], as well as charging of graphene through a biological ion channel in a lipid bilayer adjacent to graphene [26], showing the versatility and the promise of operating graphene devices in the capacitor mode. It is noteworthy that most of the above mentioned studies of solution-gated graphene devices have achieved quite high doping densities of graphene by both electrons and holes, reaching the range of 10^{13} to 10^{14} cm^{-2}.

Research communities in Physics, Chemistry and Engineering are working at a relentless pace to explore prospects that graphene may replace silicon-based-electronics in the new era of nanometer sized devices. While most researchers are concerned with graphene's conducting properties, which sometimes appear quite exotic from the perspective of Condensed Matter theory, this thesis is designed to explore a more inter-disciplinary approach at the interface between Physics and Electrochemistry with an outlook on applications of graphene based FETs as chemical and biological sensors. Results reported in this thesis represent the first stage of a long-term program to develop a comprehensive mathematical and computational model for these sensors, which will address several problems, including nonlinear effects in the electrolyte and graphene, the effects of disorder on the conductivity and capacitance of graphene, and its sensitivity to chemical reactions taking place at the interface with electrolyte. While those phenomena are characterized by an equilibrium regime of the graphene-electrolyte interface, next stages of such program will include dy-

namic regime dealing with electrokinetic processes due to ion flow in the electrolyte, and ultimately the effects of electrolyte on plasmon excitation in graphene for applications in nano-plasmonic sensors based on graphene.

1.2 Description of the results presented in the thesis

Efforts in theoretical modeling of the solution-gated graphene still lag behind the experiments. It is surprising that there are only few reports of such kind [27, 28, 29, 30, 31, 32, 33, 34], especially in view of the recent progress in mathematical modeling of strongly coupled soft matter, [35] electrokinetic phenomena, [3] and ionic liquids [36], which treat the electrolyte as a dielectric continuum. Perhaps part of the reason for this lack of theoretical modeling is due to the fact that, unlike the metallic or semiconducting electrodes that are typically considered in the standard electrochemical models [3, 35], single-layer graphene is a truly two-dimensional (2D) semi-metal, or a zero-gap semiconductor with a relatively poor screening ability, so that its surface electrostatic potential and its surface charge density may vary quite strongly with the concentration of both the mobile ions in the electrolyte and the fixed charged impurities. In that respect, my first work on graphene interaction with an electrolyte, which is described in Chapter 6, was devoted to studying the ion-assisted screening of charged impurities in an oxide substrate for electrolytically top-gated graphene [37] by treating the EDL as composed of a diffuse layer (DL) of ions and the so-called compact, or Helmholtz, or Stern layer (SL) between the DL and graphene [30]. Assuming that the ion concentration and the gate potential are not too high, we described the DL by the standard Debye-Hückel (DH) model [16], whereas the charge-free SL was treated as a phenomenological means to take into account, at least partially, the effects of non-zero size of hydrated ions in the electrolyte, also known as steric effects, as well as the dielectric saturation of water (or other polar solvent) in the possibly high electric fields close to graphene [3]. At the same time, we described the polarization of doped single-layer graphene by means of a full static dielectric function in the random phase approximation at non-zero temperature with graphene's π electron bands treated in the Dirac cone approximation [1, 38, 39].

In the DH model of the EDL, the distribution of mobile ions in the electrolyte is described by the linearized Poisson-Boltzmann (PB) equation, which enables a straightforward solution of the equations for the electrostatic potential in the entire structure, consisting of a metallic back gate, oxide layer, graphene, SL, and DL. Taking advantage of the linearized PB equation, we have adopted a mathematical formulation of the screening process by means of an effective dielectric function, which we deduce from the Green's function (GF) for the Poisson's equation. This approach is particularly suitable for a layered structure with large area, whose dielectric properties change in a jump-like manner at planar boundaries between layers with different material properties. Using a two-dimensional (2D) Fourier transform (FT) with respect to positions parallel to those boundaries reduces the Poisson equation to an ordinary differential equation which is easily solved in a piece-

wise manner by imposing the usual electrostatic boundary and matching conditions at the interfaces between neighbouring layers. In addition, assuming that graphene is represented by a zero-thickness sheet of charge with the surface density that is determined by the value of the potential in the plane of graphene proved advantageous by introducing graphene into the jump condition for the potential. Working in the 2DFT domain then allowed us to use a linear-response relation between the charge density and the potential in graphene via its polarization function, or polarizability, transforming the jump condition for the potential into a Robin type boundary (matching) condition. Moreover, the zero-thickness assumption for graphene facilitates efficient use of the Dyson-Schwinger equation for the GF of the Poisson equation, enabling us to express the GF of the entire structure *with* graphene in terms of graphene's polarizability and the GF of the same structure *without* graphene. Needless to say, this gives us great deal of flexibility in being able to use analytical expressions for the GF for layered structures with various degrees of complexity, where we can introduce one or more layers of graphene in an algebraically straightforward manner.

However, for the most of bioelectronics and sensing applications of graphene, it is of interest to consider solution-gated devices at high gate potentials and/or high ion concentration in the electrolyte, which casts serious concerns about the applicability of the DH model, or the linearized PB equation for the distribution of mobile ions in the electrolyte. This prompted my second work, which is described in Chapter 5, dedicated to exploring the interaction of graphene with an electrolyte in such extreme regimes by resorting to electrochemical models based on mean-field theories that treat the electrolyte as a dielectric continuum [3, 36]. If one may disregard specific adsorption of ions, e.g., by choosing an aqueous solution of NaF [16], one may expect that the so-called crowding of counterions will take place close to a highly charged surface of graphene, so that the steric effects in the EDL may become prominent. It was shown recently that the so-called Bikerman-Freise (BF) model for the EDL [3, 40, 41] is quite capable of describing the steric effects in electrolytes at high gate potentials [42] and in ionic liquids [43] at the level of a modified Poisson-Boltzmann (MPB) theory. In an attempt to go beyond the mere use of a SL in modeling the electrolytically top-gated graphene, the BF model was recently adopted to study the interplay between the quantum capacitance (QC) of graphene and the saturation in the EDL capacitance due to ion crowding close to a highly charged graphene surface [29].

On the other hand, the effect of dielectric saturation of a polar solvent due to partial locking of the rotational degrees of its molecular dipoles in the presence of high electric fields close to a highly charged surface is more difficult to describe within a mean-field theory [3]. Despite the recent efforts to derive a dielectric continuum model that will take the dielectric saturation of solvent and the effects of finite ion sizes on equal footing [44, 5], it appears that old models, such as Grahame's phenomenological formula [3, 45] and the Booth model [46] may provide satisfactory description for dielectric saturation of water and other polar solvents [47, 48, 49, 50]. In particular, the Booth model was found to fit the results of a molecular dynamics simulations of dielectric constant of water at high

electric fields [51], and was recently used to discuss the dielectric saturation of water in a membrane protein channel [50]. Moreover, the Booth model was recently combined with the BF model for steric effects to discuss the hydration repulsion between charged surfaces [49] and to conduct accurate simulations of the EDL capacitance of mesoporous electrodes [47] and ultramicroelectrodes [48].

Motivated by those developments, and in order to address the need to better understand the interaction of graphene with an electrolyte under high gating potential and with high ion concentration for possible biomedical sensor applications, we discuss in Chapter 5 the capacitance of a solution-gated graphene by combining the Booth model for dielectric saturation and the BF model for steric effects. We formulate a one-dimensional (1D), mean-field model for a graphene sheet of large area that is both back-gated by the standard metallic gate with a thick insulating oxide layer and top-gated through a thick layer of an aqueous solution. We allow for the existence of a SL with a simplified model for specific adsorption of ions at the inner Helmholtz plane that is moved to coincide with the outer Helmholtz plane, or Stern plane positioned at the boundary between the SL and DL [3]. While such formulation permits a more detailed study of the capacitance for a complex layered structure, we limit our numerical examples to just considering the top-gated regime without the SL and neglecting the specific adsorption. However, we expect that our description of the DL, which is in direct contact with graphene, by combining the Booth model with the BF model can provide a qualitatively correct picture of the main effects of a high gate potential and high ion concentration on the interplay between the graphene QC and the EDL capacitance in an aqueous electrolyte.

In my third work on graphene interaction with electrolyte, described in Chapter 7, we went back to the problem of ionic screening of charged impurities in the presence of doped graphene in order to relax the approximation made in the DH model of the electrolyte, while keeping the elegance and versatility of the GF method for the electrostatic potential. The key step was to use the so-called partially linearized PB equation, where both the electrostatic potential and the charge density in the structure is decomposed into an average part and a fluctuating part. The surface averaging leaves only the dependence on the coordinate perpendicular to the layered structure, for which a fully nonlinear PB equation may be solved analytically in the DL. When coupled with the nonlinear expression for the equilibrium charge density in doped graphene, the solution of the nonlinear PB equation yields a pair of transcendental equations that may be solved to give a more realistic density of mobile ions in the DL than in the DH model, as well as the equilibrium charge density in graphene in terms of an arbitrary combination of the external parameters, such as the top and/or back gate potential(s) and the average density of charged impurities in the oxide. It is important to have a reliable model for this complex gating process of graphene because its equilibrium charge density controls the conductivity of graphene in sensing measurements and it enters as a defining parameter in the expression for its polarizability, which characterizes the screening properties of graphene.

On the other hand, the resulting PB equation for the fluctuating part of the potential also includes the fluctuating part of charge density due to the randomness in the positions of

charged impurities in the oxide. Our goal is to provide a stochastic analysis of the resulting fluctuations of the potential in the plane of graphene because those fluctuations play an important role in the conductivity of graphene, which is a key quantity in the sensing measurements. Assuming that those fluctuations are small, we linearize the PB equation for the fluctuating potential about the known solution of the nonlinear PB equation for the averaged potential. As a result, we obtain a linear ordinary differential equation in the 2DFT domain with a non-constant coefficient in the DL. Fortunately, an analytical solution of that equation is available enabling us to construct, in a piece-wise manner, a full GF for the entire structure, which contains full dependence on the external parameters. This formulation of the problem allows us to express the screened potential in graphene by means of an effective dielectric function of the entire structure, as well as to express the auto-correlation function for the fluctuations in that potential due to randomness in the positions of charged impurities by means of a geometric structure factor.

Because the electronic structure of graphene, as well as its dielectric polarization are important ingredients in the models described in chapters 5-7, I shall review some known results for graphene in Chapters 2 and 3. In addition, since I use models from electrochemistry that describe ionic solution as a dielectric continuum, I shall review in Chapter 4 several established models that address various regimes of the polarization of mobile ions in an EDL.

Note that, unless otherwise explicitly stated in this thesis, we use gaussian electrostatic units where $4\pi\epsilon_0 \equiv 1$, with ϵ_0 being the dielectric permittivity of vacuum.

Chapter 2

Electronic Structure of Graphene

2.1 Crystal structure of graphene

Graphene is one of the allotropic forms of carbon that is formed by a two dimensional honeycomb crystal lattice. It has two carbon atoms per primitive cell which is repeated periodically throughout the lattice. The two types of atoms are labeled as A and B. The inter-atomic distance between the nearest atoms in the lattice is approximately $a = 1.42$ Å[1]. Fig. 2.1 shows a small portion of the crystal structure of graphene.

Using simple geometrical arguments, the Bravais lattice of graphene is formed by two vectors

$$\mathbf{a}_1 = \frac{a}{2}(3, \sqrt{3}), \tag{2.1}$$

$$\mathbf{a}_2 = \frac{a}{2}(3, -\sqrt{3}). \tag{2.2}$$

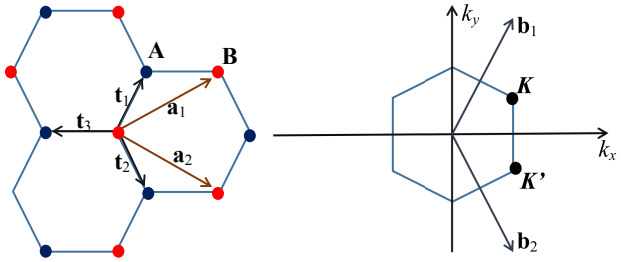

Figure 2.1: (Left) Graphene's crystal structure. The unit cell comprises the two atoms, A and B. The Bravais lattice is formed by repeating the structure of the unit cell using the vectors $\mathbf{a}_1$ and $\mathbf{a}_2$. Vectors $\mathbf{t}_1$,$\mathbf{t}_2$, and $\mathbf{t}_3$ determine the location of the nearest neighbour atom sites. (Right) The first Brillouin zone of the graphene lattice. Vectors $\mathbf{b}_1$ and $\mathbf{b}_2$ denote the reciprocal lattice vectors. Adapted from [1]

These translational vectors, which connect atoms of the same type, define the crystal structure of graphene. A single atom of type B is connected to three nearest neighbour atoms, which are of the type A, and vice versa. The transitional vectors connecting the nearest neighbour atoms may be determined using the same geometric arguments as

$$\mathbf{t}_1 = \frac{a}{2}(1, \sqrt{3}), \tag{2.3}$$

$$\mathbf{t}_2 = \frac{a}{2}(1, -\sqrt{3}), \tag{2.4}$$

$$\mathbf{t}_3 = -a(1, 0). \tag{2.5}$$

Taking into account the vectors that form the Bravais lattice, we may determine the reciprocal lattice as

$$\mathbf{b}_1 = \frac{2\pi}{3a}(1, \sqrt{3}), \tag{2.6}$$

$$\mathbf{b}_2 = \frac{2\pi}{3a}(1, -\sqrt{3}), \tag{2.7}$$

which may be used to construct the first Brillouin zone as shown in Fig. 2.1.

2.2 Tight binding calculations

We want to evaluate the energy dispersion relation for electrons in graphene using the tight binding approximation. Since graphene is a two-dimensional honeycomb lattice formed from carbon atoms we examine the structure of the carbon atom first. Each carbon atom consists of six electrons, two of which occupy the deepest lying 1s electron orbitals. They are screened from external fields by the remaining four electrons in the 2s and 2p orbitals. Since the two 1s electrons are tightly bound to the carbon atom and have limited mobility throughout the lattice, they play no role in the electrical properties of graphene, one may ignore them. The remaining four valence electrons in the $n = 2$ shell have very similar energies, so that their orbitals hybridize, forming a superposition of electron orbitals. For a proper tight binding calculation we should include all four $n = 2$ orbitals (2s, $2p_x$, $2p_y$, $2p_z$) in the wavefunction. Since the graphene lattice forms a periodic potential that enters the electronic Hamiltonian, the resulting wavefunction $\psi_{\mathbf{k}}(\mathbf{r})$ must satisfy the Bloch's theorem [52]. This theorem states that for a periodic structure, electronic eigenfunctions must have the form

$$\psi_{\mathbf{k}}(\mathbf{r}) = e^{i\mathbf{k}\cdot\mathbf{r}} u_{\mathbf{k}}(\mathbf{r}), \tag{2.8}$$

where $u_{\mathbf{k}}(\mathbf{r})$ is a periodic function which has the same period as the Bravais lattice, and $\mathbf{k}$ is the crystal momentum, which labels the electronic states inside each energy band.

Since there are two atoms per primitive cell of the Bravais lattice, each containing four $n = 2$ electron orbitals, the Bloch wavefunction for graphene consists of a summation of 8 terms over all Bravais lattice vectors $\mathbf{R}$,

$$\psi_{\mathbf{k}}(\mathbf{r}) = \sum_{\mathbf{R}} e^{i\mathbf{k}\cdot\mathbf{R}} \Big(b_{As}\Upsilon_{As} + b_{Ap_x}\Upsilon_{Ap_x} + b_{Ap_y}\Upsilon_{Ap_y} + b_{Ap_z}\Upsilon_{Ap_z} + b_{Bs}\Upsilon_{Bs} + b_{Bp_x}\Upsilon_{Bp_x} + b_{Bp_y}\Upsilon_{Bp_y} + b_{Bp_z}\Upsilon_{Bp_z} \Big), \tag{2.9}$$

Here Υ_{As}, Υ_{Ap_x}, etc. are the hydrogenic orbital wavefunctions [53]) centered at the site A in the primitive cell, and similarly for Υ_{Bs}, Υ_{Bp_x}, etc. that are centered at the site B. (To simplify the notation we have dropped the $\mathbf{r}$ and $\mathbf{R}$ dependence from the hydrogenic orbital wavefunctions). The wavefunction in Eq. (2.9) forms 8 energy bands for each $\mathbf{k}$ in the first Brillouin zone. Further analysis of the energy dispersion may be simplified by considering detailed structure of the electron orbitals in graphene. Each carbon atom in graphene forms strong chemical bonds to the three neighbouring carbon atoms. Those bonds are formed by mixing (hybridization) of the s, p_x and p_y orbitals on each atom giving rise to strong covalent bonds between the carbon atoms, known as σ bonds, which are responsible for the mechanical strength of graphene. Such mixed orbital state is called sp^2 hybridization because one s orbital mixes with two p orbitals to form a two dimensional hybrid orbital in the $x - y$ plane. The sp^2 orbital states give rise to six σ-bonding energy bands in the first Brillouin zone, three of them being the conduction and three the valence bands. The σ-bonding bands have a very large energy gap between the conduction and valence bands and by having the Fermi energy in neutral graphene lie between those two groups of bands, they do not contribute much to the electrical properties of graphene near the ground state. So, we neglect the σ-bands in our tight binding calculations, but note that a detailed analysis is given elsewhere [54].

The remaining p_z orbitals are well separated from the sp^2 hybridized orbitals, both spatially and energetically, and they form the valence and conduction π-bonding bands in graphene. Those two π-bands give rise to the unique electronic properties of graphene, which have attracted so much attention in recent years. It is interesting that the tight binding calculations that deal with the p_z orbitals and the π-bonding bands were first performed by a prominent Canadian physicist, P.R. Wallace, at the famous Chalk River Laboratory in Ontario almost 70 years ago [6] !

Dropping the atomic wavefunctions that contribute to the sp^2 orbitals, we may write the wavefunction as a linear combination of p_z orbitals on sites A and B,

$$\psi_{\mathbf{k}} = a_{\mathbf{k}}\psi_{A,\mathbf{k}} + b_{\mathbf{k}}\psi_{B,\mathbf{k}}. \tag{2.10}$$

Here $\psi_{A,\mathbf{k}}$ and $\psi_{B,\mathbf{k}}$ are the Bloch wavefunctions for the p_z orbitals located on sites A and B, respectively, which are defined as

$$\psi_{A,\mathbf{k}}(\mathbf{r}) = \frac{1}{\sqrt{N}} \sum_{\mathbf{R}} e^{i\mathbf{k}\cdot\mathbf{R}}\ \Upsilon_{Ap_z}(\mathbf{r} - \mathbf{R}). \tag{2.11}$$

where $\mathbf{R}$ are the Bravais lattice vectors for the atoms on site A, and N is the number of unit cells. We may similarly define $\psi_{B,\mathbf{k}}$ by summing over Bravais lattice vectors on site B. We may now find the energy as a function of $\mathbf{k}$ from the Schrodinger equation written in matrix form as

$$\begin{bmatrix} \langle \psi_{A,\mathbf{k}}|H|\psi_{A,\mathbf{k}}\rangle & \langle \psi_{B,\mathbf{k}}|H|\psi_{A,\mathbf{k}}\rangle \\ \langle \psi_{B,\mathbf{k}}|H|\psi_{A,\mathbf{k}}\rangle & \langle \psi_{B,\mathbf{k}}|H|\psi_{B,\mathbf{k}}\rangle \end{bmatrix} \begin{bmatrix} a_{\mathbf{k}} \\ b_{\mathbf{k}} \end{bmatrix} = \varepsilon \begin{bmatrix} \langle \psi_{A,\mathbf{k}}|\psi_{A,\mathbf{k}}\rangle & \langle \psi_{B,\mathbf{k}}|\psi_{A,\mathbf{k}}\rangle \\ \langle \psi_{B,\mathbf{k}}|\psi_{A,\mathbf{k}}\rangle & \langle \psi_{B,\mathbf{k}}|\psi_{B,\mathbf{k}}\rangle \end{bmatrix} \begin{bmatrix} a_{\mathbf{k}} \\ b_{\mathbf{k}} \end{bmatrix}. \quad (2.12)$$

Here H is one-electron Hamiltonian of the graphene's atomic lattice, which is not known but its matrix elements may be approximated in the basis of the atomic orbital wavefunctions. The diagonal matrix element for the atom of type A may be written as

$$\begin{aligned} \langle \psi_{A,\mathbf{k}}|H|\psi_{A,\mathbf{k}}\rangle &= \frac{1}{N}\sum_{\mathbf{R}} e^{i\mathbf{k}\cdot\mathbf{R}} \iiint d^3\mathbf{r}\ \Upsilon_{Ap_z}(\mathbf{r}-\mathbf{R}) H \Upsilon_{Ap_z}(\mathbf{r}) \\ &= \iiint d^3\mathbf{r}\ \Upsilon_{Ap_z}(\mathbf{r}) H \Upsilon_{Ap_z}(\mathbf{r}) + \sum_{\mathbf{r}_j} e^{i\mathbf{k}\cdot\mathbf{r}_j} \iiint d^3\mathbf{r}\ \Upsilon_{Ap_z}(\mathbf{r}-\mathbf{r}_j) H \Upsilon_{Ap_z}(\mathbf{r}) + \ldots \\ &\approx \varepsilon_{2p} \end{aligned} \quad (2.13)$$

where $\mathbf{r}_j$ are positions of the nearest carbon atoms of type A. Since the distance between neighbouring type A atoms is large enough, all the integrals involving orbitals on different atom sites of type A are negligible, so we neglected them by dropping all the terms after the first one in the second line of Eq. (2.13). To a good approximation, we are left with the on site energy ε_{2p} of the atomic $2p_z$ orbital. The same reasoning gives for the other diagonal element $\langle \psi_{B,\mathbf{k}}|H|\psi_{B,\mathbf{k}}\rangle \approx \varepsilon_{2p}$. The off-diagonal matrix elements may also be obtained in an approximate form by only using nearest neighbour interactions, giving

$$\begin{aligned} \langle \psi_{A,\mathbf{k}}|H|\psi_{B,\mathbf{k}}\rangle &= \sum_{i=1}^{3} e^{i\mathbf{k}\cdot\mathbf{t}_i} \iiint d^3\mathbf{r}\ \Upsilon_{p_z}(\mathbf{r}-\mathbf{t}_i) H \Upsilon_{p_z}(\mathbf{r}) \\ &= \alpha \sum_{i=1}^{3} e^{i\mathbf{k}\cdot\mathbf{t}_i}, \end{aligned} \quad (2.14)$$

where $\mathbf{t}_i$ is one of the three translational vectors defined in Fig. 2.1 and $\Upsilon_{p_z}(\mathbf{r})$ is the atomic $2p_z$ orbital of carbon. In Eq. (2.14) we have introduced its the nearest neighbour coupling strength, or hopping integral between the atoms of type A and B by defining $\alpha = \iiint d^3\mathbf{r}\ \Upsilon_{p_z}(\mathbf{r}-\mathbf{t}_i) H \Upsilon_{p_z}(\mathbf{r})$. Similarly, by using the same nearest neighbour approximation we get the normalization integrals as

$$\langle \psi_{A,\mathbf{k}}|\psi_{A,\mathbf{k}}\rangle = 1, \quad (2.15)$$

$$\langle \psi_{A,\mathbf{k}}|\psi_{B,\mathbf{k}}\rangle = \beta \sum_{i=1}^{3} e^{i\mathbf{k}\cdot\mathbf{t}_i}, \quad (2.16)$$

where $\beta = \iiint d^3\mathbf{r}\ \Upsilon_{p_z}(\mathbf{r}-\mathbf{t}_i)\Upsilon_{p_z}(\mathbf{r})$.

In order to find the energy dispersion relation of graphene we define the auxiliary function

$$f(\mathbf{k}) = \sum_{i=1}^{3} e^{i\mathbf{k}\cdot\mathbf{t}_i}, \tag{2.17}$$

and rewrite the matrix equation in Eq. (2.12) as

$$\left(\begin{bmatrix} \varepsilon_{2p} & \alpha f(\mathbf{k}) \\ \alpha f^*(\mathbf{k}) & \varepsilon_{2p} \end{bmatrix} - \varepsilon \begin{bmatrix} 1 & \beta f(\mathbf{k}) \\ \beta f^*(\mathbf{k}) & 1 \end{bmatrix} \right) \begin{bmatrix} a_{\mathbf{k}} \\ b_{\mathbf{k}} \end{bmatrix} = \begin{bmatrix} 0 \\ 0 \end{bmatrix}. \tag{2.18}$$

To find non-trivial solutions of this system we need to solve the secular equation

$$\det \begin{bmatrix} \varepsilon_{2p} - \varepsilon & (\alpha - \beta\varepsilon) f(\mathbf{k}) \\ (\alpha - \beta\varepsilon) f^*(\mathbf{k}) & \varepsilon_{2p} - \varepsilon \end{bmatrix} = 0, \tag{2.19}$$

which gives the energy dispersion as

$$\varepsilon(\mathbf{k}) = \frac{\varepsilon_{2p} \pm \alpha |f(\mathbf{k})|}{1 \pm \beta |f(\mathbf{k})|}, \tag{2.20}$$

where + denotes the dispersion in the conduction band and - in the valence band. This result is exact when only considering nearest neighbour interactions in the tight binding scheme. An analysis of the graphene dispersion relations beyond the nearest neighbour coupling yields much more cumbersome analytical results [55, 56]. Fortunately, the 2nd nearest neighbour contributions to the energy dispersion are approximately one order of magnitude smaller than those in Eq. (2.20), so it is usually justified to neglect their effect.

Since the Hamiltonian is not known, the exact values for ε_{2p}, α and β are not available. However, they may be approximated from experimental results or from first principle calculations. Currently admissible values of those parameters are $\alpha = 2.7$ eV and $\beta < 0.1$ [55]. The value for β is rather small because it represents the overlap integral between the two p_z electrons orbitals centered at two nearest neighbour atoms separated by a distance 1.42 Å. Hence, it is customary to make an approximation $\beta \approx 0$. Then, the on site energy ε_{2p}, which gives the amount of energy required to ionize a carbon atom, only shifts the energy reference level for our two π-bands, and so we may ignore it by setting $\varepsilon_{2p} = 0$. Thus, to a good approximation, we get for the energy dispersion

$$\begin{aligned} \varepsilon(\mathbf{k}) &= \pm\alpha |f(\mathbf{k})| = \pm\alpha \left| \sum_{i=1}^{3} e^{i\mathbf{k}\cdot\mathbf{t}_i} \right| \\ &= \pm\alpha \sqrt{3 + 4\cos\left(\frac{\sqrt{3}a}{2}k_y\right)\cos\left(\frac{3a}{2}k_x\right) + 2\cos(\sqrt{3}ak_y)}. \end{aligned} \tag{2.21}$$

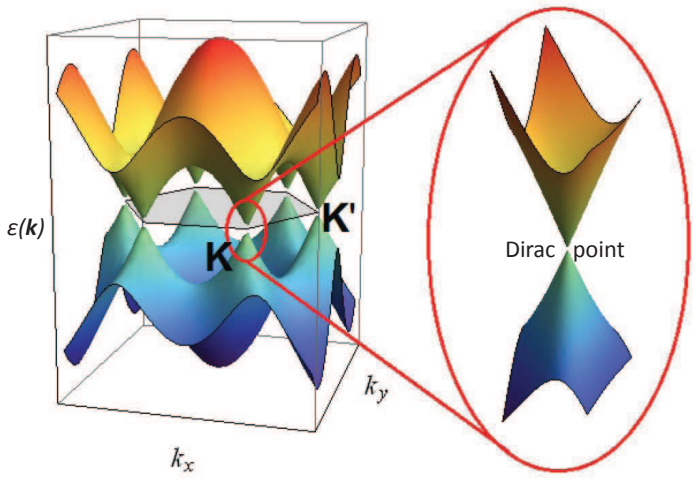

Figure 2.2: Energy dispersion model of graphene within the tight-binding approximation. The 6 symmetric self-crossings in the band energy structure are where the dispersion relation relating energy to the crystal momentum in the graphene lattice are effectively linear, known as the Dirac cone regime. Adapted from [2]

Using this result, we may plot the surfaces representing the energy dispersion in the valence and conduction π-bands in the first Brillouin zone in Fig. 2.2. There are two points labeled $\mathbf{K}$ and $\mathbf{K}'$ in the reciprocal lattice space, which play an important role. They are located at

$$\mathbf{K} = \frac{2\pi}{3a}\left(1, \frac{1}{\sqrt{3}}\right), \tag{2.22}$$

$$\mathbf{K}' = \frac{2\pi}{3a}\left(1, -\frac{1}{\sqrt{3}}\right). \tag{2.23}$$

Those points give the locations where the conduction and valence bands meet, but never intersect, leaving a zero energy gap between the two bands. In a neutral (undoped) graphene the Fermi level is positioned exactly at the energy associated with the points $\mathbf{K}$ and $\mathbf{K}'$ and, since there is negligible density of states at those points, graphene is characterized as a semi-metal, or a zero-gap semiconductor. Furthermore, the energy dispersion near $\mathbf{K}$ and $\mathbf{K}'$ is approximately linearly dependent on the momentum $\mathbf{k}$, which resembles the energy dispersion of a massless particle described by the Dirac equation. Therefore, the points $\mathbf{K}$ and $\mathbf{K}'$ are also called Dirac points. To show the linear dispersion of the energy

near these points, we perform a Taylor expansion of the dispersion equation around the point **K** and keep all the terms up to second order. Defining

$$\begin{aligned} k_x &= K_x + \delta k_x, \\ k_y &= K_y + \delta k_y, \end{aligned} \tag{2.24}$$

gives

$$\begin{aligned} |f(\mathbf{k})|^2 &= 3 + 4\cos\left[\frac{\sqrt{3}a}{2}(K_y + \delta k_y)\right]\cos\left[\frac{3a}{2}(K_x + \delta k_x)\right] + 2\cos[\sqrt{3}a(K_y + \delta k_y)] \\ &= 3 + 4\cos\left(\frac{\pi}{3} + \frac{\sqrt{3}a}{2}\delta k_y\right)\cos\left(\pi + \frac{3a}{2}\delta k_x\right) + 2\cos\left(\frac{2\pi}{3} + \sqrt{3}a\delta k_y\right) \\ &\approx \frac{9a^2}{4}\left(\delta k_x^2 + \delta k_y^2\right) \end{aligned} \tag{2.25}$$

So near the Dirac point, **K**, the dispersion only depends on its distance from that point in the reciprocal space. Taking the square root and redefining $(\delta k_x, \delta k_y) \to (k_x, k_y)$, we get that $|f(\mathbf{k})| = \frac{3a}{2}k$ where $k = |\mathbf{k}| = \sqrt{k_x^2 + k_y^2}$ is redefined as a small displacement in the crystal momentum away from the Dirac point **K**. We get the same result by performing the Taylor expansion around the point **K′**. So for a momentum near either Dirac point the energy dispersion is approximated by

$$\varepsilon(\mathbf{k}) \approx \pm\alpha\frac{3a}{2}|\mathbf{k}| = \pm v_F k. \tag{2.26}$$

Here we defined the Fermi speed of graphene as $v_F = \alpha\frac{3a}{2}$. We note that the energy dispersion should be multiplied by a factor of $\hbar$ since the derivations in this section were done in a system of units where $\hbar = 1$. It is interesting that the approximate energy dispersion of electrons in graphene given in Eq. (2.26) is linear and independent of their mass, similar to the dispersion relation that arises from the study of massless fermions traveling at the speed of light. Using the Dirac equation for spin 1/2 fermions one can arrive at Eq. (2.26) with v_F playing the role of the speed of light, which is found experimentally to take the value $v_F \approx 10^6$ ms^{-2} $\approx \frac{c}{300}$ in graphene [57, 58]. This relation between graphene and the Dirac equation is the reason why points **K** and **K′** in the first Brillouin zone are called Dirac points.

Using Eq. (2.21), we may obtain the eigenstates of the system and examine how the $\mathrm{p_z}$ orbitals on site A and site B are related. Near the Dirac point **K** one may approximate Eq. (2.17) as $f(\mathbf{k}) = \frac{3a}{2}(k_x + ik_y)$, so that the corresponding eigenvectors are solutions of the matrix equation

$$\begin{bmatrix} \pm\alpha k & \alpha(k_x + ik_y) \\ \alpha(k_x - ik_y) & \pm\alpha k \end{bmatrix}\begin{bmatrix} a_\mathbf{k} \\ b_\mathbf{k} \end{bmatrix} = 0. \tag{2.27}$$

This gives the normalized eigenvectors as

$$\mathbf{u}_{\pm} = \frac{1}{\sqrt{2}} \begin{bmatrix} 1 \\ \pm\sqrt{\dfrac{k_x + ik_y}{k_x - ik_y}} \end{bmatrix} \tag{2.28}$$

Using complex analysis we can simplify the above equation into,

$$\mathbf{u}_{\pm} = \frac{1}{\sqrt{2}} \begin{bmatrix} 1 \\ \pm e^{i\theta_k} \end{bmatrix} \tag{2.29}$$

where $\theta_k = \tan^{-1}\left(\dfrac{k_x}{k_y}\right)$ is the polar angle of the vector $\mathbf{k}$. A similar result is found for an eigenvector near the Dirac point $\mathbf{K}'$, but with a difference in phase between the electron orbitals on sites A and B differ. This phase difference between the atoms in the unit cell gives rise to the notions of pseudospin and chirality of electron eigenstates that are key components for relativistic like effects in graphene [59], which will not be discussed in this thesis.

2.3 Density of states

Density of states (DOS) is one of the most salient quantities required in semiconductor physics because it gives the number of states that are accessible for any given energy. For graphene with a two-dimensional dispersion relation function, the DOS is defined as

$$\mathcal{D}(\varepsilon) = g \iint \frac{d^2\mathbf{k}}{(2\pi)^2} \delta(\varepsilon - \varepsilon(\mathbf{k})), \tag{2.30}$$

where the integration is restricted to the first Brillouin zone. The factor g is included in order to account for the degeneracy of the system. In the case of graphene, we have two degenerate spin states and two Dirac points in the first Brillouin zone, so the total degeneracy is $g = 4$. For small energies, $\varepsilon(\mathbf{k})$, near the vicinity of the Dirac points $\mathbf{K}$ or $\mathbf{K}'$ the dispersion is approximately linear in k, Eq. (2.26). Restoring the factor $\hbar$ in the energy dispersion and integrating over the polar angle, we get

$$\mathcal{D}_L(\varepsilon) = 4 \int_0^{\infty} \frac{dk}{2\pi} k \delta(\varepsilon \pm \hbar v_F k), \tag{2.31}$$

which gives the DOS of graphene as

$$\mathcal{D}_L(\varepsilon) = \frac{2|\varepsilon|}{\pi(\hbar v_F)^2}. \tag{2.32}$$

In this approximation, the DOS is also a linear function of energy ε and is symmetric around the origin at $\varepsilon = 0$ corresponding to the Dirac point. This linear model of the DOS is only valid for $|\varepsilon| \lesssim 1$ eV.

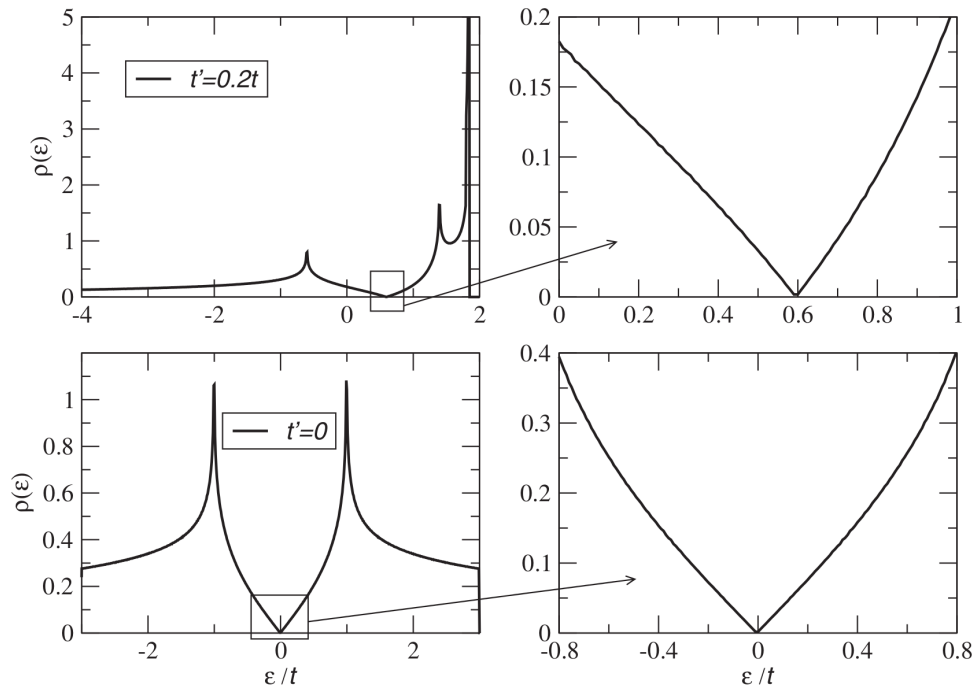

Figure 2.3: The density of states for the graphene lattice. Here $\rho(\varepsilon)$ is the DOS defined in this thesis as $\mathcal{D}(\varepsilon)$ and t and t' are the nearest neightbour and nearest-nearest neighbour coupling parameters respectively. (Top) With 2nd nearest neighbour interactions the Dirac point shifts to the right. The DOS is asymmetric around the Dirac point. (Top right) Although there is still no energy gap, the slopes of the DOS is different for hole and electron doping near the Dirac point. (Bottom) The DOS for graphene considering only nearest neighbour interactions. Van Hove singularities can be seen at approximately $\varepsilon/\alpha = \pm 1$. (Bottom right) The linear DOS near graphene is clearly visible, and has the same slope for both electron and hole doping. Picture adapted from [1]

Beyond the Dirac cone approximation, the DOS becomes nonlinear and exhibits Van Hove singularities at energies $\varepsilon = \pm\alpha$, where α is the hopping energy in the tight binding approximation described in the previous section (see Fig. 2.3). The derivation of the DOS beyond the Dirac cone approximation may be found in [60]. When $|\varepsilon| > 1$ eV, a full expression for $\mathcal{D}(\varepsilon)$ may be written as [1]

$$\mathcal{D}(\varepsilon) = \mathcal{D}_L(\varepsilon)\,\Xi\left(\frac{\varepsilon}{\alpha}\right), \tag{2.33}$$

For electron energies $|\varepsilon| \leq \alpha$, we define $x = \varepsilon/\alpha$ and find

$$\Xi(x) = \frac{\sqrt{3}}{\pi}\frac{1}{\sqrt{\lambda(x)}}K\left(\sqrt{\frac{4x}{\lambda(x)}}\right), \tag{2.34}$$

where

$$\lambda(x) = (1+x)^2 - \frac{1}{4}(x^2-1)^2, \tag{2.35}$$

and $K(y)$ is the elliptic K integral [61]. A series expansion for $\Xi(x)$, given by

$$\Xi(x) = 1 + \frac{1}{3}x^2 + \frac{5}{27}x^4 + \frac{31}{243}x^6 + \frac{71}{729}x^8 + \frac{517}{6561}x^{10} + O(x^{12}), \tag{2.36}$$

is accurate within 1% for $0 < x \leq 0.8$, and it may come handy in estimating the onset of nonlinear effect in the DOS of graphene.

Note that the zero energy reference level in the above expressions for DOS, $\mathcal{D}(\varepsilon)$, is at the Dirac point energy, ε_D, which may be varied by the externally applied electrostatic potential. So, it is convenient to define ε_D with respect to, e.g., local vacuum level and write the electron energy as $\varepsilon = \varepsilon - \varepsilon_D$. If we define the Fermi energy level, ε_F, also with respect to the vacuum level, one may use the DOS to express the equilibrium number density n of *excess* charge carriers per unit area in graphene as

$$n = \int_{-\infty}^{\infty} d\varepsilon\, \mathcal{D}(\varepsilon - \varepsilon_D) \left[\frac{1}{1+\mathrm{e}^{\beta(\varepsilon-\varepsilon_F)}} - \frac{1}{1+\mathrm{e}^{\beta(\varepsilon-\varepsilon_\mathrm{D})}} \right], \tag{2.37}$$

where $\beta = (k_B T)^{-1}$. If one neglects nearest-neighbour coupling in the TBA for graphene π energy bands, then $\mathcal{D}(\varepsilon)$ is an even function of ε. In that case the expression in Eq. (2.37) may be rearranged by defining a chemical potential with respect to intrinsic (or undoped, neutral) graphene as $\mu = \varepsilon_F - \varepsilon_D$, giving

$$n(\mu) = \int_0^{\infty} d\varepsilon\ \mathcal{D}(\varepsilon) \left[\frac{1}{1+e^{\beta(\varepsilon-\mu)}} - \frac{1}{1+e^{\beta(\varepsilon+\mu)}} \right], \tag{2.38}$$

So, when $\mu > 0$ graphene is doped with excess electrons ($n > 0$) so that it is overall negatively charged, while for $\mu < 0$ graphene is doped with excess holes ($n < 0$) and is hence positively charged.

For sufficiently low doping levels, such that, e.g. $|\mu| < 1$ eV, we may use the linear approximation for DOS given in Eq. (2.32), which gives an expression for the equilibrium number density of charge carriers as

$$n(\mu) = \frac{2}{\pi(\hbar v_F \beta)^2} \left\{ \mathrm{dilog}\Big[1 + \exp\left(-\beta\mu\right)\Big] - \mathrm{dilog}\Big[1 + \exp\left(\beta\mu\right)\Big] \right\}, \tag{2.39}$$

where dilog is the standard dilogarithm function [61]. In the limit of zero temperature, $\beta|\mu| \gg 1$, we find from Eq. (2.39) $\mu = \hbar v_F k_F \,\mathrm{sign}(n)$, where the Fermi wavenumber is given by

$$k_F = \sqrt{\pi |n|}. \tag{2.40}$$

In the opposite limit of very high temperature, $\beta|\mu| \ll 1$, we find from from Eq. (2.39)

$$\mu = \frac{\pi}{4} \frac{\beta(\hbar v_F)^2}{\ln 2}\, n. \tag{2.41}$$

Chapter 3

Linear Response of Graphene

One of the technologically most attractive properties of graphene is the tunability of its ground-state charge carrier density $n(\mu)$ by means of external metallic gates. This kind of doping of graphene may be achieved via the mechanism of capacitative charging when a constant potential is applied to a nearby gate electrode with the graphene sheet acting as the opposite plate in a capacitor. Thus, by applying fixed potential(s) to external gate(s) that are placed parallel to a graphene sheet of large area, one may control its chemical potential μ, giving rise to a uniform doping of graphene with constant distribution of its charge carrier density $n(\mu)$.

If graphene is to be used in the configuration of a field effect transistor for nano-electronic, nano-photonic, or biochemical sensing applications, then its charge-transport properties will play a key role. In particular, the electrical conductivity of graphene is strongly affected by the long-range Coulomb scattering of its charge carriers on charged impurities that are often present on the surface of graphene or in a nearby insulating material. Another mechanism that affects the conductivity of graphene at high temperatures involves phonon excitations in graphene or in the nearby polar dielectrics, which will not be studied in this thesis.

Probing the conductivity of graphene in the presence of Coulomb scattering as a function of its equilibrium charge carrier density $n(\mu)$ may be used to determine the electrical potential in the system when the graphene reaches a nominally neutral state, i.e. , when its conductivity reaches a minimum. Ideally, that minimal conductivity should be zero at zero temperature, but in reality it reaches a minimum value due to fluctuations in the charge density over the surface of graphene due to random spatial distribution of charged impurities [39]. Nevertheless, the location of the Dirac point via the conductivity minimum is a robust feature that may be efficiently used for sensing applications of graphene.

Using a semiclassical model for charge transport in graphene, it may be shown that its conductivity may be expressed in terms of an integral involving the spatial fluctuation of the electrostatic potential in graphene due to the presence of charged impurities, where the Coulomb interaction with those impurities is screened by a static polarization of the

charge carriers in the ground state of graphene [1, 39]. Thus, one of the main goals in this thesis is to describe this screening in the presence of other polarizable materials including a liquid solution of salt ions. To that effect, we shall find it beneficial using the electrostatic Green's function for the Poisson equation in the presence of graphene characterized as a polarizable sheet of charge. In particular, we wish to express the spatial fluctuation in the charge density in graphene about its equilibrium charge density in terms of the fluctuation of the total electrostatic potential in the plane of graphene.

3.1 Thomas-Fermi (TF) model

A simple description for static screening of external charges by the polarization of charge carriers (electrons or holes) in a large-area graphene sheet may be formulated within a two-dimensional Thomas-Fermi (TF) model, where we neglect the thickness of graphene. We use a Cartesian coordinate system with coordinates $\mathbf{R} = (\mathbf{r}, z)$, where $\mathbf{r} = (x, y)$, and assume that graphene is placed in the plane $z = 0$ with $\Phi(\mathbf{R}) = \Phi(\mathbf{r}, z)$ being electrostatic potential in the system. We define $\phi_0(\mathbf{r}) = \Phi(\mathbf{r}, z)|_{z=0}$ as a fluctuation of the potential in the plane of graphene about its average value, which is incorporated in the chemical potential μ that defines the ground state of graphene. The non-linear TF model for the potential $\phi_0(\mathbf{r})$ in the plane of graphene is given by the equation [62]

$$\phi_0(\mathbf{r}) = \phi_{ext}(\mathbf{r}) - e \iint d^2\mathbf{r}' \; n_{ind}(\mathbf{r}') \; G(\mathbf{r}, \mathbf{r}') + V_{xc}, \tag{3.1}$$

where

$$n_{ind}(\mathbf{r}) = n\left(\mu + e\phi_0\left(\mathbf{r}\right)\right) - n(\mu) \tag{3.2}$$

is a fluctuation of the number density of charge carriers per unit area in graphene about the ground state value $n(\mu)$, which is induced by some external electrostatic potential, having the value $\phi_{ext}(\mathbf{r})$ at a point $\mathbf{r}$ in the plane of graphene. Note that $e > 0$ is the charge of a proton, so that wherever $\phi_{ext}(\mathbf{r}) > 0$ in Eq. (3.2) the chemical potential is increased by the value $e\phi_{ext}(\mathbf{r})$ giving rise to a local excess of electrons in graphene, and vice versa. In Eq. (3.1), $G(\mathbf{r}, \mathbf{r}')$ is the electrostatic Green's function describing Coulomb interactions in the plane of graphene, whereas the exchange and correlation interaction may be approximately treated within the TF model by adding a term V_{xc} based on a local density approximation [63].

When $|n|$ is large enough so that $|e\phi_0| \ll |\mu|$, one may approximate the induced density of charge carriers as a linear expansion about the ground state chemical potential μ as

$$n_{ind}(\mathbf{r}) \approx \chi_{TF} \, e\phi_0(\mathbf{r}) \tag{3.3}$$

where we have defined the TF polarizability of graphene as

$$\chi_{TF} \equiv \frac{\partial n}{\partial \mu} = \frac{4}{\pi} \frac{1}{\beta(\hbar v_F)^2} \ln\left[2 \, \cosh\left(\frac{\beta\mu}{2}\right)\right]. \tag{3.4}$$

Notice that this quantity is also related to the inverse TF screening length in graphene,

$$q_{TF} = 2\pi e^2 \chi_{TF}, \tag{3.5}$$

as well as to the so-called quantum capacitance per unit area of graphene,

$$C_q = e^2 \chi_{TF}. \tag{3.6}$$

Since the TF polarizability of graphene is independent of the position $\mathbf{r}$, giving rise to a local relation between $n_{ind}(\mathbf{r})$ and $\phi_0(\mathbf{r})$ in Eq. (3.3), we may invoke the translational invariance of the Coulomb interactions in graphene, whereby $G(\mathbf{r}, \mathbf{r}') = G(\mathbf{r} - \mathbf{r}')$, and solve Eq. (3.1) by means of the 2D Fourier Transform of the potential in the plane of graphene, defined as

$$\tilde{\phi}_0(\mathbf{q}) = \iint d^2\mathbf{r}\ e^{-i\mathbf{q}\cdot\mathbf{r}} \phi_0(\mathbf{r}), \tag{3.7}$$

where $\mathbf{q} = (q_x, q_y)$. Assuming that graphene is free, so that $G(\mathbf{r}, \mathbf{r}') = 1/|\mathbf{r} - \mathbf{r}'|$, and neglecting the exchange-correlation interaction, we obtain from Eq. (3.1)

$$\tilde{\phi}_0(\mathbf{q}) = \frac{\tilde{\phi}_{ext}(\mathbf{q})}{\epsilon_{TF}(q)}, \tag{3.8}$$

where we have defined the TF static dielectric function of graphene as

$$\epsilon_{TF}(q) = 1 + \frac{q_{TF}}{q}, \tag{3.9}$$

with $q = \sqrt{q_x^2 + q_y^2}$.

While the TF model of 2D screening by graphene is expected to work reasonably well for small q values (and hence large distances r from a point-like charge in graphene), a more accurate description of the polarizability of graphene is needed for larger q values, i.e. when $q > k_F$, where k_F is the Fermi wavenumber of doped graphene. In the next section we described a detailed derivation of the polarizability function of graphene in the Random Phase Approximation [59].

3.2 Random Phase Approximation (RPA)

The Random Phase Approximation (RPA) is a prevalent general frame of reference for examining many-electron systems and their response to external electric fields, which has been successfully used in the field of condensed matter physics to investigate the dielectric function of a free-electron gas [64]. The key concept leading to RPA is to explore particle-hole excitations caused by an external field. Weakness of the electron-electron interaction

in the material is a necessary condition for the RPA to be plausible. However, the quasiparticle interaction is not necessarily weak in graphene. The coupling constant responsible for the strength of Coulomb interactions in graphene is given by $\frac{r_s}{\epsilon} \approx \frac{2.19}{\epsilon}$, where ϵ is relative dielectric constant of the material around graphene. The coupling constant of graphene $r_s = \frac{e^2}{\hbar v_F} \approx 2.19$ emerges in the perturbative expansion of its polarization function employing the RPA. This constant is analogous to the fine-structure constant in Quantum Field theory. The coupling constant is greater than 1 in free graphene ($\epsilon = 1$), resulting in the perturbative expansion of the interactions dubious, but since the coupling constant is controlled by the dielectric environment surrounding graphene, its value could be reduced to much less than 1 utilizing a suitable substrate. The debate surrounding the RPA's validity in graphene is still not over [65, 66]. On the other hand, the literature seems to agree that the problems arise in the case of intrinsic graphene (i.e. undoped graphene with the density of charge carriers close to zero). However, in the case of extrinsic graphene, where the Fermi energy is located far away from the Dirac point, the logarithmic ultraviolet and infrared divergences arising from the momentum integral not including an upper and a lower cutoff respectively cancel each other out [65], making the RPA well behaved.

We will follow the method of Bohm and Pines to derive the RPA polarization function of graphene [67]. The very first step for this derivation is to use the most basic properties of the density matrix. The density matrix portrays a quantum system in an ensemble of several quantum states. It is the quantum mechanical analogous to the classical phase space distribution, which assesses the dynamics of the system. The equation governing the quantum dynamics of the many-electron system is known as the Liouville equation and it is given by

$$i\hbar\frac{\partial\rho}{\partial t} = [\mathbf{H}, \rho]. \tag{3.10}$$

Here, $\mathbf{H}$ is a Hamiltonian operator and ρ is the density matrix, which is also an operator acting on a Hilbert space. Additionally, [*,*] is the usual commutation operator. In most of the cases, we cannot solve Eq. (3.10). On the other hand, we may approximate it through the use of a simpler, solvable Hamiltonian. We would like to expand the Hamiltonian operator into its unperturbed Hamiltonian part and a perturbation potential as a result of both external and induced internal effects reacting to the external field,

$$\mathbf{H} = \mathbf{H}_0 + V \tag{3.11}$$

We treat the perturbation potential, V, to be small when compared to the unperturbed Hamiltonian, $\mathbf{H}_0$. Let us assume the states, $|\psi_k\rangle$, be the eigenstates of the unperturbed Hamiltonian with corresponding energy levels ε_{k} (i.e. $\mathbf{H}_0|\psi_k\rangle = \varepsilon_k|\psi_k\rangle$). As we are taking into account a many-body system, we notice that the index k in general incorporates a vector depicting the momentum, as well as the band indices, of the many-body system. We expand the density matrix as a sum of an unperturbed and a perturbation density matrix,

$$\rho = \rho_0 + \rho_1 \tag{3.12}$$

We assume that ρ_0 governs the dynamics of the unperturbed Hamiltonian and is a solution to an equation analogous to Eq. (3.10), $i\hbar\dfrac{\partial\rho_0}{\partial t} = [\mathbf{H}_0, \rho_0]$. Likewise, when ρ_0 acts on one of the unperturbed states, $|\psi_k\rangle$, it gives the probability of the system being in state $|\psi_k\rangle$, that is $\rho_0|\psi_k\rangle = f(\varepsilon_k)|\psi_k\rangle$, where $f(\varepsilon_k)$ is the Fermi-Dirac distribution function. Now, we want to approximate the solution to Eq. (3.10) for the full perturbed system

$$i\hbar\left(\frac{\partial\rho_0}{\partial t} + \frac{\partial\rho_1}{\partial t}\right) = [\mathbf{H}_0 + V, \rho_0 + \rho_1]. \tag{3.13}$$

giving

$$i\hbar\frac{\partial\rho_1}{\partial t} = [\mathbf{H}_0, \rho_1] + [V, \rho_0] + [V, \rho_1]. \tag{3.14}$$

V and ρ_1 are small perturbations to the first order. Consequently, we will ignore the last term in the equation above due to a second order effect. Evaluating the matrix elements of the equation above in the basis of the unperturbed Hamiltonian yields

$$\begin{aligned} i\hbar\frac{\partial}{\partial t}\langle\psi_k|\rho_1|\psi_{k'}\rangle &= \langle\psi_k|[\mathbf{H}_0, \rho_1]|\psi_{k'}\rangle + \langle\psi_k|[V, \rho_0]|\psi_{k'}\rangle \\ &= (\varepsilon_k - \varepsilon_{k'})\langle\psi_k|\rho_1|\psi_{k'}\rangle + (f(\varepsilon_{k'}) - f(\varepsilon_k))\langle\psi_k|\rho_1|\psi_{k'}\rangle, \end{aligned} \tag{3.15}$$

where the last equality follows from the properties of the eigenstate $|\psi_k\rangle$ interacting with operators $\mathbf{H}_0$ and ρ_0, which were described earlier. Taking the Fourier transform in the time domain, we obtain

$$(\omega\hbar + i\nu^+)\langle\psi_k|\rho_1|\psi_{k'}\rangle = (\varepsilon_k - \varepsilon_{k'})\langle\psi_k|\rho_1|\psi_{k'}\rangle + (f(\varepsilon_{k'}) - f(\varepsilon_k))\langle\psi_k|V|\psi_{k'}\rangle. \tag{3.16}$$

Here ν^+ is a small positive number that is taken to approach zero. It arises from causality, that is initially (in the limit $t \to -\infty$), the system is assumed to be unperturbed and the perturbing potential is applied adiabatically. Collecting the like terms results in

$$\langle\psi_k|\rho_1|\psi_{k'}\rangle = \frac{f(\varepsilon_{k'}) - f(\varepsilon_k)}{\varepsilon_k - \varepsilon_{k'} + \omega\hbar + i\nu^+}\langle\psi_k|V|\psi_{k'}\rangle. \tag{3.17}$$

The above result is valid under the condition that $|\psi_k\rangle$ are eigenstates of the unperturbed Hamiltonian. Eq. (3.17) gives us the first order correction to the density matrix. Higher order corrections can be obtained using Eq. (3.17), but we will not consider these in this thesis.

Now we can utilize the first order correction of the density matrix to examine the induced charge density at any point in space. Firstly, we need to make some assertions about the system we wish to study and its eigenstate wavefunctions $|\psi_k\rangle$. Since this thesis mainly deals with graphene, we assume that our system is a two dimensional crystal with periodic structure that could be described by some primitive basis vectors as described in Chapter 2. First, we describe the wavefunctions $|\psi_k\rangle$ that we will be using. Utilizing

the tight binding model, we have already calculated the electron wavefunction of graphene near the Dirac points $\mathbf{K}$ and $\mathbf{K}'$ (Eq. (2.28)) and we know the dispersion of the energy for different momenta (Eq. (2.26)). Since there are two energy bands, we can label the electron wavefunctions as $|\mathbf{k}, l\rangle$. Here $\mathbf{k}$ indicates the two dimensional (2D) momentum of our wavefunctions and l is the index delineating one of the two bands of the $\pi-$bonds. Then we could specify the wavefunctions in position space as

$$\langle \mathbf{r}, z|\mathbf{k}, l\rangle = \psi_{\mathbf{k},l}(\mathbf{r}, z) = \frac{1}{\sqrt{A}} e^{i\mathbf{k}\cdot\mathbf{r}} u_{\mathbf{k},l}(\mathbf{r}, z), \tag{3.18}$$

where A is the area of the crystal solid that we wish to investigate. Since graphene is a two dimensional material, we are only concerned with momentum waves traveling in the plane of graphene. This implies that $\mathbf{r}$ and $\mathbf{k}$ are two dimensional vectors. Graphene is examined in a three dimensional space, so we must incorporate the out of plane dependence (the z dependence) on the wavefunction. $e^{i\mathbf{k}\cdot\mathbf{r}}$ is a plane wave with momentum $\mathbf{k}$, which is the momentum of the crystal lattice, and $u_{\mathbf{k},l}(\mathbf{r}, z)$ is a function which is periodic in the $\mathbf{r}$ coordinates and has the same period as the crystal in position space (i.e. $u_{\mathbf{k},l}(\mathbf{r}+\mathbf{R}, z) = u_{\mathbf{k},l}(\mathbf{r}, z)$) where $\mathbf{R}$ is some two dimensional lattice translational vector of graphene). Additionally, we follow usual convention and define $l = 1$ for the conduction band and $l = -1$ for the valence band.

An external charge will induce an opposing charge density on the surface of graphene. Now the induced number density of carriers per unit volume in graphene may be described as the expectation value of the density matrix of a charged particle in position space,

$$N_{ind}(\mathbf{r}, z) = \langle \mathbf{r}, z|\rho_1|\mathbf{r}, z\rangle. \tag{3.19}$$

The dependence of induced charge density on the frequency ω is implied, however we drop it for brevity. We may expand Eq. (3.19) in momentum space by utilizing the completeness relation $1 = \sum_{\mathbf{k},l} |\mathbf{k}, l\rangle\langle\mathbf{k}, l|$,

$$\begin{aligned} N_{ind}(\mathbf{r}, z) &= \sum_{\mathbf{k}',l'}\sum_{\mathbf{k},l} \langle \mathbf{r}, z|\mathbf{k}', l'\rangle\langle\mathbf{k}', l'|\rho_1|\mathbf{k}, l\rangle\langle\mathbf{k}, l|\mathbf{r}, z\rangle \\ &= \sum_{\mathbf{k}',l'}\sum_{\mathbf{k},l} \psi^*_{\mathbf{k}',l'}(\mathbf{r}, z)\langle\mathbf{k}', l'|\rho_1|\mathbf{k}, l\rangle\psi_{\mathbf{k},l}(\mathbf{r}, z) \end{aligned} \tag{3.20}$$

To evaluate the above equation, we will take into account a 2D FT of the induced charge density,

$$\begin{aligned} \tilde{N}_{ind}(\mathbf{q}, z) &= \iint d^2\mathbf{r} e^{-i\mathbf{q}\cdot\mathbf{r}} N_{ind}(\mathbf{r}, z) \\ &= \sum_{\mathbf{k}',l'}\sum_{\mathbf{k},l} \langle\mathbf{k}', l'|\rho_1|\mathbf{k}, l\rangle \iint d^2\mathbf{r}\psi^*_{\mathbf{k}',l'}(\mathbf{r}, z)e^{-i\mathbf{q}\cdot\mathbf{r}}\psi_{\mathbf{k},l}(\mathbf{r}, z). \end{aligned} \tag{3.21}$$

As the matrix elements $\langle \mathbf{k}', l'|\rho_1|\mathbf{k}, l\rangle$ are independent of the position $\mathbf{r}$, these are taken out of the integral. We may reduce our integral using the properties of the Bloch wave functions to yield

$$\begin{aligned}
&= \sum_{\mathbf{k}',l'}\sum_{\mathbf{k},l}\langle \mathbf{k}', l'|\rho_1|\mathbf{k}, l\rangle\delta_{\mathbf{k},\mathbf{k}'+\mathbf{q}}\iint d^2\mathbf{r}\psi^*_{\mathbf{k}',l'}(\mathbf{r},z)e^{-i\mathbf{q}\cdot\mathbf{r}}\psi_{\mathbf{k}'+\mathbf{q},l}(\mathbf{r},z)\\
&= \sum_{\mathbf{k}',l'}\sum_{\mathbf{k},l}\langle \mathbf{k}', l'|\rho_1|\mathbf{k}'+\mathbf{q}, l\rangle\langle \mathbf{k}', l'|e^{-i\mathbf{q}\cdot\mathbf{r}}|\mathbf{k}'+\mathbf{q}, l\rangle\\
&= \sum_{\mathbf{k}',l'}\sum_{\mathbf{k},l}\langle \mathbf{k}', l'|\rho_1|\mathbf{k}'+\mathbf{q}, l\rangle M^{l,l'}_{\mathbf{k}',\mathbf{k}'+\mathbf{q}}(z). \qquad (3.22)
\end{aligned}$$

Here, we have defined $M^{l,l'}_{\mathbf{k}',\mathbf{k}'+\mathbf{q}}(z)$ as the 2D FT of $\psi^*_{\mathbf{k}',l'}(\mathbf{r},z)\psi_{\mathbf{k}'+\mathbf{q},l}(\mathbf{r},z)$. Utilizing Eq. (3.17) for the matrix elements of the density matrix ρ_1, we expand our equation above to obtain

$$\tilde{N}_{ind}(\mathbf{q},z) = 2\sum_{\mathbf{k}',l'}\sum_{\mathbf{k},l}\frac{f(\varepsilon_{\mathbf{k}',l'})-f(\varepsilon_{\mathbf{k}'+\mathbf{q},l})}{\varepsilon_{\mathbf{k}',l'}-\varepsilon_{\mathbf{k}'+\mathbf{q},l}+\omega\hbar+i\nu^+}\langle \mathbf{k}', l'|V|\mathbf{k}'+\mathbf{q}, l\rangle M^{l,l'}_{\mathbf{k}',\mathbf{k}'+\mathbf{q}}(z) \qquad (3.23)$$

The multiple of 2 may be attributed to account for the spin degeneracy of the electrons. In the more general situations where the spin of electrons is coupled to the external interactions, the factor of 2 cannot be added and the spin interactions must be accounted for in the energy dispersion $\varepsilon_{\mathbf{k},l}$. To simplify Eq. (3.23) even further, we require to calculate the matrix elements of the potential operator V. Implementing this, we once again invoke the FT of the potential function in position space

$$V(\mathbf{r}',z') = \iint\frac{d^2\mathbf{q}'}{(2\pi)^2}e^{i\mathbf{q}'\cdot\mathbf{r}'}\tilde{V}(\mathbf{q}',z') \qquad (3.24)$$

Utilizing this definition of the potential function, the matrix elements in Eq. (3.23) yield

$$\begin{aligned}
\langle \mathbf{k}', l'|V|\mathbf{k}'+\mathbf{q}, l\rangle = &\iint d^2\mathbf{r}'\int dz'\psi^*_{\mathbf{k}',l'}(\mathbf{r}',z')V(\mathbf{r}',z')\psi_{\mathbf{k}'+\mathbf{q},l}(\mathbf{r}',z')\\
&\iint\frac{d^2\mathbf{q}'}{(2\pi)^2}\int dz'\tilde{V}(\mathbf{q}',z')\iint d^2\mathbf{r}'\psi^*_{\mathbf{k}',l'}(\mathbf{r}',z')e^{-i\mathbf{q}'\cdot\mathbf{r}'}\psi_{\mathbf{k}'+\mathbf{q},l}(\mathbf{r}',z') \qquad (3.25)
\end{aligned}$$

Next, to integrate out the $\mathbf{r}'$ variable we utilize a similar trick as done before. This simplifies the above equation to

$$\begin{aligned}
\langle \mathbf{k}', l'|V|\mathbf{k}'+\mathbf{q}, l\rangle &= \iint\frac{d^2\mathbf{q}'}{(2\pi)^2}dz'\tilde{V}(\mathbf{q}',z')\delta(\mathbf{q}-\mathbf{q}')\iint d^2\mathbf{r}'\psi^*_{\mathbf{k}',l'}(\mathbf{r}',z')e^{-i\mathbf{q}'\cdot\mathbf{r}'}\psi_{\mathbf{k}'+\mathbf{q},l}(\mathbf{r}',z')\\
&= \int dz'\tilde{V}(\mathbf{q},z')M^{l,l'}_{\mathbf{k}',\mathbf{k}'+\mathbf{q}}(z'). \qquad (3.26)
\end{aligned}$$

Therefore, finally the FT of the induced charge density has the form

$$\tilde{N}_{ind}(\mathbf{q},z) = 2\sum_{\mathbf{k}}\sum_{l,l'}\frac{f(\varepsilon_{\mathbf{k},l'})-f(\varepsilon_{\mathbf{k}+\mathbf{q},l})}{\varepsilon_{\mathbf{k},l'}-\varepsilon_{\mathbf{k}+\mathbf{q},l}+\omega\hbar+i\nu^+}M^{l,l'}_{\mathbf{k},\mathbf{k}+q}(z)\int dz' M^{l,l'}_{\mathbf{k},\mathbf{k}+q}(z')\tilde{V}(\mathbf{q},z'). \qquad (3.27)$$

Hence, we obtain the most general form of the induced charge density for graphene, taking into account the only assumption about graphene that it is a two dimensional periodic lattice.

Using the first order approximation to the density matrix defined in Eq. (3.17) results in Eq. (3.27). The function $M^{l,l'}_{\mathbf{k},\mathbf{k}'}(z)$ may be thought of as the average z dependence of the wavefunction. A practical approach to evaluating it is through the use of the electron orbital structure of graphene which was derived using the tight binding approximation. The π-bonds formed from $2p_z$ orbital wavefunctions have an electron density that decays exponentially in the z direction. The spatial decay rate is less than an angstrom, hence a distance of a few angstroms away from the graphene surface leads to a negligible electron density contribution from the bonds. The function $M^{l,l'}_{\mathbf{k},\mathbf{k}'}(z)$ is assumed to be localized in the plane of graphene as a consequence of the zero thickness approximation of graphene. It is a somewhat an abstract approximation, as impurities near the surface of graphene could significantly overlap with the electron orbitals. We ignore the effects of orbital overlap since they make the corresponding calculations less attractive and inseparable. Instead we approximate $\sqrt{A}M^{l,l'}_{\mathbf{k},\mathbf{k}'}(z) \approx \bar{M}^{l,l'}_{\mathbf{k},\mathbf{k}'}\,\delta(z)$. Hence, the last factor in Eq. (3.27) becomes

$$M^{l,l'}_{\mathbf{k},\mathbf{k}'}(z)\int dz' M^{l,l'}_{\mathbf{k},\mathbf{k}+q}(z')\tilde{V}(\mathbf{q},z') = \frac{1}{A}\delta(z)\tilde{V}(\mathbf{q},z)|\bar{M}^{l,l'}_{\mathbf{k},\mathbf{k}'}|^2, \tag{3.28}$$

giving us an induced charge density of

$$\tilde{N}_{ind}(\mathbf{q},z) = 2\delta(z)\tilde{V}(\mathbf{q},z)\iint \frac{d^2\mathbf{k}}{(2\pi)^2}\sum_{l,l'}\frac{f(\varepsilon_{\mathbf{k},l'}) - f(\varepsilon_{\mathbf{k}+\mathbf{q},l})}{\varepsilon_{\mathbf{k},l'} - \varepsilon_{\mathbf{k}+\mathbf{q},l} + \omega\hbar + i\nu^+}|\bar{M}^{l,l'}_{\mathbf{k},\mathbf{k}'}|^2, \tag{3.29}$$

where we have turned the sum over $\mathbf{k}$ into an integral over the 1st Brillouin zone. This is an authentic step since the spacing between consecutive momenta becomes smaller and smaller as the size of the graphene sheet becomes larger. For a theoretically infinite graphene sheet, the sum transforms into an integral. In the zero thickness approximation of graphene, the induced charge density resides on the plane of graphene.

Although the idea of a zero thickness graphene sheet may seem somewhat ad hoc the formalism greatly simplifies our calculations and is accurate enough for our application. Note that the Delta function in Eq. (3.29) implies that we may set $z = 0$ in the perturbed energy of electrons in graphene $\tilde{V}(\mathbf{q},z)$, which may be then expressed in terms of the in-plane value of the electrostatic potential as

$$\tilde{V}(\mathbf{q},0) = -e\tilde{\phi}_0(\mathbf{q}). \tag{3.30}$$

If we further express the volume density of the induced charge carriers in graphene in terms of a 2D FT of the surface density of charge carriers as

$$\tilde{N}_{ind}(\mathbf{q},z) \approx \delta(z)\,\tilde{n}_{ind}(\mathbf{q}), \tag{3.31}$$

we may utilize Eq. (3.29) to rewrite the linear response relation of Eq. (3.3) in the Fourier space as

$$\tilde{n}_{ind}(\mathbf{q}) = \chi(\mathbf{q})\,e\tilde{\phi}_0(\mathbf{q}) \tag{3.32}$$

where we define the in-plane polarizability of graphene in the RPA as

$$\chi(\mathbf{q}) = -2 \iint \frac{d^2\mathbf{k}}{(2\pi)^2} \sum_{l,l'} |\bar{M}^{l,l'}_{\mathbf{k},\mathbf{k}'}|^2 \frac{f(\varepsilon_{\mathbf{k},l'}) - f(\varepsilon_{\mathbf{k}+\mathbf{q},l})}{\varepsilon_{\mathbf{k},l'} - \varepsilon_{\mathbf{k}+\mathbf{q},l} + \omega\hbar + i\nu^+}. \tag{3.33}$$

Next step we need to undertake is to evaluate the matrix elements of $|\bar{M}^{l,l'}_{\mathbf{k},\mathbf{k}'}|^2$ which is the FT of two wavefunctions. Expanding the wavefunctions by using the tight binding approximation from Eq. (2.10)

$$\bar{M}^{l,l'}_{\mathbf{k},\mathbf{k}+\mathbf{q}} = \iint d^2\mathbf{r} \int dz [a^*_{\mathbf{k},l}\psi^*_{A,\mathbf{k}} + b^*_{\mathbf{k},l}\psi^*_{B,\mathbf{k}}] e^{-i\mathbf{q}\cdot\mathbf{r}} [a_{\mathbf{k}+\mathbf{q},l'}\psi_{A,\mathbf{k}+\mathbf{q}} + b_{\mathbf{k}+\mathbf{q},l}\psi_{B,\mathbf{k}+\mathbf{q}}] \tag{3.34}$$

The evaluation of this integral is cumbersome and the reader is encouraged to go through its derivation in the Appendix 8.1. Here, we shall restate the result

$$\bar{M}^{l,l'}_{\mathbf{k},\mathbf{k}+\mathbf{q}} = \frac{1}{2}\mathcal{R}(\mathbf{q}) \left[1 + (-1)^{l+l'} \frac{f(\mathbf{k}) f(\mathbf{k}+\mathbf{q})}{|f(\mathbf{k})||f(\mathbf{k}+\mathbf{q})|} \right] \tag{3.35}$$

where $\mathcal{R}(\mathbf{q})$ is the two-dimensional Fourier transform of the modulus squared of the unperturbed p_z orbital,

$$\mathcal{R}(\mathbf{q}) = \int dz \iint d^2\mathbf{r} |\Upsilon_{p_z}(\mathbf{r}, z)|^2 e^{i\mathbf{q}\cdot\mathbf{r}} = \left[1 + \left(\frac{a_0 q}{Z_{eff}} \right)^2 \right]^{-3} \tag{3.36}$$

Here a_0 is the Bohr radius and Z_{eff} is the effective charge of the screened nucleus in the carbon atom [68]. Taking the modulus squared of $\bar{M}^{l,l'}_{\mathbf{k},\mathbf{k}+\mathbf{q}}$ leads to

$$|\bar{M}^{l,l'}_{\mathbf{k},\mathbf{k}+\mathbf{q}}|^2 = \frac{1}{2}\mathcal{R}^2(q) \left[1 + (-1)^{l+l'} \Re\left(\frac{f(\mathbf{k}) f(\mathbf{k}+\mathbf{q})}{|f(\mathbf{k})||f(\mathbf{k}+\mathbf{q})|} \right) \right]. \tag{3.37}$$

We resort to the most commonly used assumption, $\mathcal{R}^2(q) \approx 1$ for the range of q values of interest here [69, 70], so that the polarization function becomes

$$\chi(\mathbf{q}) = -\iint_{BZ} \frac{d^2\mathbf{k}}{(2\pi)^2} \sum_{l,l'} \left[1 + (-1)^{l+l'} \Re\left(\frac{f(\mathbf{k}) f(\mathbf{k}+\mathbf{q})}{|f(\mathbf{k})||f(\mathbf{k}+\mathbf{q})|} \right) \right] \frac{f(\varepsilon_{\mathbf{k},l'}) - f(\varepsilon_{\mathbf{k}+\mathbf{q},l})}{\varepsilon_{\mathbf{k},l'} - \varepsilon_{\mathbf{k}+\mathbf{q},l} + \omega\hbar + i\nu^+} \tag{3.38}$$

The above integral cannot be evaluated analytically for the general energy dispersion, yet in the Dirac cone approximation, $\varepsilon_{\mathbf{k},l} = (-1)^l \hbar v_F |\mathbf{k}|$, analytical results may be achieved for finite ω and zero temperature [69, 70], as well as for the static case at finite temperature [71]. Since we are especially interested in this thesis in static screening of graphene in the presence of liquid electrolyte at finite temperature, we showcase in Appendix 8.2 some key steps in the derivation of the polarization function by setting $\omega = 0$ and $\nu^+ \to 0^+$ in Eq. (3.38).

3.3 Semiclassical transport in graphene

Electrical conductivity of doped graphene is dominated by the long-ranged elastic Coulomb scattering of its charge carriers on the nearby charged impurities and, at high enough temperatures, also by the charge carriers'interaction with phonons, both in graphene and in the nearby substrate. Although we are not going to compute electrical conductivity of graphene in this thesis, it is instructive to show how the presence of charged impurities enters in the expression for graphene conductivity, Σ, obtained using the semiclassical Boltzmann transport theory at finite temperature as [71]

$$\Sigma = \frac{e^2 v_F^2}{2} \int d\varepsilon \; D(\varepsilon) \; \tau(\varepsilon) \left(-\frac{\partial f}{\partial \varepsilon} \right). \tag{3.39}$$

Here, $D(\varepsilon)$ is the density of states in graphene and $\tau(\varepsilon)$ is the relaxation time, or the transport scattering time, which is obtained for uncorrelated point-charge impurities with the average number per unit area, $\bar{n}_{imp}$, as

$$\frac{1}{\tau(\varepsilon_{s\mathbf{k}})} = \frac{2\pi \bar{n}_{imp}}{\hbar} \iint \frac{d^2\mathbf{k}'}{(2\pi)^2} |V_{s\mathbf{k},s\mathbf{k}'}|^2 [1 - \cos\theta_{\mathbf{k}\mathbf{k}'}] \delta(\varepsilon_{s\mathbf{k}} - \varepsilon_{s\mathbf{k}'}), \tag{3.40}$$

where $\theta_{\mathbf{k}\mathbf{k}'}$ is the angle between the electron momenta $\mathbf{k}$ and $\mathbf{k}'$. In Eq. (3.40), the squared modulus of the matrix element for the Coulomb scattering potential is given by

$$|V_{s\mathbf{k},s\mathbf{k}'}|^2 = |\widetilde{\varphi}(\mathbf{q})|^2 \, \frac{1 + \cos\theta_{\mathbf{k}\mathbf{k}'}}{2} \tag{3.41}$$

where $\widetilde{\varphi}(\mathbf{q})$ is the 2D Fourier transform of the screened Coulomb potential of individual impurity with $\mathbf{q} = \mathbf{k}' - \mathbf{k}$.

It is important to realize that disorder plays a crucial role in the transport properties of graphene [39, 72]. In particular, the randomness in the spatial arrangement of charged impurities in the substrate gives rise to a fluctuation in the electrostatic potential in the plane of graphene, $\delta\phi_0(\mathbf{r})$, which in turn disrupts coherent motion of charged impurities in graphene and hence gives rise to its electrical resistivity [39, 73, 74]. Thus, denoting the ensemble average over the impurity positions by $\langle \cdots \rangle$, one can show that, for heavily doped graphene with the equilibrium charge carrier density $\bar{n}$ at *zero temperature*, the average resistivity of graphene, $\varrho = \langle \Sigma^{-1} \rangle$, is given by [74]

$$\varrho = \frac{2}{e^2 v_F^2 D(\varepsilon_F)} \left\langle \frac{1}{\tau(\varepsilon_F)} \right\rangle, \tag{3.42}$$

where $\varepsilon_F = \hbar v_F k_F$ is the Fermi energy of graphene with $k_F = \sqrt{\pi |\bar{n}|}$, and

$$\left\langle \frac{1}{\tau(\varepsilon_F)} \right\rangle = \frac{\bar{n}_{imp}}{2\pi} \frac{v_F}{\varepsilon_F^2} \int_0^{2k_F} dq \, q^2 \sqrt{1 - \left(\frac{q}{2k_F} \right)^2} \; |\widetilde{\varphi}(\mathbf{q})|^2 \; I(q). \tag{3.43}$$

Here, $I(q)$ is the geometric structure factor describing spatial correlation between charged impurities that occupy random positions in a plane parallel to graphene, usually assumed to lie inside or on the surface of an insulating oxide layer [39, 73]. It may also be shown that, if the distribution of the impurity positions is translationally invariant in directions parallel to graphene, then the auto-covariance function of the electrostatic potential fluctuations in the plane of graphene, $\langle \delta\phi_0(\mathbf{r})\, \delta\phi_0(\mathbf{r}')\rangle \equiv C(\mathbf{r}-\mathbf{r}')$, may be expressed as [74, 75]

$$C(\mathbf{r}-\mathbf{r}') = \bar{n}_{imp} \iint \frac{d^2\mathbf{q}}{(2\pi)^2}\, e^{i\mathbf{q}\cdot(\mathbf{r}-\mathbf{r}')}\, |\widetilde{\varphi}(\mathbf{q})|^2\; I(q). \tag{3.44}$$

It is interesting that this function has been observed experimentally by a combination of the scanning tunneling microscopy and atomic force microscopy [75]. Equations Eqs. (3.43) and (3.44) show that the auto-covariance function $C(\mathbf{r}-\mathbf{r}')$ plays a determining role in the transport properties of doped graphene. Hence, we shall pay particular attention to the screening of $C(\mathbf{r}-\mathbf{r}')$ by the polarization of charge carriers in graphene and mobile ions in the electrolyte.

Particularly intriguing, and still quite elusive are the mechanisms of transport in undoped, or nominally neutral graphene. In the absence of randomness, Eqs. (3.42) and (3.43) show that the resistivity of graphene should $\to \infty$ (or the conductivity should vanish) as $\bar{n} \to 0$ at zero temperature, which is in clear disagreement with experiments showing that graphene attains finite conductivity when $\bar{n} \to 0$ [39, 72]. One possible explanation is based on the fact that fluctuations of the electrostatic potential in neutral graphene give rise to a system of electron-hole puddles, which facilitate electrical conduction. In that context, the authors of Ref. [72] proposed a phenomenological but self-consistent model for conductivity in a weakly doped graphene, which is based on the variance of the fluctuating part of the in-plane potential, $C(0) \equiv \langle[\delta\phi_0(\mathbf{r})]^2\rangle$. Namely, keeping in mind that the screened potential in graphene depends on the average doping density of graphene, $\delta\phi_0(\mathbf{r}) = \delta\phi_0(\mathbf{r};\bar{n})$, the authors postulated that there exists some residual charge carrier density, $\bar{n} = n^*$, such that the square of the corresponding effective Fermi energy, $(\varepsilon_F^*)^2 = \pi n^* (\hbar v_F)^2$, equals the variance of that potential, giving an equation to be solved for n^* [39, 72]

$$(\hbar v_{\mathrm{F}})^2\, \pi n^* = e^2 \langle[\delta\phi_0(\mathbf{r};n^*)]^2\rangle. \tag{3.45}$$

Then, considering the conductivity of graphene as a function of the average charge carrier density, $\Sigma(\bar{n})$, one may estimate the minimum conductivity in a nominally neutral graphene due to the electron-hole puddles as $\Sigma(n^*)$. Given the current research focus on that quantity, we shall also analyze the screening effects of mobile ions in the dependence of variance $C(0) \equiv \langle[\delta\phi_0(\mathbf{r})]^2\rangle$ on the average doping density of graphene.

Chapter 4

Screening in Electrolyte

When charged surface of a solid is immersed in an aqueous solution with added salt at the concentration c_0, the dissolved salt ions with the charge opposite to that of the solid surface (counter-ions) will be attracted to the surface, while the ions having the same charge as the surface (co-ions) will be repelled from it. As a result, an electric double layer will be formed close to that surface, which contains a distribution of volume charge with the density ρ that is determined by the equilibrium positions of the counter- and co-ions [3]. A very long history of development of the so-called continuum models for the structure of electric double layers has produced several models that have gained wide acceptance as good starting point in modeling the biochemical sensors based on the so-called ion-sensitive field effect transistors (ISFETs) [12]. In contrast to the traditional silicon based ISFETs, graphene shows great promise because it is hydrophobic and hence its detection sensitivity to external charges may be enhanced by bringing graphene in direct contact with an aqueous solution without disrupting its electronic band structure. Moreover, the process of capacitative gating of graphene through an electrolyte proved to be much more effective than the traditional doping by the use of a metal back gate separated by thick oxide layer from graphene. Finally, graphene may be doped to the surface density of charges on the order of 10^{13} cm^{-2} or more electrons or holes, which is rather large compared to the typical interface between a metal electrode and electrolyte that is studied in electrochemistry.

The simplest class of continuum models of electrochemistry is based on equilibrium distribution (at finite temperature) of dissolved salt ions based on the Boltzmann distribution,which considers ions as point charges and the solvent (water) as continuous background with a spatially uniform dielectric constant. This picture is acceptable at relatively small ion concentrations and small surface charge density on the electrode. It gives rise to the well-known Poisson-Boltzmann model for the electrostatic potential in electric double layer with a diffuse layer of charge, which provides the screening mechanism that is named after Debye, with a typical screening length of about $3/\sqrt{c_0}$, given in Angstroms when the salt concentration is given in Moles per liter.

However, since the dissolved ions are, in fact, hydrated, i.e., each ion is surrounded by a layer of oriented dipoles representing water molecules, the effective ion sizes are quite large

(on the order of several Angstroms) [3]. Thus, modeling the structure of electric double layer close to a charged electrode needs to take into account the finite ion sizes, or the so-called steric effects, especially for high ion concentrations and large surface charge density that may arise when graphene is used as an ISFET. A phenomenological modification of the Poisson-Boltzmann model is provided by the so-called Stern layer next to the electrode (graphene), with the thickness on the order of the hydrated ion radius, which represents a minimum distance at which those ions can approach the charged surface. Thus, Stern layer is considered to be free of charges and it separates the diffuse layer with mobile ions from the charged electrode (graphene) surface. While the simple Poisson-Boltzmann model gives rise to unreasonably high ion concentration at charged surface, the modification due to Stern layer helps alleviate this effect of ion crowding. To overcome the shortcomings of phenomenological models such as Stern layer, a whole class of better founded modifications of the Poisson-Boltzmann was developed over many years [76, 77]. Probably the most broadly acknowledged is a model that may be called Bikerman-Freise model [3], which predicts a distribution of salt ions in the form of a Fermi distribution owing to their finite size, and introduces a parameter that defines the maximum density of salt ions.

In addition, when graphene is doped to a large charge carrier density by applying the potential drop across the electrolyte on the order of 1 V or even more, a relatively large electric field may arise close to the surface of graphene, which may cause a decrease in the dielectric constant of water. Since the very large relative dielectric constant of ≈ 80 in the bulk water at zero field is a consequence of the orientational degrees of freedom of permanent dipole moments associated with water molecules, it is conceivable that those degrees will be partially locked by the presence of a strong electric field close to the electrode surface. This dielectric decrement, or saturation of dielectric constant in water may be modeled phenomenologically by assigning a value to the relative dielectric constant of water inside the Stern layer, which is much small than its bulk value. In this manner, the Stern layer would represent a layer of water molecules represented by electric dipoles that are predominantly oriented towards or away from the charged surface. This additional role of Stern layer in electrochemistry is certainly a very useful modification of the Poisson Boltzmann model, but it renders phenomenological modeling of both its thickness and its effective dielectric constant quite uncertain. In view of that, there has been a long history of attempts to describe the dielectric behavior of water in high electric fields [45, 46, 78]. Probably the most appreciated and frequently tested in computer simulations of the structure of water is the model due to Booth, which may be for historic reasons also called Grahame-Booth model for dielectric saturation of water [3], which takes into account the statistical nature of the the orientational ordering of the water dipoles.

While the Bikerman-Freise model for ion steric effects and Grahame-Booth model for dielectric saturation have been time honored modifications to the Poisson-Boltzmann model of electric double layer in aqueous solutions, it is somewhat unsettling that those two models were derived within different theoretical frameworks. Accrodingly, there were several attempts to describe both the steric effects and dielectric saturation within the same framework [78]. While the outcomes of such attempts are not always as successful in prac-

tical applications as the original models of Bikerman-Freise and Grahame-Booth, they are nevertheless worthy analyzing for future reference.

Since the above two modifications of the Poisson-Boltzmann model for graphene in an ISFET configuration are critically important for considering the screening properties of graphene in the presence of mobile ions, as well as for its capacitative gating in an electrolyte, we provide in this chapter a few details on their mathematical formulation.

4.1 Poisson-Boltzmann (PB) equation

The Poisson Equation when combined with the Boltzmann distribution yields the PB equation. The PB equation is a nonlinear partial differential equation that describes electrostatic interactions between molecules in ionic solutions. PB equation is the mathematical base for the Gouy-Chapman double layer (interfacial) theory, first proposed by Gouy in 1910 and complemented by Chapman in 1913. The distribution of the electrostatic potential $\Phi(\mathbf{R})$ in $3D$ is defined by the Poisson Equation

$$\nabla \cdot [\epsilon \nabla \Phi] = -4\pi\rho, \tag{4.1}$$

where ϵ is the dielectric constant of the medium. ρ is the mean charge density of mobile ions given as

$$\rho = \sum_i Z_i e c_i, \tag{4.2}$$

where $Z_i e$ is the charge on the ith ionic species and c_i is the mean concentration assumed to be given by the Boltzmann distribution,

$$c_i(\Phi) = c_i^0 e^{-Z_i e\Phi/k_B T}. \tag{4.3}$$

In the above equation, c_i^0 is the bulk concentration, k_B is the Boltzmann constant and T is the absolute temperature. We use the Gaussian units ($4\pi\epsilon_0 = 1$) throughout our work and assume room temperature giving $k_B T = 0.025$ eV.

Considering a symmetric binary electrolyte ($Z_\pm = \pm Z$, $c_+^0 = c_-^0 = c_0$), we get the standard form of PB equation as

$$\nabla \cdot [\epsilon \nabla \Phi] = -4\pi\rho(\Phi) = 8\pi c_0 Ze \ \sinh(Ze\Phi/k_B T), \tag{4.4}$$

which may be called the non-linearized PB model.

Assuming the potential variation is small and/or that the temperature is high, that is, $|Ze\Phi|/k_B T \ll 1$, Eq. (4.3) may be linearized to give

$$c_i(\Phi) \approx c_i^0(1 - Z_i e\Phi/k_B T), \tag{4.5}$$

which yields the Debye-Hückel approximation or the linearized PB model. Assuming that the relative dielectric constant of the solvent, ϵ, is independent of the position, this model gives the Helmholtz equation of the form

$$\nabla^2\Phi = \kappa^2\Phi, \tag{4.6}$$

where we defined inverse Debye screening length as

$$\kappa = \sqrt{\frac{8\pi\beta Z^2 e^2 c_0}{\epsilon}}. \tag{4.7}$$

While being of limited validity as regards the ranges of parameters, the linearized PB eqution in Eq. (4.6) allows analytical solutions in various geometries. On the other hand, the nonlinear PB equation in Eq. (4.4) may only be solved analytically for a one-dimensional dependence, which is fortunately of relevance for graphene based ISFETs, where one may assume that a relatively large area of graphene is exposed to a thick and laterally uniform layer of electrolyte.

4.2 Modified PB (MPB) model involving steric effects

The standard PB model is valid for point-like ions. As far as we are dealing with high ion concentration or dilute electrolytes in large applied voltages, we have to consider the effects of finite ion size or steric effects. J. J. Bikerman, in 1942, came up with a thorough MPB model with steric effects in an excellent, but poorly known paper [40].

To start deriving MPB equation taking into account the steric effects in electrolytes, the first step is to write [76] the expression for the total free energy. Within mean field approximation, the total energy,

$$F_{MPB} = U - TS, \tag{4.8}$$

for a symmetric binary electrolyte may be expressed [76, 79] with reference to local electrostatic potential Φ and the ion concentrations $c_{\pm}$. The share of the electrostatic energy U [76] is

$$U = \iiint d^3\mathbf{r}\left[-\frac{\epsilon}{8\pi}(\nabla\Phi)^2 + (c_+ - c_-)Ze\Phi - \mu_+ c_+ - \mu_- c_-\right]. \tag{4.9}$$

Here, the first term is the self-energy of the electric field, and ϵ is the relative dielectric constant of the solution [76]. The next two terms are the electrostatic energies of the ions [76]. The last two terms express the constraint of conservation of the number of ions, with the Lagrange multipliers $\mu_{\pm}$ which will be related to the chemical potentials of ionic species in the bulk of the electrolyte [76].

The entropic contribution $-TS$ is [76]

$$-TS = \frac{k_BT}{a^3}\iiint d^3\mathbf{r}\Big[a^3c_+\ln(a^3c_+) + a^3c_-\ln(a^3c_-) + (1-a^3c_+-a^3c_-) \ln(1-a^3c_+-a^3c_-)\Big]. \tag{4.10}$$

In the above equation, the first two terms represent the entropies of the positive and negative ions[76], where we assume that the sizes of the co-ions and counter-ions are same and equal to a. However, the last term corresponds to the entropy of the solvent molecules [76]. In fact, the last term is accountable for the atypical steric corrections to the PB equation [76]. As a matter of fact, these corrections are accomplished taking into account a lattice-gas version of the Coulomb gas that considers each lattice site being occupied partially by one ion [76, 77]. In the limit $a \longrightarrow 0$, we recover expression for free energy with the PB model. The above total free energy is a functional of the three independent fields: $c_\pm$ and Φ.

Minimizing the above free energy functional leads to the thermodynamic equilibrium state. Considering the variation of the free energy with respect to $c_\pm$ results in the Boltzmann distributions of the ions in the presence of the local potential Φ:

$$\frac{\delta F_{MPB}}{\delta c_\pm} = \pm eZ\Phi + k_BT\ln(a^3c_\pm) - k_BT\ln(1-a^3c_+-a^3c_-) - \mu_\pm = 0, \tag{4.11}$$

wherefrom the local ion densities are

$$c_\pm = c_0\frac{\exp(\mp eZ\Phi/k_BT)}{1-\nu+\nu\cosh(eZ\Phi/k_BT)}, \tag{4.12}$$

where $\nu = 2c_0a^3$ is the bulk volume fraction of the ions. The last two terms couple the system to a bulk reservoir [76]. $\mu_\pm$ are the size-modified chemical potentials for the ionic species given as

$$\mu_\pm = k_BT\ln\frac{a^3c_0}{1-2a^3c_0}. \tag{4.13}$$

Similarly taking the variation with respect to the potential Φ yields the Poisson equation connecting Φ with the ion densities:

$$\frac{\delta F_{MPB}}{\delta\Phi} = \frac{\epsilon}{4\pi}\nabla^2\Phi + eZc_+ - eZc_- = 0. \tag{4.14}$$

Hence the MPB equation for symmetric electrolytes is written as:

$$\nabla^2\Phi = \frac{8\pi eZc_0}{\epsilon}\frac{\sinh(eZ\Phi/k_BT)}{1-\nu+\nu\cosh(eZ\Phi/k_BT)}. \tag{4.15}$$

In Fig. (4.1) we show the effects of increasing potential drop Ψ_D across the diffuse part

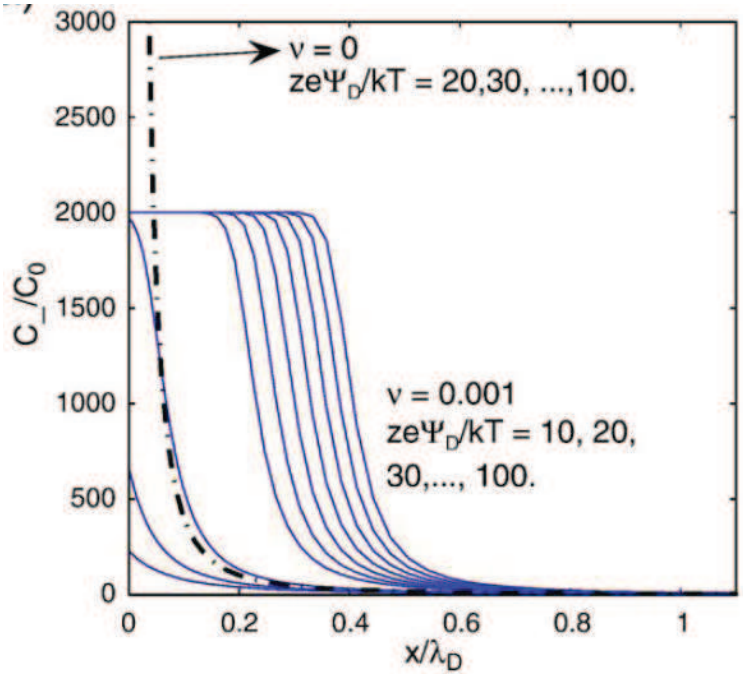

Figure 4.1: Relative concentration of negative ions as a function of the distance (in units of the Debye screening length $\lambda_D \equiv \kappa^{-1}$) from a positively charged electrode for several values of the potential drop Ψ_D across the diffuse part of electrolyte, when the bulk volume fraction of the ions $\nu = 2c_0a^3$ takes values 0.001 (solid curves) and 0 (dash-dotted curve). Adapted from Ref. [3].

of electrolyte on the concentration of negative ions in front of a positively charged surface for the bulk volume fraction of the ions $\nu = 2c_0a^3 = 0.001$, according to the solution of Eq. (4.15). Also shown are the result from the Poisson-Boltzmann model by setting $\nu = 2c_0a^3 = 0$ [3]. We can clearly interpret the results by observing that the ion densities saturate for large values of the electrostatic potential. Hence, the ion densities hinder the values of the electrostatic potential from reaching the unphysical values that can be obtained in the standard PB theory.

4.3 Dielectric saturation of water in high electric field

The local dielectric constant of an electrolyte is generally reduced in the inner part of the double layer, as confirmed from experimental fitting data with simple models, because of the alignment of the solvent dipoles in the large local electric field [3]. This effect is called the dielectric saturation. In aqueous solutions, the compact Stern layer is inferred to have an effective permittivity ϵ_s smaller than that of bulk water ϵ_b by approximately an order of magnitude, e.g. reduced from $\epsilon_b = 78\epsilon_0$ to about $\epsilon_s = 6\epsilon_0$ [3, 80]. We shall also study the dielectric saturation within the PB theory through the different models given below.

4.3.1 Grahame-Booth model

Grahame [45] was perhaps the pioneer to assess the structure of the diffuse layer with an electric-field-dependent permittivity, utilizing PB theory and the empirical form

$$\epsilon(E) = \epsilon_s + \frac{\epsilon_b - \epsilon_s}{\left(1 + (E/E_s)^2\right)^m}, \tag{4.16}$$

where E is the magnitude of electric field, m is an empirical exponent, assumed to be in the range $0 < m < 2$ to avoid exceedingly abrupt onset of dielectric saturation above the characteristic field strength E_s.

Nearly half a century ago, Booth [46] obtained the following expression for the field-dependent dielectric constant of water by extending the Onsager and Kirkwood theories of polar dielectrics

$$\epsilon_r(E) = n_w^2 + \frac{28\pi c_{0w}\alpha(n_w^2+2)}{3\sqrt{73}E}\, L\left[\frac{\sqrt{73}E\alpha(n_w^2+2)}{6k_BT}\right], \tag{4.17}$$

where n_w is optical refractive index of water (≈ 1.33), c_{0w} is the number density of water molecules (55 mol/l), and α is the magnitude of the water dipole moment. $L(x) = \coth(x) - \frac{1}{x}$ is the Langevin function. Eq. (4.17) is the expression for relative permittivity for point like ions taking into consideration the cavity and reaction fields and the structural correlations between water dipoles [46]. In the limit of vanishing electric field, the above equation reduces to

$$\epsilon_r \approx n_w^2 + \frac{14\pi c_{0w}\alpha^2\beta(n_w^2+2)^2}{27}, \tag{4.18}$$

where $\beta = \frac{1}{k_BT}$. It follows from the above equation that the dipole moment of water $\alpha = 2.03$ D (Debye units) corresponds to bulk permittivity $\epsilon_r = 78.5$ at room temperature. In Fig. (4.2) we show a comparison of the relative dielectric constant of water as a function of the electric field evaluated with the Booth model with the dipole moment of

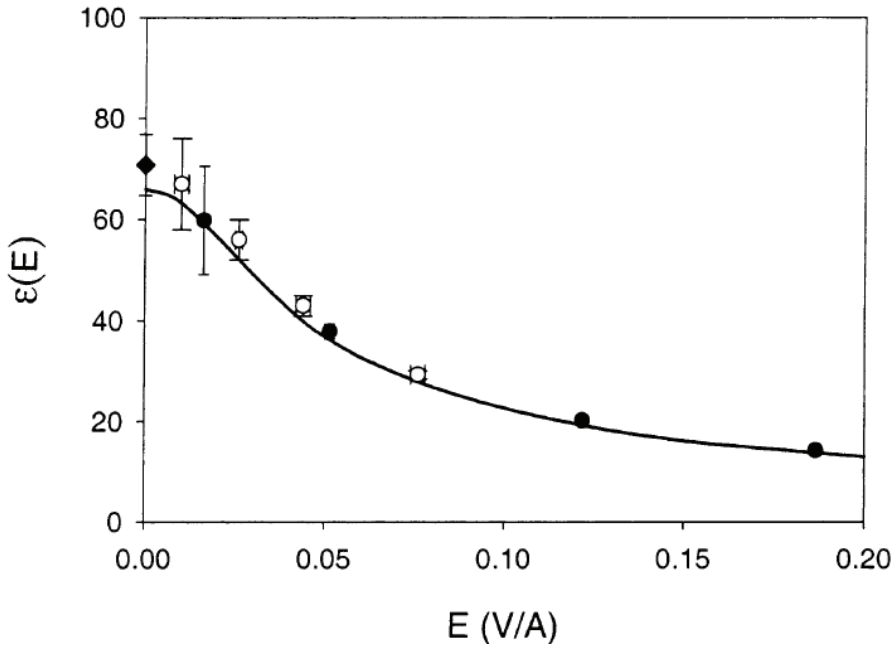

Figure 4.2: A diagram showing comparison of the Booth model (solid curve) with several computer simulations (data symbols) for the relative dielectric constant of water as a function of the electric field. Booth model was calculated with the dipole moment for water molecules of 1.85 D. Adapted from Ref. [4].

$\alpha = 1.85$ D with several results from computer simulations using the Molecular Dynamics method [4]. One notices that, while the zero field value of the dielectric constant is slightly underestimated by the Booth model with this somewhat lower value of α, the agreement with the data at high fields is quite remarkable.

4.3.2 Unified model for steric effects and dielectric saturation

It should be noticed that the Booth model considers the salt ions as point charges. In order to include the effects of finite ion size into the theory of dielectric saturation of the dielectric constant of water, Gongadze *et al.* [78] used a lattice gas model taking into account the orientational ordering of water molecules near planar electrode. The number densities of water molecules (c_{0w}), counterions (c_0) and co-ions (c_0) are constant in bulk solution

(where $x \longrightarrow \infty$); therefore, their number densities may be expressed [78] by calculating the corresponding probabilities that a single lattice site is occupied by one of the three particle types in the electrolyte solution (counterions, co-ions and water molecules):

$$c_+(x \longrightarrow \infty) = c_-(x \longrightarrow \infty) = c_s \frac{c_0}{c_0 + c_0 + c_{0w}}, \tag{4.19}$$

$$c_w(x \longrightarrow \infty) = c_s \frac{c_{0w}}{c_0 + c_0 + c_{0w}}, \tag{4.20}$$

where $c_s = 2c_0 + c_{0w} = \dfrac{1}{a^3}$, is defined as the number density of lattice sites. Also, a is the width of a single lattice site. The charged surface at $x = 0$ affects the number densities of monovalent ions ($Z = 1$) and water molecules, so the probabilities that a single lattice site is occupied by one of the three kinds of particles at finite distance x should be corrected by the corresponding Boltzmann factors [78]

$$c_+(x) = c_s \frac{c_0 e^{-e\Phi\beta}}{c_0 e^{-e\Phi\beta} + c_0 e^{e\Phi\beta} + c_{0w}\left\langle e^{-\alpha E\beta\cos\omega}\right\rangle_\omega}, \tag{4.21}$$

$$c_-(x) = c_s \frac{c_0 e^{e\Phi\beta}}{c_0 e^{-e\Phi\beta} + c_0 e^{e\Phi\beta} + c_{0w}\left\langle e^{-\alpha E\beta\cos\omega}\right\rangle_\omega}, \tag{4.22}$$

$$c_w(x) = c_s \frac{c_{0w}\left\langle e^{-\alpha E\beta\cos\omega}\right\rangle_\omega}{c_0 e^{-e\Phi\beta} + c_0 e^{e\Phi\beta} + c_{0w}\left\langle e^{-\alpha E\beta\cos\omega}\right\rangle_\omega}, \tag{4.23}$$

where $\left\langle e^{-\alpha E\beta\cos\omega}\right\rangle_\omega$ is the dipole Boltzmann factor after rotational averaging over all possible angles ω with respect to the x-axis, and is given as [78]

$$\left\langle e^{-\alpha E\beta\cos\omega}\right\rangle_\omega = \frac{2\pi\int_0^1 d(\cos\omega) e^{-\alpha E\beta\cos\omega}}{4\pi} = \frac{\sinh(\alpha E\beta)}{\alpha E\beta}. \tag{4.24}$$

Using the definition [78]

$$H(\Phi, E) = 2c_0\cosh(e\Phi\beta) + c_{0w}\frac{\sinh(\alpha E\beta)}{\alpha E\beta}, \tag{4.25}$$

Eqs. (4.21)-(4.23) may be rewritten [78, 81, 82] as

$$c_+(x) = c_0 e^{-e\Phi\beta}\frac{c_s}{H}, \tag{4.26}$$

$$c_-(x) = c_0 e^{e\Phi\beta}\frac{c_s}{H}, \tag{4.27}$$

$$c_w(x) = \frac{c_{0w}c_s}{H}\frac{\sinh(\alpha E\beta)}{\alpha E\beta}. \tag{4.28}$$

In the case of finite sized ions, Gongadze *et al.* [5, 78] derived the polarization $P(x)$ of water as

$$P(x) = c_w(x)\langle \mathbf{p}(x,\omega)\rangle_B = -\frac{c_{0w}c_s}{HE\beta}\sinh(\alpha E\beta)L(\alpha E\beta), \tag{4.29}$$

where $\mathbf{p}(x,\omega)$ is the water dipole moment vector at coordinate x and $\langle \mathbf{p}(x,\omega)\rangle_B$ is the average of $\mathbf{p}(x,\omega)$ over the angle distribution in thermal equilibrium at given x, given by [5]

$$\langle \mathbf{p}(x,\omega)\rangle_B = \frac{\int_0^\infty \alpha\cos\omega\exp(-\alpha E\beta\cos\omega)2\pi\sin\omega d\omega}{\int_0^\infty \exp(-\alpha E\beta\cos\omega)2\pi\sin\omega d\omega} = -\alpha L(\alpha E\beta). \tag{4.30}$$

The relative permittivity of the electrolyte solution takes the form [81, 82]

$$\epsilon_r(x) = 1 + 4\pi\frac{\mid P \mid}{E} = 1 + 4\pi c_s c_{0w}\alpha\frac{F(\alpha E\beta)}{H(\Phi,E)E}, \tag{4.31}$$

where

$$F(y) = L(y)\frac{\sinh y}{y}. \tag{4.32}$$

The expression for the relative permittivity defined by Eq. (4.31) for zero electric field strength and zero potential, i.e. the bulk value of ϵ_r is given as [83]

$$\epsilon_r = 1 + \frac{4\pi c_{0w}\alpha^2\beta}{3}, \tag{4.33}$$

which in turn gives $\epsilon_r = 78.5$ corresponding to $\alpha = 4.9D$, which is unrealistically large.

In the next improvement of their unified approach, Gongadze *et al.* [84] derived an expression for the relative permittivity of an electrolyte from Eqs. (4.31)-(4.32) in saturation regime (i.e. near the highly charged surface) considering orientational ordering of water and excluded volume effects due to accumulation of counterions as follows:

$$\epsilon_r(x) = n_w^2 + \frac{4\pi c_s c_{0w}\alpha(2+{n_w}^2)F(\delta\alpha E\beta)}{3ED(\Phi,E)}, \tag{4.34}$$

where

$$D(\Phi,E) = 2c_0\cosh(e\Phi\beta) + c_{0w}\frac{\sinh(\delta\alpha E\beta)}{\delta\alpha E\beta}, \tag{4.35}$$

$$\delta = \frac{2+{n_w}^2}{2}. \tag{4.36}$$

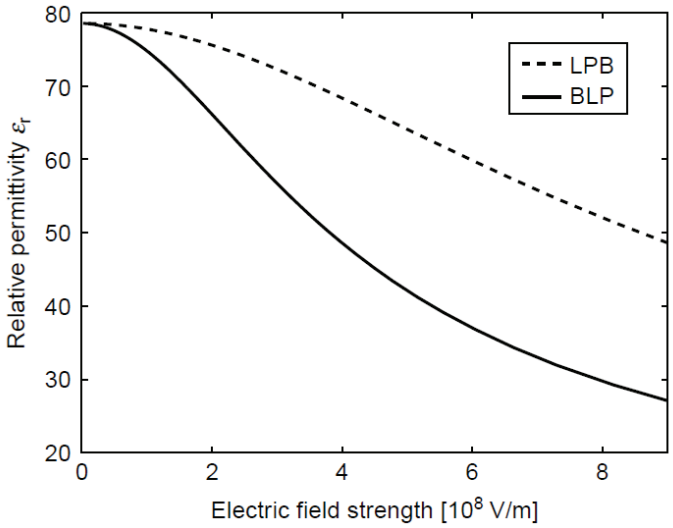

Figure 4.3: A diagram showing a comparison of the Booth model (solid curve labeled BLP) with the model in Eq. (4.34) (dashed curve labeled LPB) for relative dielectric constant of water as a function of the electric field. While the Booth model was calculated with the dipole moment for water molecules of $\alpha = 2.03$ D, the LPB model was calculated with $\alpha = 4.794$. Adapted from Ref. [5].

Eq. (4.34) reduces to Onsager expression for bulk permittivity (in the limit of zero electric field and zero potential) as follows:

$$\epsilon_r \approx n_w^2 + \frac{2\pi c_{0w}\alpha^2\beta(n_w^2+2)^2}{9}. \tag{4.37}$$

Eq. (4.37) gives $\epsilon_r = 78.5$ corresponding to $\alpha = 3.1$ D. This value of α is much smaller than the value obtained in lattice gas model [5], but is still higher than the value corresponding to Booth's model [46]. In fact, this value of α is much closer to the experimental values of the effective dipole moment of water molecules in clusters ($\alpha = 2.7$ D) and in bulk solution ($\alpha = 2.4 - 2.6$ D) [78]. In Fig. (4.3) one can see that the result reported in Eq. (4.34) for the model that includes the finite ion size effect into the theory of dielectric saturation of water requires unrealistically large dipole moment of $\alpha = 4.794$ D in order to reproduce the zero field value, which in turn overestimates the values at high fields that were reported in Fig. (4.2) from computer simulations. It appears that, while the authors in Refs. [5, 81, 78] succeeded in providing a unified treatment of the steric and dielectric saturation models, the quantitative utility of their result for the dielectric constant of water

seems to be inferior to that of the Booth model. We shall therefore adopt the latter model in our study of the capacitance of electrolytically gated graphene sheet.

Finally, for electric double layer in an electrolyte near charged wall, the PB equation may be written in a more general form as

$$\nabla \cdot [\epsilon_r(\mathbf{r}) \nabla \Phi(\mathbf{r})] = -4\pi\rho(\mathbf{r}), \tag{4.38}$$

where $\rho(\mathbf{r})$ is the macroscopic volume charge density of coions and counterions given as [84]

$$\rho(\mathbf{r}) = ec_+(\mathbf{r}) - ec_-(\mathbf{r}) = -2ec_s c_0 \frac{\sinh(e\Phi\beta)}{D(\Phi, E)}, \tag{4.39}$$

whereas reduced dielectric constant in the electrolyte $\epsilon_r(\mathbf{r})$ is defined by Eq. (4.34). The boundary condition at the charged surface is

$$\epsilon_r(\mathbf{r} = \mathbf{r}_s)\, \hat{\mathbf{n}} \cdot \nabla \Phi(\mathbf{r} = \mathbf{r}_s) = -4\pi\sigma(\mathbf{r}_s), \tag{4.40}$$

where $\hat{\mathbf{n}}$ is a unit normal vector at the point $\mathbf{r}_s$ on the boundary surface and $\sigma(\mathbf{r}_s)$ is the surface charge density at that point. For a thick layer of electrolyte, deep in its bulk region we may impose a boundary condition far from the charged surface to be

$$\Phi(\mathbf{r} \longrightarrow \infty) = 0. \tag{4.41}$$

Chapter 5

Capacitance of graphene in aqueous electrolytes: the effects of dielectric saturation of water and finite size of ions

The concept of electrostatic capacitance is important for understanding of the electrochemical charging of graphene based FETs through a double layer in the electrolyte. The experiments usually determine the differential capacitance per unit area. In the present context, capacitance arises from two different origins: the classical electrostatics which treats the double layer as a planar capacitor and the so-called quantum capacitance. The electrostatic capacitance comes from the mutual Coulomb repulsion of electrons resulting in a nonzero potential across the double layer, which is associated with the charging of graphene. The concept of quantum capacitance comes from the Pauli exclusion principle in graphene, which forces electrons to occupy all energies up to the Fermi level, leading to an increase in the internal electrical potential in graphene. Those two contributions are usually viewed as two capacitors connected in series, so that the smaller one dominates the total capacitance. When graphene is doped by a back gate, its electrostatic capacitance is very small because of a typically very thick ($\sim$ 300 nm) oxide layer between the gate and graphene. Thus, for a back-gated graphene the electrostatic capacitance dominates the total capacitance and the quantum capacitance contribution is negligible. In contrast, for an electrolytically top gated graphene, the electrostatic capacitance is comparable to the quantum capacitance of graphene, so the quantum contribution must be taken into account.

In this chapter, we present a theoretical model for electrolytically top gated graphene, in which we analyze the effects of dielectric saturation of water due to possibly strong electric fields near the surface of a highly charged graphene, as well as the steric effects due to finite size of salt ions in an aqueous electrolyte. We also assess the effects of the nonlinearity arising in the density of states of graphene as the chemical potential μ in

graphene increases. By combining the Bikerman-Freise model for the steric effects and the Grahame-Booth model for dielectric saturation, we show that the total capacitance of the solution-gated graphene is dominated by its quantum capacitance for gating potentials $\lesssim 1$ V, which is the range of primary interest for most sensor applications of graphene. It also happens that the linear approximation to the density of states of graphene works well for chemical potential values $|\mu| \lesssim 1$ V, validating the picture of graphene π-electron bands as Dirac fermions. The corresponding range of doping densities of graphene in electrolytically top gated graphene is $|n| \lesssim 7 \times 10^{13}$ cm^{-2}. On the other hand, at the gating potentials $\gtrsim 1$ V the total capacitance is dominated by a universal capacitance of the electric double layer in the electrolyte, which exhibits a dramatic decrease of capacitance with increasing gating potential due to interplay of a fully saturated dielectric constant of water and ion crowding near graphene. This dominance of the electric double layer capacitance completely overcomes an increase in the graphene quantum capacitance due to nonlinearity of its density of states for chemical potentials $|\mu| \gtrsim 1$.

5.1 Theory

We consider a three-layer structure with an x axis perpendicular to the plane of graphene, which is placed at $x = 0$, and assume that the structure is homogeneous in directions parallel to graphene. We further assume that a metallic electrode is held at an electric potential $\phi_{\rm bg}$ and is placed at $x = -t$, where t is the thickness of an oxide substrate with relative dielectric constant ϵ_1, which occupies region 1 defined by $-t \le x \le 0$, as shown in Fig. 5.1. A Stern layer (SL) is assumed to occupy region 2 defined by $0 \le x \le h$, and is characterized by a relative dielectric constant ϵ_2, whereas a semi-infinite diffuse layer (DL) fills region 3 defined by $x \ge h$, which is characterized by a relative dielectric constant of the solvent ϵ_3, with the potential in the bulk of the electrolyte chosen to be a zero reference potential. Furthermore, we allow for the existence of fixed charged impurities in the region 1, which are ubiquitous in typical substrates used for graphene devices [74, 75]. Thus, in the region 1 we may have a charge density $\bar{\rho}_{\rm imp}(x)$ describing those impurities, which is obtained by averaging the full density of impurities over a large area parallel to graphene [30]. We note that the SL is assumed to be free of charge, by definition, whereas its parameters h and $\epsilon_2 \le \epsilon_3$ may represent, in a qualitative manner, the effect of finite size of ions giving rise to a minimum distance $\sim h$ of approach to graphene and the effect of dielectric saturation of water due to a possibly high electric field close to graphene [16]. Alternatively, the parameters h and ϵ_2 may represent a thin dielectric layer placed on top of graphene to insulate it from the solution [42].

We seek a solution of the Poisson equation for the electric potential that is defined in a piece-wise manner as

$$\phi(x) = \phi_j(x), \tag{5.1}$$

when x is in the jth region. In the regions 1 and 2, the corresponding functions are

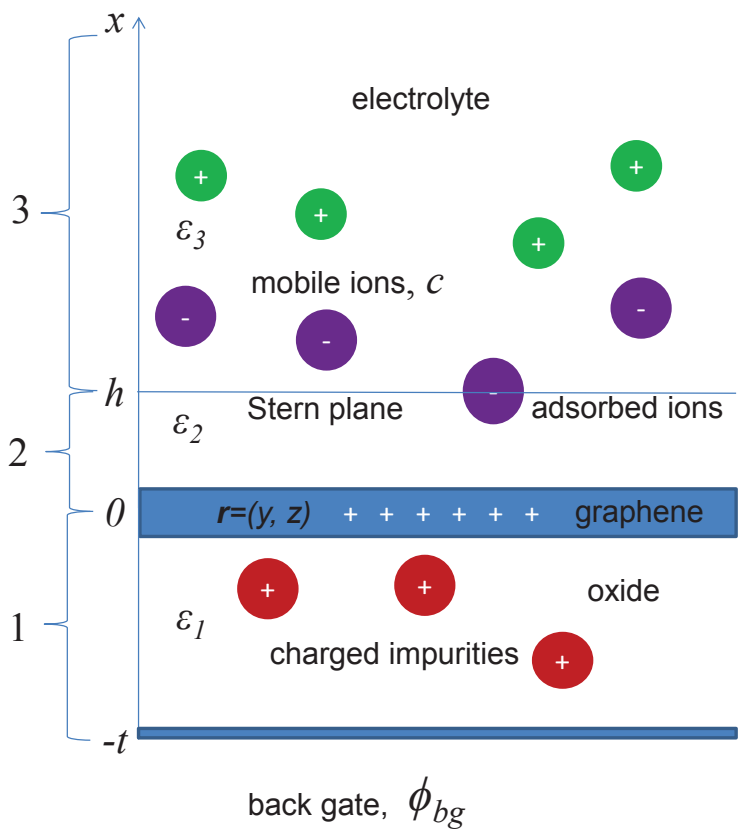

Figure 5.1: A diagram showing the configuration of the system studied, with the region 1, $-t < x < 0$, representing an oxide layer with dielectric constant ϵ_1 that contains fixed charged impurities, region 2, $0 < x < h$, representing a charge-free Stern layer with dielectric constant ϵ_2, and the region 3, $x > h$, representing a diffuse layer, which contains mobile ions in a semi-infinite electrolyte with the solvent dielectric constant ϵ_3. A single layer of graphene occupies the plane $x = 0$, whereas specific adsorption of ions is assumed to take place in the outer Helmholtz (or Stern) plane at $x = h$. $\phi_{\rm bg}$ is the electrostatic potentials at the back gate, $x = -t$, whereas the potential in the bulk electrolyte, $x \to \infty$, is assumed to be zero.

solutions of the equations

$$\epsilon_1 \frac{d^2\phi_1}{dx^2} = -4\pi\bar{\rho}_{\rm imp}(x), \qquad -t < x < 0 \tag{5.2}$$

and

$$\frac{d^2\phi_2}{dx^2} = 0, \qquad 0 < x < h \tag{5.3}$$

whereas $\phi_3(x)$ is to be determined from the Gauss' law in region 3,

$$\frac{d}{dx}\left[\epsilon_3\left(|E_3|\right)\,E_3\right] = 4\pi\rho_3\left(\phi_3\right), \qquad x > h \tag{5.4}$$

where

$$E_3(x) = -\frac{d\phi_3}{dx}, \tag{5.5}$$

is the x component of the electric field in the DL. In the spirit of a local-density approximation, we assume that the ionic charge density in the right-hand side of Eq. (5.4) is given for a symmetric $Z:Z$ electrolyte by the so-called Fermi distribution of the BF model [3, 43]

$$\rho_3\left(\phi\right) = -\frac{2Zec_0\sinh\left(\beta Ze\phi\right)}{1+2\nu\sinh^2\left(\beta Ze\phi/2\right)}, \tag{5.6}$$

where $e > 0$ is the proton charge, c_0 is the salt concentration in the bulk of the DL, $\beta = 1/\left(k_BT\right)$ is the inverse thermal energy, for which we adopt the room temperature value of $k_BT \approx 0.025$ eV throughout this work, and $\nu = 2a^3c_0$ is the packing fraction of the solvated ions, for which we assume equal diameters of $a \approx 7.1$ Å in this work. Notice that the limit of point ions with $a = 0$ and hence $\nu = 0$ gives the usual result for ionic density that follows from the Boltzmann distribution. On the other hand, in the regions of a solution with finite-sized ions where the local potential is large enough, $\beta Ze|\phi| \gg \ln(2/\nu)$, the ionic density saturates at the value $\rho_3 \to Zec_{\max}$, where $c_{\max} = 1/a^3$ is a maximum concentration of ions of either kind, which describes the regime of ion crowding due to steric effects.

In the left-hand side of Eq. (5.4) we assume that the dielectric constant of solvent in region 3 is a function of the magnitude of the electric field, which may be modeled by the Booth model as [5, 47, 48, 49, 50, 51]

$$\epsilon_3\left(E\right) = n_w^2 + \left(\epsilon_b - n_w^2\right)\,\frac{3}{\gamma E}\left[\coth\left(\gamma E\right) - \frac{1}{\gamma E}\right], \tag{5.7}$$

where $n_w \approx 1.33$ is the optical refractive index of water, $\epsilon_b \approx 80$ its bulk dielectric constant in the zero-field limit, and

$$\gamma = \frac{\sqrt{73}}{6}\left(n_w^2+2\right)\alpha\beta \tag{5.8}$$

is the parameter that defines a critical electric field $E_s \equiv 1/\gamma$ for which the dielectric saturation sets in, with α being the effective dipole moment of water molecules, for which we adopt the value $\alpha \approx 2$ Debye, cited in literature [5, 46, 47, 48, 49, 50, 51]. We note that, when the local electric field in the electrolyte is much smaller than $E_s \approx 0.1$ V/nm, Eq. (5.7) gives $\epsilon_3 \approx \epsilon_b$, which in the limit of point ions in Eq. (5.6) gives rise to the standard

Poisson-Boltzmann (PB) model of DL [16]. In the opposite limit of high electric fields, $\gamma E \gg 1$, Eq. (5.7) gives a much smaller dielectric constant of water, $\epsilon_3 \approx n_w^2$, although it should be pointed out that this limit is only approached very slowly, according to the asymptotic form $\epsilon_3 \sim 1/(\gamma E)$.

The above equations for the potential components have to be solved subject to the boundary conditions, such that $\phi_1(-t) = \phi_{\rm bg}$ and $\phi_3 \to 0$ along with $E_3 \to 0$ when $x \to \infty$. In addition, the electrostatic matching conditions at $x = 0$ and $x = h$ impose the continuity of the potential, which takes the values $\phi_0 \equiv \phi_1(0) = \phi_2(0)$ and $\phi_h \equiv \phi_2(h) = \phi_3(h)$ at the graphene and Stern planes, respectively, as well as the jumps conditions for the x components of the dielectric displacements, which may be expressed as

$$-\epsilon_2 \left.\frac{d\phi_2}{dx}\right|_{x=0} + \epsilon_1 \left.\frac{d\phi_1}{dx}\right|_{x=0} = 4\pi\sigma_g(\phi_0)\,, \tag{5.9}$$

where $\sigma_g(\phi_0)$ is the surface charge density on graphene, and

$$\epsilon_3\left(E_3(h)\right)\, E_3(h) + \epsilon_2 \left.\frac{d\phi_2}{dx}\right|_{x=h} = 4\pi\sigma_a(\phi_h - \phi_0)\,, \tag{5.10}$$

where $\sigma_a(\phi_h - \phi_0)$ is the surface charge density resulting from specifically adsorbed ions at the position of the Stern plane at $x = h$ [3]. We note that both densities σ_g and σ_a are assumed to be functions of the averaged values of the potentials ϕ_0 and ϕ_h, thereby neglecting the potential fluctuations in the graphene and Stern planes due to discreteness of charge in the impurity layer in the oxide [74, 75] and discreteness of charge in the layer of specifically adsorbed ions [85]. While we shall not pursue here any further details related to the ion adsorption, it is remarkable that both the presence of graphene and the specifically adsorbed ions enter the model through the jump conditions, Eqs. (5.9) and (5.10).

5.1.1 Quantum capacitance of graphene

Referring to Eq. (2.38), the surface charge density on graphene is given by

$$\sigma_g(\phi_0) = -e\int_{-\infty}^{\infty} d\varepsilon\, \mathcal{D}(\varepsilon - \varepsilon_D)\left[\frac{1}{1+{\rm e}^{\beta(\varepsilon-\mu_{ge})}} - \frac{1}{1+{\rm e}^{\beta(\varepsilon-\varepsilon_{\rm D})}}\right], \tag{5.11}$$

where $\mathcal{D}(\varepsilon - \varepsilon_{\rm D})$ is the density of states (DOS) for graphene's π-electron bands (see, e.g., Eq. (14) of Ref. [1]), given in reference to the electron energy level at the Dirac point, whose position is determined by the surface potential on graphene as $\varepsilon_{\rm D} = -e\phi_0$, whereas μ_{ge} is the chemical potential in graphene with respect to the chemical potential in the reference electrode that is used to dope the graphene. Note that the charge density on graphene in Eq. (5.11) is, in fact, determined by the potential difference $V_q \equiv (\mu_{ge} - \varepsilon_{\rm D})/e = \phi_0 + \mu_{ge}/e$, which we call quantum potential because of its role in defining the quantum capacitance

(QC) of graphene as the differential capacitance per unit area, $C_q = -d\sigma_g/dV_q$. So, when $\beta e|V_q| \gg 1$, it follows from Eq. (5.11) that $C_q \approx e^2\mathcal{D}(e|V_q|)$, neglecting a small electron-hole asymmetry in the DOS about Dirac point [86]. On the other hand, for charge carrier densities in graphene up to about 10^{14} cm^{-2}, which are achieved when $|V_q| \lesssim 1$ V, it suffices to use linear approximation for the electron DOS given by Eq. (2.32) where $E = \varepsilon - \varepsilon_{\rm D}$ [1]. Using this approximation in Eq. (5.11) gives

$$\sigma_g(V_q) = \frac{2}{\pi}\frac{e}{\left(\hbar v_{\rm F}\beta\right)^2}\left[\mathrm{dilog}\left(1+\mathrm{e}^{\beta e V_q}\right) - \mathrm{dilog}\left(1+\mathrm{e}^{-\beta e V_q}\right)\right], \tag{5.12}$$

where dilog is the standard dilogarithm function, and hence

$$C_q = \frac{4e^2}{\pi\beta\left(\hbar v_{\rm F}\right)^2}\ln\left[2\cosh\left(\beta e V_q/2\right)\right]. \tag{5.13}$$

One sees that the QC has a minimum value of about 0.8 μF/cm^2 at $V_q = 0$ and exhibits a linear increase with the potential magnitude for $\beta e|V_q| \gtrsim 1$, which is a signature of the well-known Dirac-cone approximation for the π electron bands in the vicinity of the Dirac point [1, 39].

5.1.2 Capacitance of diffuse layer

We proceed by turning to the DL and integrating Eq. (5.4) once to obtain a relation between the potential ϕ_h and the electric field E_h, both evaluated at the Stern plane $x = h$. We assume that the electric field E_3 in the region 3 may be expressed in terms of the potential ϕ_3 in that region as $E_3(x) = E_3(\phi_3(x))$ and apply the Chain Rule on the left-hand side of Eq. (5.4) to get

$$\frac{d}{dx} = \frac{d\phi_3}{dx}\frac{d}{d\phi_3} = -E_3(\phi_3)\frac{d}{d\phi_3}. \tag{5.14}$$

As a consequence, we have a first-order differential equation with separated variables, which we integrate from the point deep into the diffuse layer where both $E_3 = 0$ and $\phi_3 = 0$ to the Stern plane. We obtain [3]

$$H(E_h) = p_3(\phi_h), \tag{5.15}$$

where the function H is defined by

$$H(E_h) = \int_0^{E_h}\left[E\frac{d\epsilon_3(E)}{dE} + \epsilon_3(E)\right]E\,dE \tag{5.16}$$

$$= \frac{1}{2}n^2E_h^2 + \left(\epsilon_b - n^2\right)\frac{3}{\gamma^2}\left\{\gamma E_h\coth\left(\gamma E_h\right) - 1 - \ln\left[\frac{\sinh\left(\gamma E_h\right)}{\gamma E_h}\right]\right\}, \tag{5.17}$$

while the electrostatic pressure in the DL is defined by

$$p_3\left(\phi_h\right) = -4\pi \int_0^{\phi_h} \rho_3(\phi)\, d\phi \tag{5.18}$$

$$= \frac{8\pi c_0}{\beta\nu} \ln\left[1 + 2\nu \sinh^2\left(\beta z e \phi_h/2\right)\right]. \tag{5.19}$$

In order to find an expression for the differential capacitance C_d of the DL, we use the Gauss' law to express the total surface charge density due to ions in the DL as

$$\sigma_d\left(\phi_h\right) = -\frac{1}{4\pi}\epsilon_3(E_h)\, E_h, \tag{5.20}$$

which allows us to calculate the capacitance as

$$C_d = -\frac{d\sigma_d}{d\phi_h} = -\frac{\rho_3\left(\phi_h\right)}{E_h}, \tag{5.21}$$

with the ionic charge density in the DL given in Eq. (5.6).

We now discuss several limiting special cases for the EDL capacitor. Note that, if the electric field at the Stern plane is small enough, $\gamma E_h \ll 1$, one has from Eq. (5.17) $H(E_h) \approx \frac{1}{2}\epsilon_b E_h^2$, so that Eq. (5.21) gives the DL capacitance as a function of the potential at the Stern plane as

$$C_d \approx -\rho_3\left(\phi_h\right) / \sqrt{2p_3(\phi_h)/\epsilon_b} \equiv C_{BF}, \tag{5.22}$$

which reproduces the BF expression for capacitance given by [3]

$$C_{BF} = C_D \frac{\sinh\left(\beta Z e |\phi_h|\right)}{\left[1 + 2\nu \sinh^2\left(\beta Z e \phi_h/2\right)\right] \sqrt{\frac{2}{\nu} \ln\left[1 + 2\nu \sinh^2\left(\beta Z e \phi_h/2\right)\right]}}, \tag{5.23}$$

where

$$C_D = \epsilon_b / \left(4\pi\lambda_D\right), \tag{5.24}$$

is the Debye capacitance that is achieved in the Debye-Hückel (DH) limit, $\beta Z e|\phi_h| \ll 1$, with $\lambda_D^{-1} = \sqrt{8\pi\beta Z^2 e^2 c_0/\epsilon_b}$ being the (inverse) Debye length of the electrolyte. If we take the limit of point ions in Eq. (5.23), $\nu \to 0$, then the BF capacitance takes the familiar form from the PB theory,$C_{BF} \approx C_{GC}$, where

$$C_{GC} = C_D \cosh\left(\beta Z e \phi_h/2\right), \tag{5.25}$$

is the Gouy-Chapman (GC) expression for capacitance [43].

On the other hand, it is interesting to consider the BF capacitance in Eq. (5.23) in the limit of a large potential at the Stern plane in the presence of ions with finite size, such

that $\beta e|\phi_h| \gg \ln(2/\nu)$. Then, the BF capacitance is found to decrease with increasing potential according to $C_{BF} \sim C_D/\sqrt{2\nu\beta e|\phi_h|}$ as a consequence of the ion crowding effect [3, 43]. Finally, if both the potential and the electric field are large at the Stern plane, $\beta e|\phi_h| \gg \ln(2/\nu)$ and $\gamma E_h \gg 1$, then it may be shown that the DL capacitance decreases with increasing potential according to a similar inverse-square-root formula, but with a magnitude reduced by a factor of $n_w/\sqrt{\epsilon_b} \approx 0.15$ compared to the weak-field case. The resulting limiting expression for capacitance, $C_{GBBF} \sim n_w\sqrt{z^2 e c_{\max}/(8\pi|\phi_h|)}$, may be considered as resulting from a Grahame-Booth-Bikerman-Freise formula because it describes the effects of both the dielectric saturation and finite ion size that are expected in the presence of a dense electrolyte near highly-charged surface of graphene.

In passing, we make a technical note on how to analyze the full expression in Eq. (5.21) without resorting to specific limiting cases. Namely, C_d in that equation cannot be expressed explicitly as a function of the potential ϕ_h because the function H in Eq. (5.17) cannot be inverted to give $E_h = H^{-1}(\phi_h)$, which could be then inserted in the right-hand side of Eq. (5.21). However, it is possible to invert the function p_3 in Eq. (5.19) to express the potential as $\phi_h = p_3^{-1}(E_h)$, which may be then substituted in the right-hand side of Eq. (5.21) to give the DL capacitance as a function of the electric field at the Stern plane, $C_d = C_d(E_h)$. Then, the relation between the capacitance C_d and the potential ϕ_h may be analyzed by considering those quantities as parametric functions of the field E_h.

5.1.3 Total capacitance

Finally, we return to studying the entire structure by following a procedure described in Ref. [30] By imposing the jump conditions in Eqs. (5.9) and (5.10) we obtain two relations,

$$(\phi_h - \phi_0)C_S = \sigma_a(\phi_h - \phi_0) + \sigma_d(\phi_h), \tag{5.26}$$

where $C_S = \epsilon_2/(4\pi h)$ is the capacitance of the Stern layer, and

$$(\phi_{\rm bg} - \phi_0)C_{\rm ox} = \sigma_{\rm imp} + \sigma_g(\phi_0) + \sigma_a(\phi_h - \phi_0) + \sigma_d(\phi_h), \tag{5.27}$$

where $C_{\rm ox} = \epsilon_1/(4\pi t)$ is the capacitance of the oxide layer, whereas $\sigma_{\rm imp}$ is the average surface charge density of the impurities in the oxide given by

$$\sigma_{\rm imp} = \int_{-t}^{0} dx \left(1 + \frac{x}{t}\right) \bar{\rho}_{\rm imp}(x). \tag{5.28}$$

We shall only consider top gating of graphene through an electrolyte by setting $\phi_{\rm bg} = \phi_0$ in the left-hand side of Eq. (5.27), in which case the vanishing of the right-hand side of that equation expresses charge neutrality of the entire structure.

We further note that the potential applied to a reference electrode in the bulk of the electrolyte in order to dope graphene is given by $V_a = \mu_{ge}/e$, where we neglect the potential

offsets, which only define the potential of zero charge in graphene (along with $\sigma_{\rm imp}$). Then, we may write $V_a = V_q + V_S + V_d$, where $V_S = \phi_h - \phi_0$ and $V_d = -\phi_h$ are the potential drops across the SL and DL, respectively. Hence, the inverse of the total differential capacitance is given by

$$C^{-1} \equiv -\frac{dV_a}{d\sigma_g} = -\frac{dV_q}{d\sigma_g} - \frac{dV_S}{d\sigma_g} - \frac{dV_d}{d\sigma_g} \tag{5.29}$$

$$= \frac{1}{C_q(V_q)} + \frac{1}{C_S} + \frac{1}{C_d(V_d)}\left[1 - \frac{1}{C_S}\frac{d\sigma_a(V_S)}{dV_S}\right]. \tag{5.30}$$

If one disregards specific adsorption by setting $\sigma_a = 0$ (or $\sigma_a =$ constant), one may see from Eq. (5.30) that the total capacitance corresponds to a series connection of the graphene QC, the SL capacitance and the DL capacitance. Finally, since the parameters of the SL are only empirically determined from case to case, we shall set $V_S = 0$ along with $h = 0$, so that the total capacitance is then simply given by the expression

$$C = \left[C_q(V_q)^{-1} + C_d(V_d)^{-1}\right]^{-1}, \tag{5.31}$$

which will be analyzed in the following section in conjunction with the relations $V_a = V_q + V_d$ and $\sigma_g(V_q) + \sigma_d(V_d) = 0$, with the surface charge densities in graphene and in the DL given via Eqs. (5.12) and (7.55), respectively.

5.2 Results and discussion

From now on, we only consider a monovalent symmetric electrolyte at room temperature, assume all the potentials to be positive without loss of generality, and we normalize them by means of the thermal potential, so that $\overline{V}_\xi = \beta e V_\xi$ for $\xi = a, q, d$,

5.2.1 Capacitance of diffuse layer

We first analyze the capacitance C_d of the DL as a function of the potential drop V_d across that layer in the presence of both steric effects due to finite ion sizes modeled by the BF formula and the dielectric saturation of water modeled by the Booth formula. In doing so, we parallel the analysis presented on page 63 of Ref. [3] where dielectric saturation was modeled by the Grahame's empirical formula, [45] expecting that our use of the Booth formula may give a somewhat more realistic description of dielectric saturation in aqueous solutions. We normalize the DL capacitance by the Debye capacitance, $\widetilde{C}_d = C_d/C_D$, where $C_D = \epsilon_b/(4\pi\lambda_D)$ may be written as $C_D \approx 230\sqrt{c}$ in the units of μF/cm^2, where c is the salt concentration expressed in the units of M (mole/liters). In addition to the parameter ν that controls the steric effect due to finite ion size, we introduce the parameter $\Gamma = \gamma/(\beta e \lambda_D)$ that is inversely proportional to the saturation electric field in the Booth formula Eq. (5.7). Thus, from $\gamma \approx 9$ nm/V and $\lambda_D \approx 0.31/\sqrt{c}$ given in nanometers, we

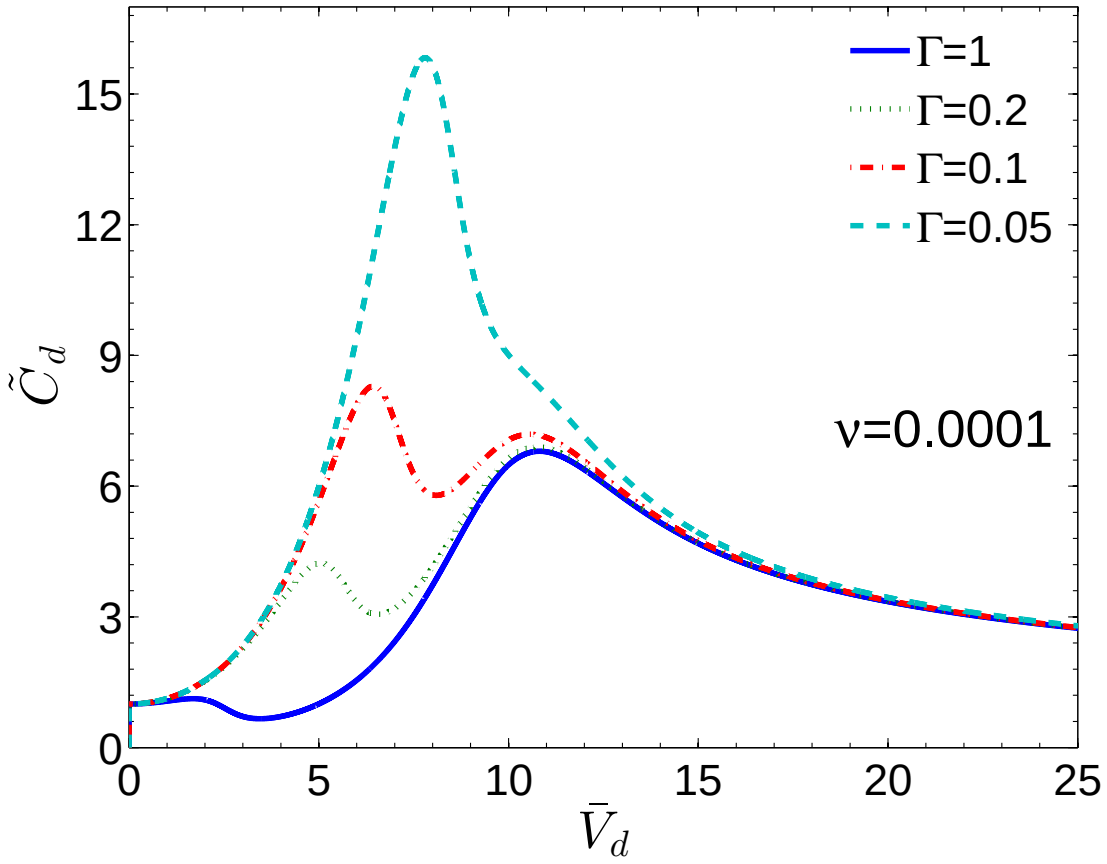

Figure 5.2: The capacitance of the diffuse layer normalized by the Debye capacitance, $\widetilde{C}_d = C_d/C_D$, versus the normalized potential drop across that layer, $\overline{V}_d = \beta e V_d$, for a fixed packing fraction of ions $\nu = 10^{-4}$ and for several values of the parameter $\Gamma = \gamma/(\beta e \lambda_D)$ that controls the inverse saturation electric field: $\Gamma = 1$ [solid (blue) lines], $\Gamma = 0.2$ [dotted (green) lines], $\Gamma = 0.1$ [dash-dotted (red) lines], and $\Gamma = 0.05$ [dashed (light blue) lines].

find $\Gamma \approx 0.7\sqrt{c}$ showing that the typical range of values for this parameter does not exceed $\Gamma \sim 1$ for salt concentrations $c \lesssim 1$ M.

In Fig. 5.2 we plot the normalized DL capacitance versus normalized potential drop with fixed $\nu = 10^{-4}$ and for several values of the parameter Γ. The resulting curves are qualitatively similar to those shown in Fig. 9(b) of Ref. [3] for the same set of parameters, but with the double peaked structures that are seen at the intermediate values of Γ appearing more pronounced in our modeling. One notices the U-shaped behavior of the capacitance in Fig. 5.2 at small potentials, which stems from the GC capacitance in the PB limit of the weak electric field and negligible steric effects, where $\widetilde{C}_d \approx \cosh\left(\overline{V}_d/2\right)$. However, with increasing the parameter Γ the capacitance passes through one or two peaks at potentials in the range $1 \lesssim \overline{V}_d \lesssim 10$, attaining maximum values of the capacitance that

appear to be significantly reduced in our case when compared to those seen in Fig. 9(b) of Ref. [3] The double peak structures seen in the DL capacitance are a consequence of the competition between the ion crowding effect and dielectric saturation effect, which both cause a decrease in the capacitance with increasing potential, albeit at different rates [3]. It is remarkable in our Fig. 5.2 that at high enough potentials, say $\overline{V}_d \gtrsim 15$ or so, the DL capacitance approaches the previously deduced asymptotic form $\widetilde{C}_{GBBF} \sim n_w/\sqrt{2\epsilon_b \nu \overline{V}_d}$, showing that the water dielectric constant is fully saturated for finite-size ions regardless of their concentration. This surprisingly universal behavior of the DL capacitance at high potentials is further accentuated in its non-normalized form $C_{GBBF} \sim n_w \sqrt{z^2 e c_{\max}/\left(8\pi V_d\right)}$, which is also independent of temperature.

5.2.2 Total capacitance

We further analyze the total capacitance for electrolytically gated graphene in the presence of both the steric effect (controlled by the parameter $\nu = 2a^3 c_0$, which for $a = 0.71$ nm amounts to $\nu \approx 0.43\, c$) and dielectric saturation via Booth formula (controlled by the parameter $\Gamma \approx 0.7\sqrt{c}$). We adopt here a different normalization of the capacitances by using a prefactor from Eq. (5.13), given by

$$C_0 = (2/\pi) e^2 / \left[\beta \left(\hbar v_F\right)^2\right], \tag{5.32}$$

which takes the value $C_0 \approx 0.6\ \mu\mathrm{F/cm}^2$ at room temperature. Hence, the total normalized capacitance is given by

$$\overline{C} \equiv C/C_0 = \overline{C}_q \overline{C}_d / \left(\overline{C}_q + \overline{C}_d\right), \tag{5.33}$$

where $\overline{C}_d = C_d/C_0$ and $\overline{C}_q = C_q/C_0$. Notice that the thus normalized QC of graphene,

$$\overline{C}_q = 2 \ln\left[2 \cosh\left(\overline{V}_q/2\right)\right], \tag{5.34}$$

increases linearly with normalized potential at unit slope, according to $\overline{C}_q = \overline{V}_q$, when $\overline{V}_q \gg 1$. In Fig. 5.3 we show several cases of the total normalized capacitance $\overline{C}$ versus normalized total applied potential $\overline{V}_a$ for two salt concentrations, (a) $c = 1\ \mu$M and (b) $c = 1$ M. In addition to the case where both the dielectric saturation via Booth formula (labeled B) and the steric effect (labeled S) are included, we also show in Fig. 5.3 the cases where the dielectric saturation is "turned off" by setting $\Gamma \to 0$ (labeled NB) and/or where the steric effect is "turned off" by setting $\nu \to 0$ (labeled NS). In all four combinations of the models, labeled as B+S, B+NS, NB+S, and NB+NS (the latter being equivalent to the PB theory of DL), we have used the expression for QC from Eq. (5.13) that is based on the linear approximation for the DOS of graphene's π electron bands (results shown with thick lines), whereas in the cases B+S and NB+NS we also used a full nonlinear expression for the DOS, as given in Eq. (2.34)[1] (results shown with thin lines).

One may see in Fig. 5.3 that the dielectric saturation and steric effects do not play significant roles in the total capacitance for potentials $\overline{V}_a \lesssim 40$, i.e. , when $V_a \lesssim 1$ V, and

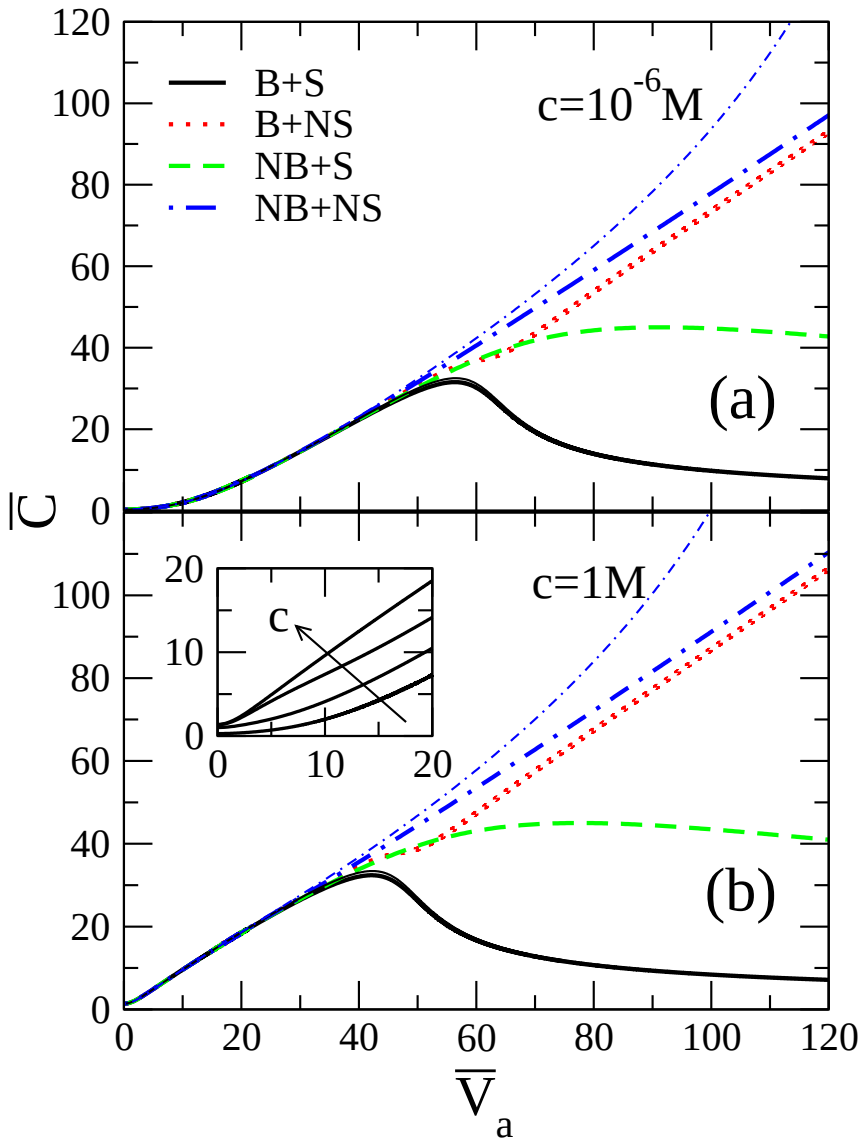

Figure 5.3: The total normalized capacitance $\overline{C} = C/C_0$, where $C_0 = (2/\pi)e^2/\left[\beta\left(\hbar v_F\right)^2\right] \approx 0.6\ \mu\text{F/cm}^2$ comes from the quantum capacitance of graphene, versus normalized total applied potential $\overline{V}_a = \beta e V_a$ for two salt concentrations: (a) $c = 10^{-6}$ and (b) $c = 1$ M (mole/liters). The four cases shown with thick lines are calculated using linear approximation for the density of states for graphene's π electron bands, and are labeled B (NB) when they include (exclude) dielectric saturation via Booth model and are labeled S (NS) when they include (exclude) steric effect. The cases B+S and NB+NS that are shown with thin lines are calculated using a nonlinear expression for the density of states, as given in Eq. (2.34)[1]. The inset shows a blow-up of the total capacitance in the case NB+NS for four concentrations: $c = 10^{-6}, 10^{-4}, 10^{-2}$ and 1 M with an arrow pointing in the direction of increasing values of c.

hence the total potential may be determined by using the simple PB theory for DL, in which $\overline{C}_d \approx \Delta \cosh\left(\overline{V}_d/2\right)$ where

$$\Delta \equiv \frac{C_D}{C_0} = \frac{\left(\hbar v_F \beta\right)^2}{8\lambda_B \lambda_D}, \tag{5.35}$$

with $\lambda_B = \beta e^2/\epsilon_b \approx 0.7$ nm being the Bjerrum length in the bulk water at zero electric field [16]. Noting that this parameter takes the value $\Delta \approx 374\sqrt{c}$, it follows that the total capacitance will be dominated by the graphene QC for salt concentrations $c \gtrsim 7$ μM and not too large potentials. Moreover, we find that using the expression for QC from Eq. (5.13), which is based on the linear approximation for the DOS of graphene, works well in the range of potentials $\overline{V}_a \lesssim 40$.

Thus, one may conclude that, for the applied potentials such that $V_a = V_q + V_d \lesssim 1$ V, it suffices to analyze the total capacitance of a solution gated graphene by using the expression in Eq. (5.31) with the graphene QC given in Eq. (5.13) and the DL capacitance given by $C_d = C_D \cosh\left(\beta z e V_d/2\right)$, subject to the charge neutrality constraint $\sigma_g(V_q) + \sigma_d(V_d) = 0$, with the graphene charge density given in Eq. (5.12) and the diffuse charge density given by [16]

$$\sigma_d\left(V_d\right) = \sqrt{2\epsilon_b c_0/(\pi\beta)}\sinh\left(\beta z e V_d/2\right). \tag{5.36}$$

To analyze the role of salt concentration, we show in the inset to Fig. 5.3 a blow-up of the results for the total capacitance in the case NB+NS for four concentrations: $c = 10^{-6}, 10^{-4}, 10^{-2}$ and 1 M with an arrow pointing in the direction of increasing values of c. One sees in the inset that, even though the QC of graphene dominates at low applied potentials, the total capacitance is not entirely insensitive to the salt concentration at such potentials. This is also evidenced by the shift in the peak position of the B+S curves in the range of potentials $40 \lesssim \overline{V}_a \lesssim 60$ seen in the main panels of Fig. 5.3 as the salt concentration jumps from $c = 10^{-6}$ to $c = 1$ M. However, given the large range of variation of c in Fig. 5.3, it is clear that the mere change in shape of the total capacitance curves is not particularly sensitive to variations in the salt concentration.

Looking at the higher range of the potentials in Fig. 5.3, $\overline{V}_a \gtrsim 40$, i.e. , $V_a \gtrsim 1$ V, one notices that the total capacitance becomes quite dependent on the model combination used to calculate it. First, the NB+NS case increases linearly with increasing potential, thus reflecting the continued dominance of the graphene QC that scales as $\overline{C}_q = \overline{V}_q$ within the linear approximation for DOS, whereas the DL capacitance is given by the PB result $\overline{C}_d \approx \Delta \cosh\left(\overline{V}_d/2\right)$. It is noteworthy that, in the panel (b) of Fig. 5.3, the total capacitance in the NB+NS case is given by $\overline{C} \approx \overline{V}_a$ because the DL capacitance is so large at high salt concentrations that $\overline{C} \approx \overline{C}_q$, whereas practically all of the applied potential goes to graphene, so that $\overline{V}_a \approx \overline{V}_q$. One further sees that adding the nonlinearity in the DOS for the case NB+NS slightly increases the total capacitance at potentials $\overline{V}_a \gtrsim 40$, as expected, while adding the dielectric saturation via the Booth model in the case B+NS only sets off the capacitance to a slightly lower value.

The case NB+S in Fig. 5.3 reproduces a broad maximum in the total capacitance due to the steric effect acting alone, which was seen in Ref. [29] to be only slightly affected by the nonlinearity in the DOS. Finally, in the case B+S, when both the dielectric saturation and steric effects operate, one notices a strong decrease in the total capacitance that occurs after the potential increases past the peak seen for $\overline{V}_a$ somewhere between 40 and 60. Noticing that the thin and thick solid lines used for the B+S case in Fig. 5.3 are almost indistinguishable, one may conclude that the total capacitance is independent from the nonlinearity in the DOS of graphene when both the dielectric saturation and steric effects operate. This is related to the effects seen in Fig. 5.2, where the DL capacitance essentially follows the universal asymptotic form $C_{GBBF} \sim n\sqrt{z^2 e c_{\max}/\left(8\pi V_d\right)}$ at sufficiently large potential $\overline{V}_d$, so that it becomes small enough to dominate the total capacitance at a large applied potential $\overline{V}_a$. However, it is remarkable that any signature of the double peaked structures seen in Fig. 5.2 for the DL capacitance at the DL potentials $1 \lesssim \overline{V}_d \lesssim 10$ is completely lost in the total capacitance for the case B+S in Fig. 5.3, presumably due to the dominance of graphene's QC at the corresponding applied potentials.

Finally, it is of substantial interest, both for modeling and applications, to analyze the distribution of the total potential $\overline{V}_a$ applied to a reference electrode in the bulk of electrolyte between the potential drop $\overline{V}_d$ across the DL, and the quantum potential $\overline{V}_q$ in graphene that determines its doping charge density according to Eq. (5.12). Thus, we show in Fig. 5.4 the dependence of $\overline{V}_q$ on $\overline{V}_a$ for all four model combinations using the linear approximation for the DOS of graphene's π electron bands that were shown by the thick lines in Fig. 5.3. (We have also evaluated the cases B+S and NB+NS with the nonlinear DOS, but found practically no noticeable effects over the entire range of the potentials, so we left out the corresponding curves from Fig. 5.4 for the sake of its clarity.) One notices in Fig. 5.4 that, in the absence of steric effects, almost all of the applied potential goes to graphene and may be effectively used for its doping. This is particularly true at high salt concentrations, as seen in the panel (b) of Fig. 5.4 where $\overline{V}_q \approx \overline{V}_a$, which may be rationalized by the fact that the DL capacitance remains so high due to small effective thickness of the DL for point ions, even in the presence of dielectric saturation, that the total capacitance remains dominated by the QC of graphene for all potentials. On the other hand, with the inclusion of steric effects, there is a gradual increase of the fraction of the potential that goes across the DL and, in the case of dielectric saturation, the split between the quantum potential and the drop across the DL is approximately equal for the highest applied potential shown in Fig. 5.4. Thus, since $\overline{V}_q$ does not exceed the value 60 in the case B+S in Fig. 5.4, it becomes obvious why the total capacitance in Fig. 5.3 is practically independent from nonlinear effects in the DOS for the same case.

We conclude this section by analyzing the regimes of graphene doping through an aqueous electrolyte where the dielectric saturation may become important. In the absence of specific adsorption and without charged impurities, charge neutrality implies that $\sigma_d = -\sigma_g$. Then, in the absence of a Stern layer, one may use Eq. (7.55) to find the electric field and hence evaluate the effective dielectric constant of water at the surface of graphene, ϵ_{surf}, for any given charge carrier density in graphene. We find that for densities under about

10^{13} cm^{-2} (corresponding to $\overline{V}_q \lesssim 15$) one may safely use the zero-field value for the water surface dielectric constant, $\epsilon_{\rm surf} \approx 80$, but a rapid change occurs at higher charge carrier densities where, e.g., for the density of 10^{14} cm^{-2} (corresponding to $\overline{V}_q \approx 47$) we find $\epsilon_{\rm surf} \approx 54$. This emergence of the dielectric saturation effect correlates with the changes in the curves in Figs. 5.3 and 5.4 that show the cases including the Booth formula, which are seen to generally occur in the range of applied potentials $40 \lesssim \overline{V}_a \lesssim 60$.

5.3 Concluding remarks

We have described theoretically the capacitance of an electrolytically top-gated, single layer graphene of large area as a function of the applied gate potential and the changing salt concentration in the presence of dielectric saturation of water and the steric effect due to finite ion size in a nearby aqueous solution. Those effects were described analytically by the well established models due to Booth [46] (for dielectric saturation) and Bikerman [40] and Freise [41] (for the steric effect), respectively.

We have first analyzed the dielectric saturation and steric effects on the capacitance of diffuse layer of ions in the electrolyte, in close analogy to the analysis presented in Ref. [3]. We confirmed the emergence of doubly peaked structures in the capacitance as a function of the potential drop across the diffuse layer at intermediate potentials, as well as the dominance of a drastically reduced universal capacitance at high potentials, which operates in the regime of a full dielectric saturation and the complete ion crowding near an ideal metallic electrode [36].

When graphene is used as an electrode in an aqueous electrolyte, we have confirmed that the total capacitance is dominated by the quantum capacitance of graphene at low gating potentials ($\lesssim 1$ V), similar to the observations made when graphite [20] or the conductive diamond [21, 22] were used as electrodes. Moreover, we have shown that for the range of gating potentials $\lesssim 1$ V, which is most interesting for graphene-based devices, it suffices to use a linear approximation for the density of states for graphene's π electron bands, whereas the capacitance of the electric double layer in the electrolyte may be adequately described within the standard Poisson-Boltzmann theory [16]. We have also shown that the effects of changing the salt concentration are relatively weak, as well as that the most of the potential applied through the electrolyte goes to doping the graphene.

However, at the gating potentials $\gtrsim 1$ V, the effects coming from: the nonlinearity in graphene's density of states, the dielectric saturation of water, and the finite ion size all become important for the total capacitance in a broad range of the salt concentrations. We have found that, while the nonlinear density effect is not particularly prominent at high potentials, the total capacitance becomes dominated by the capacitance of the diffuse layer, which exhibits a dramatic decrease with increasing gating potential due to interplay of the dielectric saturation and steric effects. As a consequence, a sizeable fraction of the applied gate potential goes across the diffuse layer at high gate potentials. Nevertheless, we

have found that the intricacies of doubly peaked structures in the diffuse layer capacitance disappear in the total capacitance, presumably due to the all important role played by graphene's quantum capacitance, even at high gating potentials.

All the above findings may be of interest for applications of the solution-gated graphene devices, where high doping densities may be desired, e.g., for graphene based surface plasmon resonance interfaces [87]. However, high gating potentials will inevitably cause specific adsorption of ions at the graphene-solution interface, which can be efficiently used for ion and pH sensing applications of graphene, in both the transistor and capacitor mode [19]. Our future effort will be devoted to amending the present model of graphene capacitance in the presence of specific adsorption in an electrolyte.

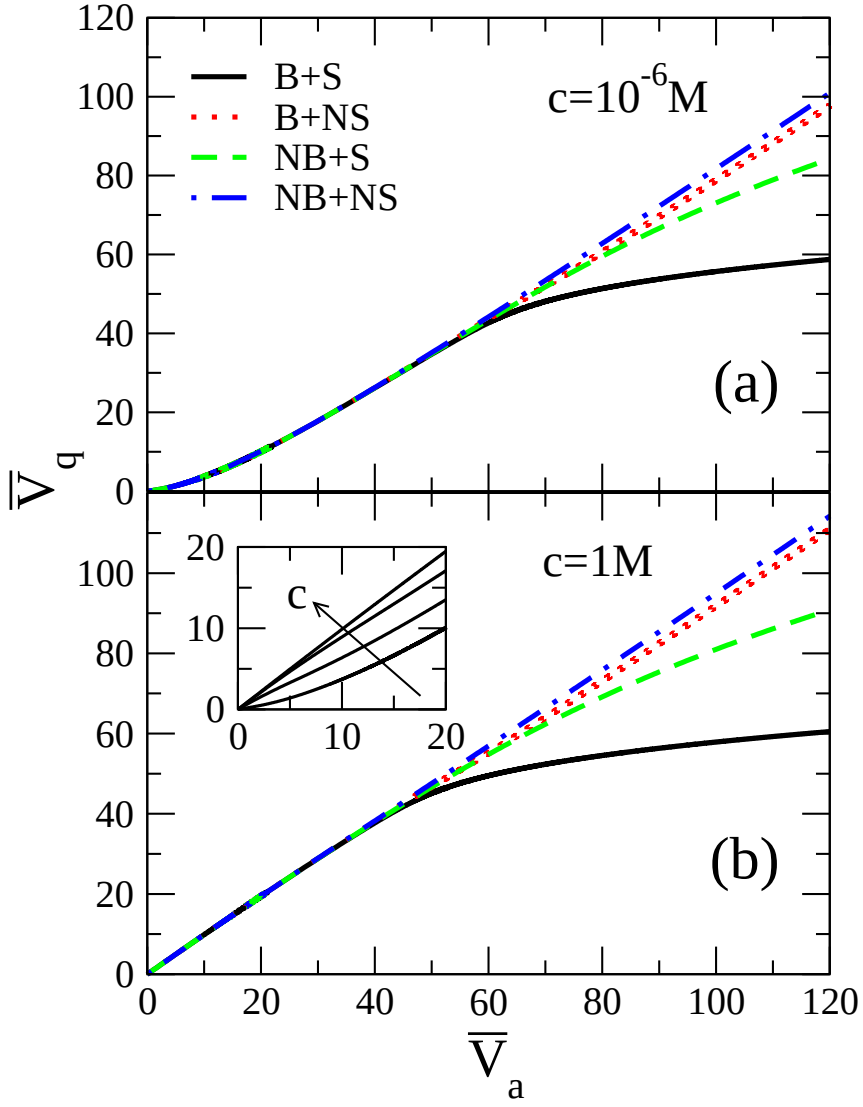

Figure 5.4: The normalized quantum potential $\overline{V}_q = \beta e V_q$ on graphene versus normalized total applied potential $\overline{V}_a = \beta e V_a$ for two salt concentrations: (a) $c = 10^{-6}$ and (b) $c = 1$ M (mole/liters). The four cases shown with thick lines are calculated using linear approximation for the density of states for graphene's π electron bands, and are labeled B (NB) when they include (exclude) dielectric saturation via Booth model and are labeled S (NS) when they include (exclude) steric effect. The inset shows a blow-up of the quantum potential in the case NB+NS for four concentrations: $c = 10^{-6}, 10^{-4}, 10^{-2}$ and 1 M with an arrow pointing in the direction of increasing values of c.

Chapter 6

Ionic screening of charged impurities in electrolytically gated graphene: Debye-Hückel approximation

In this chapter, we present a model for dual-gated, single-layer graphene, with a back gate separated by a layer of oxide, and the top gate potential applied through a thick layer of liquid electrolyte that contains mobile ions in a diffuse layer, described in the Debye-Hückel approximation, which is separated from graphene by a charge-free Stern layer. After deriving a non-linear equation for the average charge carrier density in graphene in terms of the gate potentials, we use the Green's function of the Poisson equation to express the fluctuating part of the electrostatic potential in the plane of graphene in terms of the distribution function for fixed charged impurities in the oxide. By using both the Thomas-Fermi and the random phase approximations of graphene's response at non-zero temperature, we show that the presence of mobile ions in the electrolyte significantly increases graphene's screening ability of the in-plane potential for a single impurity, accentuates Friedel oscillations in that potential, and gives rise to a linear plasmon dispersion in doped graphene at long wavelengths. In the case of multiple charged impurities in the oxide, the increasing ion concentration in the electrolyte causes a reduction in the auto-correlation function of the fluctuating in-plane potential when the impurities are uncorrelated. However, when the impurities are correlated, the relative effect of the increased ion concentration in the electrolyte is drastically reduced, while the auto-correlation function in this case takes negative values in a range of inter-impurity distances.

6.1 Theory

As indicated in Fig. 6.1, we use a cartesian coordinate system with coordinates $\mathbf{R} \equiv \{\mathbf{r}, z\}$, where $\mathbf{r} \equiv \{x, y\}$, and we assume that graphene is placed in the plane $z = 0$, while oxide occupies the region I_1 defined by $-t \leq z \leq 0$ and is characterized by a relative dielectric

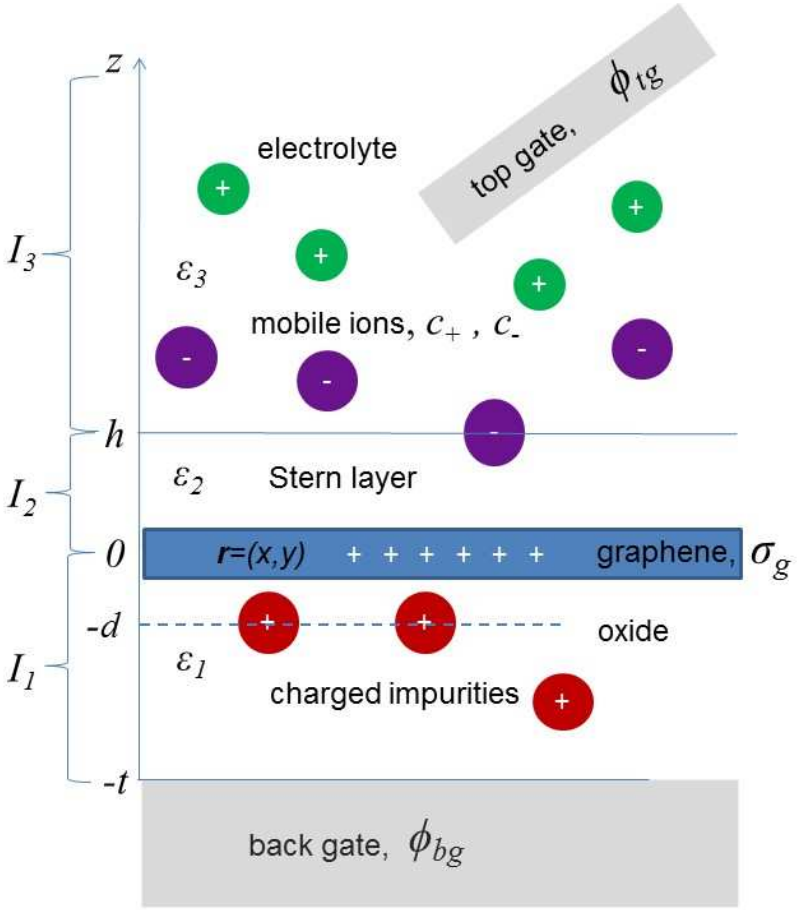

Figure 6.1: A diagram showing the configuration of the system studied, with the region I_1, $-t<z<0$, representing an oxide layer with dielectric constant ϵ_1 that contains trapped charged impurities, region I_2, $0<z<h$, representing a charge-free Stern layer with dielectric constant ϵ_2, and the region I_3, $z>h$, representing a diffuse layer, which contains mobile ions in a semi-infinite electrolyte with the solvent dielectric constant ϵ_3. $\phi_{\rm bg}$ and $\phi_{\rm tg}$ are the electrostatic potentials at the back gate, $z=-t$, and at the top gate in the bulk electrolyte, $z\to\infty$, respectively, whereas a single layer of graphene occupies the plane $z=0$. Fluctuations in the electrostatic potential in the plane of graphene, $\phi_0(\mathbf{r})$, are evaluated for a specific model of the spatial distribution of trapped charges, which restricts their vertical positions to lie in the plane $z=-d$ under the graphene but allows for the correlation among the positions of those charges in the directions parallel to the graphene plane.

constant $\epsilon_1\equiv\epsilon_{\rm ox}$. The Stern layer (SL) is assumed to occupy the region I_2 defined by $0\le z\le h$ and is characterized by a relative dielectric constant ϵ_2, whereas the semi-infinite diffuse layer (DL) defined by I_3 fills the region $z\ge h$, which is characterized by a relative dielectric constant of the solvent $\epsilon_3\ge\epsilon_2$. Furthermore, we assume that charged impurities in region I_1 are described by a volume charge density $\rho_{\rm imp}(\mathbf{R})$ and we note that

the SL is free of charge by definition [16]. In this chapter we describe the DL within the DH approximation for a symmetric binary electrolyte containing mono-valent ions with $Z_i = 1$ and having an equilibrium number density of c in the bulk electrolyte.

Assuming that the electrostatic potential $\Phi(\mathbf{R})$ satisfies the boundary conditions

$$\Phi(\mathbf{R})|_{z=-t} = \phi_{\rm bg}, \tag{6.1}$$

where $\phi_{\rm bg}$ is the surface potential at the back gate, which is taken to be independent of $\mathbf{r}$, and

$$\Phi(\mathbf{R})|_{z\to\infty} = \phi_{\rm tg}, \tag{6.2}$$

where $\phi_{\rm tg}$ is the potential in the bulk of electrolyte that is related to the top gate potential at a reference electrode in Fig. (6.1) [16], we wish to determine the electrostatic potential in the plane of graphene,

$$\phi_0(\mathbf{r}) \equiv \Phi(\mathbf{R})|_{z=0}\,, \tag{6.3}$$

as a function of the lateral coordinates $\mathbf{r}$ for any given distribution of the impurity charges $\rho_{\rm imp}(\mathbf{R})$.

We proceed by defining the full potential in a piece-wise manner by $\Phi(\mathbf{R}) = \Phi_j(\mathbf{R})$ for the z coordinate in the region I_j, $j = 1$, 2, or 3, satisfying the Poisson equation in the corresponding region,

$$\epsilon_j \nabla^2_{\mathbf{R}} \Phi_j(\mathbf{R}) = -4\pi\rho_j(\mathbf{R}), \tag{6.4}$$

where $\rho_1(\mathbf{R}) = \rho_{\rm imp}(\mathbf{R})$, $\rho_2(\mathbf{R}) = 0$, and $\rho_3(\mathbf{R}) = \rho_{\rm ion}(\mathbf{R})$, with the density of mobile ions given in the DH approximation by

$$\rho_{\rm ion}(\mathbf{R}) = -2\beta Z_i^2 e^2 c\,[\Phi_3(\mathbf{R}) - \phi_{\rm tg}]\,. \tag{6.5}$$

Invoking the continuity of the potential, we have two matching conditions, one at the plane of graphene,

$$\Phi_1(\mathbf{R})|_{z=0} = \Phi_2(\mathbf{R})|_{z=0} \equiv \phi_0(\mathbf{r}), \tag{6.6}$$

and the other at the boundary between the DL and SL (that is, at the outer Helmholtz plane [16]),

$$\Phi_2(\mathbf{R})|_{z=h} = \Phi_3(\mathbf{R})|_{z=h}\,. \tag{6.7}$$

Regarding the jump conditions for the potential, in the zero-thickness approximation for a single-layer graphene, we have at the plane of graphene

$$-\epsilon_2 \left.\frac{\partial\Phi_2(\mathbf{R})}{\partial z}\right|_{z=0} + \epsilon_1 \left.\frac{\partial\Phi_1(\mathbf{R})}{\partial z}\right|_{z=0} = 4\pi\,\sigma_g[\phi_0(\mathbf{r})], \tag{6.8}$$

where $\sigma_g[\phi_0(\mathbf{r})]$ is the surface charge density of graphene, which is generally a functional of the in-plane potential $\phi_0(\mathbf{r})$, whereas absence of the surface charge at the boundary between the DL and SL gives

$$\epsilon_2 \left.\frac{\partial\Phi_2(\mathbf{R})}{\partial z}\right|_{z=h} = \epsilon_3 \left.\frac{\partial\Phi_3(\mathbf{R})}{\partial z}\right|_{z=h}. \tag{6.9}$$

6.1.1 Equations for the averaged quantities

We define the surface averages of the density of charged impurities and the electrostatic potential components, respectively, as

$$\bar{\rho}_{\rm imp}(z) = \frac{1}{\mathcal{A}} \int d^2\mathbf{r}\, \rho_{\rm imp}(\mathbf{R}), \tag{6.10}$$

$$\bar{\Phi}_j(z) = \frac{1}{\mathcal{A}} \int d^2\mathbf{r}\, \Phi_j(\mathbf{R}), \tag{6.11}$$

for j =1, 2, and 3, where $\mathcal{A}$ is the macroscopic area of the graphene channel. This allows us to separate out the z dependent averages of those quantities from their respective fluctuating parts,

$$\rho_{\rm imp}(\mathbf{R}) = \bar{\rho}_{\rm imp}(z) + \delta\rho_{\rm imp}(\mathbf{R}), \tag{6.12}$$

$$\Phi_j(\mathbf{R}) = \bar{\Phi}_j(z) + \delta\Phi_j(\mathbf{R}), \tag{6.13}$$

The in-plane potential is accordingly decomposed into

$$\phi_0(\mathbf{r}) = \bar{\phi}_0 + \delta\phi_0(\mathbf{r}), \tag{6.14}$$

with the surface average of that potential defined by the analogue of Eq. (6.10), that is,

$$\bar{\phi}_0 = \frac{1}{\mathcal{A}} \int d^2\mathbf{r}\, \phi_0(\mathbf{r}), \tag{6.15}$$

and with $\delta\phi_0(\mathbf{r})$ as its fluctuating part. While the decompositions in Eqs. (6.12) and (6.13) do not assume linearization of the density of charged impurities or of the potential components, we note that further progress is made by invoking a linear response approximation for the total surface charge density on graphene,

$$\sigma_g[\phi_0(\mathbf{r})] \approx \bar{\sigma}_g + \delta\sigma_g[\delta\phi_0(\mathbf{r})]\,, \tag{6.16}$$

where $\bar{\sigma}_g$ is an average charge density on graphene that is determined by the average potential $\bar{\phi}_0$, whereas $\delta\sigma_g$ is a linear functional of the fluctuating part of the in-plane potential, $\delta\phi_0(\mathbf{r})$.

In passing, we describe how $\bar{\sigma}_g$ may be evaluated from the definition of the equilibrium number density of charge carriers in graphene, $n(\mu)$, given in Eq. (2.38), where we define the chemical potential of graphene as $\mu = \varepsilon_{\rm F} - \varepsilon_{\rm D}$, with $\varepsilon_{\rm F}$ being the Fermi energy relative to the local vacuum level and $\varepsilon_{\rm D}$ the Dirac energy in graphene. By using the low-energy approximation for the density of states for graphene's π-electron bands, $\mathcal{D}(\varepsilon) \approx \mathcal{D}_L(\varepsilon)$ in Eq. (2.38), and letting $\varepsilon_{\rm D} = -e\bar{\phi}_0$ while keeping $\varepsilon_{\rm F}$ fixed, we obtain the average charge density of graphene as $\bar{\sigma}_g(\bar{\phi}_0) = -en(\varepsilon_{\rm F} + e\bar{\phi}_0)$, with the equilibrium surface density of charge carriers $n(\mu)$ given in Eq. (2.39). Proceeding along this line of reasoning, a Thomas-Fermi (TF) approximation for the response of graphene may be readily derived

by expressing the second term in Eq. (6.16) as $\delta\sigma_g \approx -C_{\rm q}\delta\phi_0(\mathbf{r})$, where the quantum capacitance of graphene per unit area is defined from Eq. (2.39) as [24]

$$C_{\rm q} = -\frac{\partial\bar{\sigma}_g}{\partial\bar{\phi}_0} = \frac{q_{\rm TF}}{2\pi}, \tag{6.17}$$

where q_{TF} is the inverse TF screening length in free graphene, defined in Eq. (3.5) with $\mu = \varepsilon_{\rm F} + e\bar{\phi}_0$ [29]. In the subsequent sections, we find it useful to define a related quantity for macroscopically neutral graphene, where $\varepsilon_{\rm F} + e\bar{\phi}_0 = 0$, by $q_0 = 8e^2 \ln 2/\left[\beta\left(\hbar v_{\rm F}\right)^2\right] \approx 0.48\ \mathrm{nm}^{-1}$.

We may now solve the 1D Poisson equations for the z dependent average potential, given in the three regions by

$$\bar{\Phi}_1''(z) = -\frac{4\pi}{\epsilon_1}\bar{\rho}_{\rm imp}(z), \tag{6.18}$$

$$\bar{\Phi}_2''(z) = 0, \tag{6.19}$$

$$\bar{\Phi}_3''(z) - \kappa^2\bar{\Phi}_3(z) = \kappa^2\phi_{\rm tg}. \tag{6.20}$$

The solutions of these equations that satisfy the non-homogeneous boundary conditions in Eqs. (7.4) and (7.5) may readily be written as

$$\bar{\Phi}_1(z) = -\frac{4\pi}{\epsilon_1}\int_{-t}^{z} dz'\ (z-z')\,\bar{\rho}_{\rm imp}(z') + A(z+t) + \phi_{\rm bg}, \tag{6.21}$$

$$\bar{\Phi}_2(z) = Bz + C, \tag{6.22}$$

$$\bar{\Phi}_3(z) = D\mathrm{e}^{-\kappa(z-h)} + \phi_{\rm tg}, \tag{6.23}$$

where the coefficients A, B, C and D are determined by imposing the matching conditions in Eqs. (6.6)-(6.9), with the right-hand sides in Eqs. (6.6) and (6.8) being $\bar{\phi}_0$ and $\bar{\sigma}_g(\bar{\phi}_0)$, respectively. As a result, one arrives at a consistency equation for the average potential in the plane of graphene $\bar{\phi}_0$,

$$\left(C_{\rm ox} + C_{\rm dl}\right)\bar{\phi}_0 = C_{\rm ox}\phi_{\rm bg} + C_{\rm dl}\phi_{\rm tg} + \bar{\sigma}_g(\bar{\phi}_0) + \bar{\sigma}_{\rm imp}, \tag{6.24}$$

where we have defined the capacitance per unit area of the oxide by

$$C_{\rm ox} = \frac{\epsilon_1}{4\pi t}, \tag{6.25}$$

whereas the capacitance per unit area of the electrostatic double layer (EDL) is given by a series connection of the capacitances of the SL and DL,

$$C_{\rm dl} = \left(C_{\rm S}^{-1} + C_{\rm D}^{-1}\right)^{-1}, \tag{6.26}$$

with

$$C_{\rm S} = \frac{\epsilon_2}{4\pi h}, \tag{6.27}$$

and

$$C_{\rm D} = \frac{\epsilon_3 \kappa}{4\pi}, \tag{6.28}$$

with the inverse Debye screening length κ defined in Eq. (4.7). In Eq. (6.24), we have defined the effective surface charge density of charged impurities by

$$\bar{\sigma}_{\rm imp} = \int_{-t}^{0} dz \, \left(1 + \frac{z}{t}\right) \bar{\rho}_{\rm imp}(z). \tag{6.29}$$

It is important to note that Eq. (6.24) may be used to determine the average charge density in graphene, $\bar{\sigma}_g = -e\bar{n}$, for any combination of the back-gate and the top-gate (that is, reference electrode) potentials relative to graphene's Fermi level, $V_{\rm bg}$ and $V_{\rm tg}$, respectively. Then, the screening properties of graphene may be assessed by first evaluating its chemical potential μ from the relation $\bar{n} = n(\mu)$ via Eq. (2.39), and then plugging the thus obtained μ into the expression for the polarizability function of graphene $\chi(q)$ given in Eq. (B.24).

We note that Eq. (6.24) relates only the electrostatic components of the potential drops across the oxide and the EDL to the average position of the Dirac point in graphene relative to the local vacuum level. In order to determine $\bar{\sigma}_g$ in practice one must modify Eq. (6.24) by taking into account the relative potential offsets of all the media involved. Defining the doping potential in graphene by $V_q \equiv \mu/e = (\varepsilon_{\rm F} - \bar{\varepsilon}_{\rm D})/e = \varepsilon_{\rm F}/e + \bar{\phi}_0$, one may use Eq. (5.12) to define the function $\bar{\sigma}_g(V_q)$, which turns Eq. (6.24) into a nonlinear equation for V_q,

$$(C_{\rm ox} + C_{\rm dl})\, V_q = C_{\rm ox}\left[V_{\rm bg} - (w_{\rm bo} - w_{\rm go})\right] + C_{\rm dl}\left[V_{\rm tg} - (w_{\rm te} - w_{\rm ge})\right] + \bar{\sigma}_g(V_q) + \bar{\sigma}_{\rm imp}, \tag{6.30}$$

where $w_{\rm bo}$, $w_{\rm go}$, $w_{\rm te}$, and $w_{\rm ge}$ are the potential offsets for the back-gate relative to the oxide, graphene relative to the oxide, top gate (reference electrode) relative to the electrolyte, and graphene relative to the electrolyte, respectively[88]. We note that, since the effect of mobile ions is contained in $C_{\rm D}$ and hence in $C_{\rm dl}$, Eq. (6.30) may be used by setting $V_q = 0$ to analyze the effects of ion concentration c on the gate potentials that correspond to graphene's conductivity minimum, if the relevant potential offsets are known [37, 89, 90].

However, for the sake of a preliminary analysis of the gating of graphene through an electrolyte at the qualitative level, we shall discard those offsets and just assume that they define the so-called potential of zero charge on graphene that is akin to the flat band potential in ordinary semiconductor based transistors. Moreover, since our use of the DH approximation for diffuse layer limits the range of applicability of the linearized PB equation to a low potential drop across that layer, in this chapter we shall simply treat $\bar{n}$ as free parameter.

6.1.2 Linearized model for fluctuating potential

With the linearization of the problem established via Eq. (6.16) we may perform a 2D Fourier transform (FT) of the fluctuating part of the potential $\delta\Phi_j(\mathbf{R}) \equiv \delta\Phi_j(\mathbf{r}, z)$,

$$\widetilde{\Phi}_j(\mathbf{q}, z) = \iint d^2\mathbf{r}\, \mathrm{e}^{-i\mathbf{q}\cdot\mathbf{r}} \delta\Phi_j(\mathbf{r}, z), \tag{6.31}$$

for $j = 1$, 2, and 3, and the fluctuating part of the impurity charge density $\delta\rho_{\mathrm{imp}}(\mathbf{R}) \equiv \delta\rho_{\mathrm{imp}}(\mathbf{r}, z)$,

$$\widetilde{\rho}_{\mathrm{imp}}(\mathbf{q}, z) = \iint d^2\mathbf{r}\, \mathrm{e}^{-i\mathbf{q}\cdot\mathbf{r}} \delta\rho_{\mathrm{imp}}(\mathbf{r}, z), \tag{6.32}$$

and write the Poisson equations in the three regions as

$$\frac{\partial^2\widetilde{\Phi}_1(z)}{\partial z^2} - q^2\widetilde{\Phi}_1(z) = -\frac{4\pi}{\epsilon_1}\widetilde{\rho}_{\mathrm{imp}}(z), \tag{6.33}$$

$$\frac{\partial^2\widetilde{\Phi}_2(z)}{\partial z^2} - q^2\widetilde{\Phi}_2(z) = 0, \tag{6.34}$$

$$\frac{\partial^2\widetilde{\Phi}_3(z)}{\partial z^2} - \left(q^2 + \kappa^2\right)\widetilde{\Phi}_3(z) = 0, \tag{6.35}$$

where we have dropped listing the dependence of all the FTs on $\mathbf{q}$.

Now, the FTs of the fluctuating potential components satisfy homogeneous boundary conditions, that is, $\widetilde{\Phi}_1(-t) = 0$ and $\widetilde{\Phi}_3(\infty) = 0$, whereas the matching conditions in Eqs. (6.7) and (6.9) at $z = h$ remain unchanged. On the other hand, the matching conditions at the plane of graphene, $z = 0$, become

$$\widetilde{\Phi}_1(z)\Big|_{z=0} = \widetilde{\Phi}_2(z)\Big|_{z=0} \equiv \widetilde{\phi}_0, \tag{6.36}$$

where $\widetilde{\phi}_0 \equiv \widetilde{\phi}_0(\mathbf{q})$ is the FT of the fluctuating part of the in-plane potential, $\delta\phi_0(\mathbf{r})$, and

$$-\epsilon_2 \frac{\partial\widetilde{\Phi}_2(z)}{\partial z}\bigg|_{z=0} + \epsilon_1 \frac{\partial\widetilde{\Phi}_1(z)}{\partial z}\bigg|_{z=0} = -4\pi\widetilde{\delta\sigma}_g, \tag{6.37}$$

where $\widetilde{\delta\sigma}_g$ is the FT of the second term in Eq. (6.16), $\delta\sigma_0$, given by

$$\widetilde{\delta\sigma}_g = -e^2\chi(q)\widetilde{\phi}_0(\mathbf{q}) \tag{6.38}$$

within the linear response approach, with $\chi(q)$ being the polarization function of the non-interacting π electrons in graphene. We note that taking the long wavelength limit, $q \to 0$, in the RPA polarization function recovers the TF approximation [38, 62],

$$\chi(q) \to \frac{q_{\mathrm{TF}}}{2\pi e^2}. \tag{6.39}$$

The polarizability of graphene $\chi(q)$ generally depends on its average charge density $\bar{\sigma}_g$, which needs to be determined from Eq. (6.30) in terms of the gate potential(s) before proceeding to the solution of Eqs. (6.33)-(6.35). Accordingly, while the assumption of finite thickness of the oxide is necessary in the application of Eq. (6.30), we may further assume that the screening of fluctuations in the electrostatic potential in the plane of graphene by the back gate may be neglected, allowing us to take the limit of an infinitely thick oxide layer in solving the Eqs. (6.33)-(6.35). Thus, by using Eq. (E.20) (Appendix 8.5) and taking the limit $t \to \infty$ in Eq. (E.31), we may express the FT of the fluctuating part of the in-plane potential as

$$\widetilde{\phi}_0(\mathbf{q}) = \frac{2\pi}{q\epsilon(q)} \int_{-\infty}^{0} dz\, \mathrm{e}^{qz} \widetilde{\rho}_{\mathrm{imp}}(\mathbf{q}, z), \tag{6.40}$$

where we have defined the effective dielectric function of the system in the presence of a graphene layer at $z = 0$ by

$$\epsilon(q) = \epsilon_{\mathrm{bg}}(q) + V_{\mathrm{C}}(q)\chi(q), \tag{6.41}$$

with the background dielectric constant expressed in terms of the Green's function for the surrounding dielectric media without graphene, $\widetilde{G}^{(0)}(q; z, z')$, as

$$\epsilon_{\mathrm{bg}}(q) \equiv \frac{2\pi}{q\,\widetilde{G}^{(0)}(q; 0, 0)} = \frac{1}{2}\left[\epsilon_1 + \epsilon_2 \Gamma(q)\right], \tag{6.42}$$

and $V_{\mathrm{C}}(q) \equiv 2\pi e^2/q$ being the 2DFT of the bare Coulomb interaction in the plane of graphene [62]. Notice that the auxiliary function $\Gamma(q)$ is defined in the Appendix 8.5 in Eq. (E.32).

In passing, we note that the effects of EDL are encompassed in the function $\Gamma(q)$ defined in Eq. (E.32). We may analyze the qualitative effects of a concentration c of mobile ions in the electrolyte on the screening ability of graphene by considering the long wavelength form of the dielectric function in Eq. (6.41) for $q \ll \min\left(q_{\mathrm{TF}}, \kappa, h^{-1}\right)$,

$$\epsilon(q) \approx \frac{\epsilon_1}{2} + \frac{1}{q}\left(q_{\mathrm{TF}} + \frac{1}{2}\frac{\epsilon_3\kappa}{1 + \epsilon_3\kappa h/\epsilon_2}\right) \equiv \frac{\epsilon_1}{2} + \frac{2\pi}{q}\left(C_{\mathrm{q}} + C_{\mathrm{dl}}\right). \tag{6.43}$$

This form of the dielectric functions shows that the TF inverse screening length of graphene is initially increased at low ion concentrations by an amount that is proportional to $\epsilon_3\kappa/2 \propto \sqrt{c}$, which saturates at the value $\epsilon_2/(2h)$ for $\epsilon_3\kappa h/\epsilon_2 \gg 1$ at high enough ion concentrations, when one expects that a condensed layer of counter-ions is formed at the outer Helmholtz plane [16]. We note that the parameters characterizing the SL may be estimated only roughly, with a lower bound for h being a typical radius of the solvated ions in water, $h \gtrsim 0.3$ nm, whereas the reduction of the dielectric constant of water in a SL is sometimes taken to be ten-fold, $\epsilon_3/\epsilon_2 \approx 10$ [3]. By using $\epsilon_3 \approx 80$ for an aqueous solution of monovalent ions at room temperature, we find $\kappa \approx 3.24\,(c/\mathrm{M})^{1/2}$ nm^{-1}, where M stands for mol/litre,

which implies that saturation of the increase in screening by mobile ions sets in at the concentrations $c \sim 0.01$ M or higher.

On the other hand, if we wish to be more specific in estimating the effect of ionic screening at lower concentrations, we may assume $\epsilon_3 \kappa h/\epsilon_2 \ll 1$ in Eq. (6.43) and solve the equation $2q_{\rm TF} = \epsilon_3\kappa$ to obtain a numerical value of ion concentration for which the additional screening by the mobile ions becomes comparable to the screening by the graphene alone. Considering first the macroscopically neutral graphene at 300 K with $q_{\rm TF} = q_0$, we obtain from $2q_0 = \epsilon_3\kappa$ [29]

$$c_0 = \frac{32\,(\ln 2)^2\, e^2}{\pi\epsilon_3\beta^3\,(\hbar v_{\rm F})^4}, \tag{6.44}$$

giving $c_0 \approx 8.28 \times 10^{-6}$ nm$^{-3} \approx 1.37 \times 10^{-5}$ M. For a heavily doped graphene, such that $e|V_q| = |\varepsilon_{\rm F} - \bar{\varepsilon}_{\rm D}| \gg k_B T$, one has $q_{\rm TF} \approx 4e^2 k_{\rm F}/\,(\hbar v_{\rm F})$, where $k_{\rm F} = \sqrt{\pi|\bar{n}|}$ is the Fermi wavenumber, so that the solution of the equation $2q_{\rm TF} = \epsilon_3\kappa$,

$$c_d = \frac{8e^2\bar{n}}{\epsilon_3\beta\,(\hbar v_{\rm F})^2}, \tag{6.45}$$

shows that the ion concentration for which the ionic screening becomes comparable to the screening by doped graphene scales with its charge carriers density $\bar{n}$ as $c_d \approx 1.44 \times 10^{-16}\bar{n}$ cm^2 M.

6.1.3 Statistical properties of the potential

We now use Eq. (6.40) to evaluate the FT, $\widetilde{\varphi}(\mathbf{q})$, of the screened potential in the plane of graphene due to a single impurity represented by a point charge Ze at a depth d underneath graphene,

$$\widetilde{\varphi}(q) = Ze\frac{2\pi}{q\epsilon(q)}\mathrm{e}^{-qd}, \tag{6.46}$$

giving the potential

$$\varphi(r) = Z_i e \int_0^\infty dq\, J_0(qr)\frac{\mathrm{e}^{-qd}}{\epsilon(q)}, \tag{6.47}$$

where J_0 is a Bessel function of order zero.

However, we are primarily interested in statistical properties of the fluctuating part of the in-plane potential, $\delta\phi_0(\mathbf{r})$, given as the inverse FT of the expression in Eq. (6.40) for an ensemble of N point charges $Z_j e$, placed at the points $\mathbf{R}_j = \{\mathbf{r}_j, z_j\}$ with $z_j < 0$, having charge density

$$\rho_{\rm imp}(\mathbf{r}, z) = \sum_{j=1}^{N} Z_j e\,\delta(\mathbf{R} - \mathbf{R}_j)\,. \tag{6.48}$$

In particular, we wish to calculate the auto-correlation function of the fluctuating potential,

$$\mathcal{C}(\mathbf{r},\mathbf{r}') = \langle \delta\phi_0(\mathbf{r})\delta\phi_0(\mathbf{r}')\rangle, \tag{6.49}$$

where $\langle\cdots\rangle$ indicates an ensemble average over all configurations of the charged impurities. Assuming that all the charges are equal, $Z_j = Z$, and that the distribution of their positions in the oxide is translationally invariant in the directions parallel to graphene, we may postulate that the one-particle number density function for this assembly has the form

$$F_1(\mathbf{r},z) = \frac{N}{\mathcal{A}} f_1(z), \tag{6.50}$$

so that $\bar{\rho}_{\rm imp}(z) = Ze\frac{N}{\mathcal{A}} f_1(z)$, where the distribution of the particle positions over the depth, $f_1(z)$, is normalized to one. Similarly, the two-particle number density function may be factored as

$$F_2(\mathbf{r}_1,\mathbf{r}_2;z_1,z_2) = \frac{N(N-1)}{\mathcal{A}^2} f_1(z_1) f_1(z_2) g(\mathbf{r}_2-\mathbf{r}_1;z_1,z_2), \tag{6.51}$$

where $g(\mathbf{r};z_1,z_2)$ is a pair correlation function. As a consequence, the auto-correlation function in Eq. (6.49) is also translationally invariant, $\mathcal{C}(\mathbf{r},\mathbf{r}') \equiv C(\mathbf{r}-\mathbf{r}')$, and is given by

$$\begin{aligned} C(\mathbf{r}) \;=\; & Z^2e^2 n_{\rm imp} \iint d^2\mathbf{q}\, \frac{\mathrm{e}^{i\mathbf{q}\cdot\mathbf{r}}}{q^2\epsilon^2(q)} \left\{ \int\limits_{-\infty}^{0} dz\, \mathrm{e}^{2qz} f_1(z) \right. \\ & \left. + \int\limits_{-\infty}^{0} dz\, \mathrm{e}^{qz} f_1(z) \int\limits_{-\infty}^{0} dz'\, \mathrm{e}^{qz'} f_1(z') \left[I(\mathbf{q};z,z') - 1 \right] \right\}, \end{aligned} \tag{6.52}$$

where $n_{\rm imp} \equiv N/\mathcal{A}$ is the effective surface number density of charged impurities, and $I(\mathbf{q};z,z')$ is a 2D structure factor of the ensemble, defined by

$$I(\mathbf{q};z,z') = 1 + n_{\rm imp} \iint d^2\mathbf{r}\, \mathrm{e}^{i\mathbf{q}\cdot\mathbf{r}} \left[g(\mathbf{r};z,z') - 1 \right]. \tag{6.53}$$

While it is tempting to analyze various models of the depth distribution of trapped charges on the basis of Eqs. (6.52) and (6.53), [91] we limit ourselves to the planar model that has been used so far, [39, 72] where all impurities are assumed to be placed at equal depths in the oxide, $z_j = -d$, so that $f_1(z) = \delta(z+d)$. Moreover, if one also assumes that the distribution of impurities in the plane $z = -d$ is isotropic, so that $g(\mathbf{r};z_1,z_2) = g(r)$, then the auto-correlation function from Eq. (6.52) simplifies to

$$C(r) = 2\pi Z^2 e^2 n_{\rm imp} \int\limits_0^\infty \frac{dq}{q} \frac{\mathrm{e}^{-2qd}}{\epsilon^2(q)} J_0(qr) I(q), \tag{6.54}$$

where

$$I(q) = 1 + 2\pi n_{\rm imp} \int_0^\infty dr\, r J_0(qr)\,[g(r) - 1]\,. \tag{6.55}$$

While it is difficult to model the structure factor, $g(r)$, even in such a simplified 2D model of a translationally invariant and isotropic layer of charged impurities, we consider in this chapter two extreme cases: one corresponding to uncorrelated impurities with $g(r) = 1$ and hence $I(q) = 1$, and the other being a step model with $g(r) = 1$ for $r \geq r_c$ and $g(r) = 0$ otherwise. We note that, by choosing the correlation distance to be $r_c = 1/\sqrt{\pi n_{\rm imp}}$ one mimics a large degree of correlation among the charged impurities, characterized by a zero compressibility, that is, $I(q) \to 0$ when $q \to 0$, in which case Eq. (6.55) gives

$$I(q) = 1 - \frac{2}{qr_c} J_1(qr_c), \tag{6.56}$$

where J_1 is a Bessel function of order one.

6.2 Results

The standard set of parameters used in the calculations in this section takes the oxide to be an SiO_2 with $\epsilon_1 = 3.9$, the Stern layer of thickness $h = 0.3$ nm to have $\epsilon_2 = 8$, and the electrolyte to be an aqueous solution at room temperature with $\epsilon_3 = 80$, having variable concentration c of the mobile ions. Charged impurities are taken to be point charges with equal charges Ze that all lie at a depth $d = 0.2$ nm in SiO_2, whereas the graphene polarizability $\chi(q)$ is evaluated at 300 K for various values of $\bar{n}$. The results for the potential are normalized by Ze/d (≈ 7.2 V for $Z = 1$), those for the auto-correlation function and the variance of the fluctuating in-plane potential are normalized by $(Ze/d)^2$, whereas the radial distance in graphene is normalized by the inverse TF screening length of the neutral graphene at room temperature, $q_0^{-1} \approx 2.1$ nm.

In Fig. 6.2 we show, for a single point charge, the reduced potential $\bar{\varphi} = \varphi\, d/(Ze)$ as a function of the reduced distance in the plane of graphene $\bar{r} = rq_0$, which is evaluated for several ion concentrations in the range $c = 10^{-4}$ M to $c = 1$M by using both the RPA and the TF approximations for graphene's polarizability with several charge carrier densities: $\bar{n} = 10^{11}$, 10^{12}, and 10^{13} cm^{-2}. One notices that the results are weakly dependent on $\bar{n}$ at low charge carrier densities, which is the reason for not showing in Fig. 6.2 the results for the neutral graphene, $\bar{n} = 0$, as being barely distinguishable from those for $\bar{n} = 10^{11}$ cm^{-2}. The main effect of the increasing ion concentration is an increase in the screening length of the potential at a rate that seems to saturate for $c > 0.01$ M due to ion condensation at the boundary between the SL and the DL, as mentioned above. The distinction between the RPA and the TF results also increases with increasing ion concentration. Probably the most surprising result occurs at the highest charge carrier density shown in Fig. 6.2(c),

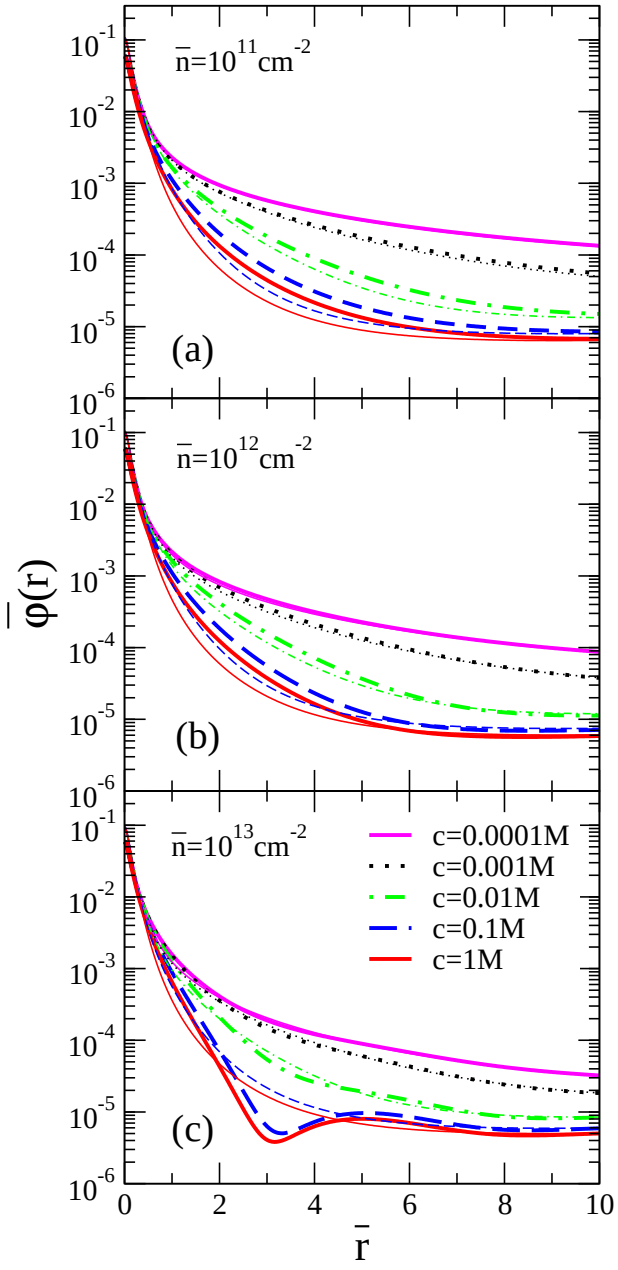

Figure 6.2: Reduced potential in the plane of graphene, $\bar{\varphi} = \varphi\, d/(Ze)$, shown as a function of the reduced distance $\bar{r} = r q_0$, where $q_0^{-1} = 2.1$ nm, due to a single point charge at depth $d = 2$ Å, for several values of the average charge carrier density in graphene: (a) $\bar{n} = 10^{11}$ cm^{-2}, (b) $\bar{n} = 10^{12}$ cm^{-2}, and (c) $\bar{n} = 10^{13}$ cm^{-2}, and for several ion concentrations in the electrolyte: $c = 10^{-4}$ M [solid (pink) lines], $c = 10^{-3}$ M (dotted black lines), $c = 10^{-2}$ M [dash-dotted (green) lines], $c = 10^{-1}$ M [dashed (blue) lines], and $c = 1$ M [solid (red) lines]. Thick lines show the results for the RPA and the thin lines show the results for the TF approximation for graphene's polarizability.

$\bar{n} = 10^{13}$ cm^{-2}, where the potential from the RPA shows Friedel oscillations [1, 39] with amplitudes that seem to increase with respect to the TF results when the ion concentration in electrolyte c increases. Given that those oscillations occur due to a singularity at the wavenumber $q = 2k_{\rm F} = 2\sqrt{\pi\bar{n}}$ in the RPA polarizability of graphene at zero temperature, it appears that the quantum effects in graphene's screening ability are accentuated by the increased ion concentration, even at non-zero temperatures [62]. Moreover, since Friedel oscillations give rise to minima in the in-plane potential at the distances $r \approx 6.6$ - 6.9 nm for the highest charge carrier density shown in Fig. 6.2(c), $\bar{n} = 10^{13}$ cm^{-2}, and for ion concentrations $c \gtrsim 0.01$ M, it is tempting to speculate whether those minima could play a role in ordering the structure of ions in the condensed layer near heavily doped graphene.

In Fig. 6.3 we show the reduced auto-correlation function, $\bar{C}(\bar{r}) = C(\bar{r})\,[d/(Ze)]^2$ as a function of the reduced distance in the plane of graphene $\bar{r} = rq_0$ for an ensemble of point charges with the effective surface density $n_{\rm imp} = 10^{12}$ cm^{-2}, which is evaluated for several ion concentrations in the range $c = 10^{-4}$ M to $c = 1$M by using the RPA for graphene's polarizability with several charge carrier densities: $\bar{n} = 10^{11}$, 10^{12}, and 10^{13} cm^{-2}. We show the results for both uncorrelated $[I(q) = 1]$ and correlated charged impurities described by a step-like pair correlation function that yields $I(q)$ given in Eq. (6.56) with $r_c = 1/\sqrt{\pi n_{\rm imp}} \approx 5.6$ nm. One notices that the magnitude of the auto-correlation function $C(r)$ is generally reduced by increasing ion concentration for all distances r, but this effect is much weaker for correlated than for uncorrelated impurities, as exemplified by a much smaller spread among the curves in the former case. Moreover, the results for correlated impurities show almost no sensitivity to increasing charge carrier density in graphene, which is seen in Fig. 6.3 to affect only the magnitude of the auto-correlation function for uncorrelated impurities, mostly at low ion concentrations, $c < 0.01$ M. However, while the values of the auto-correlation function $C(r)$ are strictly positive at all distances in the case of uncorrelated impurities, one notices that for the correlated impurities there exist broad regions around $r \approx 4.5$ nm where $C(r)$ takes negative values. It should be mentioned that this is not a consequence of quantum effects due to our using the RPA polarizability of graphene, because the results for the auto-correlation function obtained with the TF polarizability (not shown in Fig. 6.3) also exhibit negative values for correlated impurities at roughly the same distances as those seen in Fig. 6.3. Given that the regions of negative auto-correlation are almost unaffected by the increasing charge carrier density in graphene, and are very weakly affected by the ion concentration in the electrolyte, it is remarkable that both systems so poorly screen out the effects of spatial correlation among the charged impurities. We note that similar negative auto-correlation in the spatial distribution of electron-hole puddles due to sub-surface charges for mono-layer graphene without electrolyte was observed recently using various experimental techniques [92, 93].

In Fig. 6.4 we show the reduced variance $\bar{C}(0) = C(0)\,[d/(Ze)]^2$ as a function of c in units of M for three ensembles of point charges with the effective surface densities $n_{\rm imp} = 10^{11}$, 10^{12}, and 10^{13} cm^{-2}, which is evaluated by using the RPA for graphene's polarizability with several charge carrier densities: $\bar{n} = 0$, 10^{11}, 10^{12}, and 10^{13} cm^{-2}. The results are shown for both uncorrelated $[I(q) = 1]$ and correlated charged impurities with

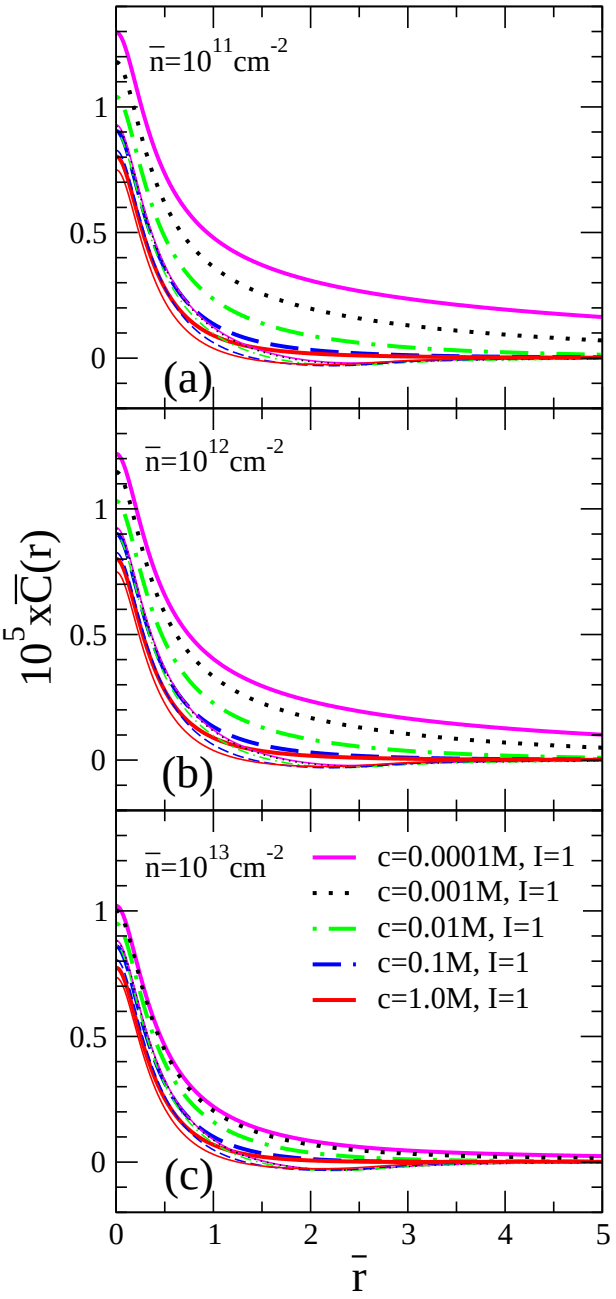

Figure 6.3: Reduced auto-correlation function of the potential in the plane of graphene, $\bar{C}(\bar{r}) = C(\bar{r})\,[d/(Ze)]^2$, shown as a function of the reduced distance $\bar{r} = rq_0$, where $q_0^{-1} = 2.1$ nm, due to an ensemble of charged impurities at the depth $d = 2$ Å with the effective surface density $n_{\rm imp} = 10^{12}$ cm^{-2}, for several values of the average charge carrier density in graphene: (a) $\bar{n} = 10^{11}$ cm^{-2}, (b) $\bar{n} = 10^{12}$ cm^{-2}, and (c) $\bar{n} = 10^{13}$ cm^{-2}, and for several ion concentrations in the electrolyte: $c = 10^{-4}$ M [solid (pink) lines], $c = 10^{-3}$ M (dotted black lines), $c = 10^{-2}$ M [dash-dotted (green) lines], $c = 10^{-1}$ M [dashed (blue) lines], and $c = 1$ M [solid (red) lines]. Thick lines show the results for uncorrelated impurities with the structure factor $I(q) = 1$, and the thin lines show the results for $I(q)$ given in Eq. (6.56) with $r_c = 1/\sqrt{\pi n_{\rm imp}}$.

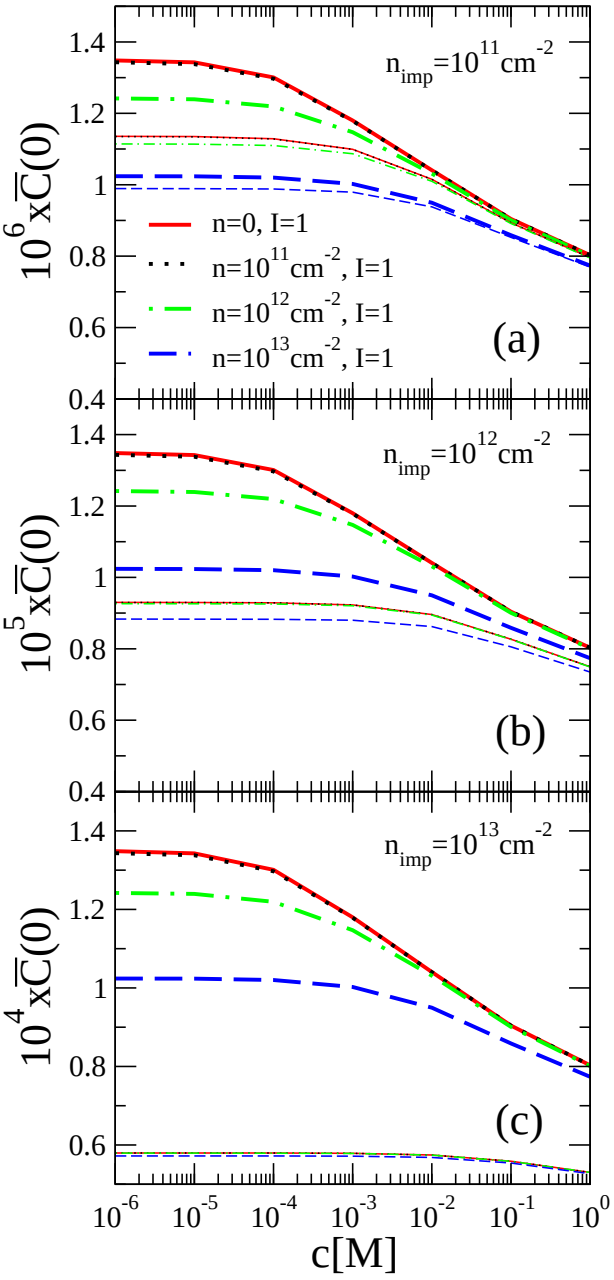

Figure 6.4: Reduced variance of the potential in the plane of graphene, $\bar{C}(0) = C(0)\,[d/(Ze)]^2$, shown as a function of the ion concentration in the electrolyte c in units of M (mol/litre), for three ensembles of point charges at depth $d = 2$ Å with the effective surface densities: (a) $n_{\rm imp} = 10^{11}$ cm^{-2}, (b) $n_{\rm imp} = 10^{12}$ cm^{-2}, and (c) $n_{\rm imp} = 10^{13}$ cm^{-2}, for several values of the average charge carrier density in graphene: $\bar{n} = 0$ [solid (red) lines], $\bar{n} = 10^{11}$ cm^{-2} (dotted black lines), $\bar{n} = 10^{12}$ cm^{-2} [dash-dotted (green) lines], and $\bar{n} = 10^{13}$ cm^{-2} [dashed (blue) lines]. Thick lines show the results for uncorrelated impurities with the structure factor $I(q) = 1$, and the thin lines show the results for $I(q)$ given in Eq. (6.56) with $r_c = 1/\sqrt{\pi n_{\rm imp}}$.

the structure factor given in Eq. (6.56). One notices that the variance generally appears to have constant values for small values of c and starts decreasing when c exceeds certain threshold values that increase with increasing $\bar{n}$. One sees that all the curves for $\bar{n} = 0$ and 10^{11} cm^{-2} are practically indistinguishable, with a threshold value of $c_0 \approx 10^{-5}$ M beyond which the variance starts decreasing, whereas such a threshold in the case of graphene doped with higher values of $\bar{n}$ seems to scale with the charge carrier density as $c_d \propto \bar{n}$. These observations are consistent with the discussion in subsection 3.0.3 that gave estimates for the threshold values of ion concentration, Eqs. (6.44) and (6.45), for (almost) neutral graphene and for doped graphene, respectively. Further, one may confirm in Fig. 6.4 (via scaling of the vertical axes) that the variance is simply proportional to n_{imp} for uncorrelated impurities, but its magnitude and the rate of decrease with c are strongly reduced with increasing n_{imp} for correlated impurities, while the threshold values of c beyond which this decrease takes place are higher than in the case of uncorrelated impurities. Moreover, the effects of increasing charge carrier density in graphene are heavily suppressed with increasing n_{imp} for correlated impurities. For example, for the highest impurity density shown in Fig. 6.4(c), $n_{\text{imp}} = 10^{13}$ cm^{-2}, one sees that the variances for correlated impurities are drastically reduced in magnitude in comparison with those for uncorrelated impurities, practically identical for all charge carrier densities in graphene, and almost independent of the ion concentration in the electrolyte.

6.3 Concluding remarks

We have presented a model for dual-gated, single-layer graphene, with a metallic back gate electrode separated by a layer of oxide from graphene, and the top gate potential applied through a thick layer of liquid electrolyte that contains a concentration c of mobile ions. Our primary goal is to analyze the effects of ion concentration on graphene's ability to screen the electrostatic potential fluctuation due to random distribution of fixed charges trapped in the oxide-graphene interface. The electric double layer in the electrolyte is described by a diffuse layer in the Debye-Hückel approximation, which is separated from graphene by a charge-free Stern layer.

First, solving the 1D Poisson equation for the planar average of the electrostatic potential throughout the system allows us to derive a nonlinear equation for the average equilibrium charge carrier density in graphene, which includes the gate voltages, potential offsets for each part of the system, as well as the average density of charge carriers. Next, the fluctuating part of the electrostatic potential in the plane of graphene, which gives rise to a potential corrugation that is responsible for increased charge-carrier scattering in graphene and hence an increase in its resistivity, is evaluated by means of the Green's function of the Poisson equation and by invoking the linear response for graphene in both the Random Phase approximation (RPA) and Thomas-Fermi (TF) approximation at non-zero temperature. Results are obtained for the in-plane potential due to a single charge, as well as due to an ensemble of point charges at a fixed depth in the oxide that are characterized

by two models for the spatial correlation in the directions parallel to graphene.

The effect of increased screening of the in-plane potential due to increased ion concentration is shown clearly for the case of single charged impurity, where an addition to the inverse TF screening length of graphene is found in the amount that is proportional to $\sqrt{c}$, with a tendency of saturation at high concentrations, where ion condensation is expected to occur at the boundary between the Stern layer and the diffuse layer. It is also found that Friedel oscillations in the potential due to the quantum effects in the RPA polarization function of doped graphene are accentuated by increased ion concentration. In addition, a prediction is made that the plasmon frequency in doped graphene should exhibit a quasi-acoustic dispersion at long wavelengths due to the ion concentration in the electrolyte, pointing to possible sensing applications via graphene plasmonics.

The effect of increased screening due to increased ion concentration is also confirmed for the auto-correlation function of the in-plane potential due to an ensemble of charged impurities. In the case of uncorrelated impurities, this function is found to be positive for all inter-impurity distances, whereas the effect of ionic screening is observed to be reduced by increasing charge carrier density in graphene, especially at lower ion concentrations, as expected. In the case of correlated impurities, the magnitude of the auto-correlation function is found to be much smaller than in the case of uncorrelated impurities, and in fact is seen to take negative values in a range of inter-impurity distances. Moreover, in comparison to the case of uncorrelated impurities, the auto-correlation function for correlated impurities shows a significantly reduced variation with increased ion concentration in the electrolyte, and almost no variation with the increased charge carrier density in graphene. Similar effects are observed in the dependence of the variance of the in-plane potential on ion concentration, where the reduction of the effect of ion concentration for correlated impurities strengthens as the density of impurities increases.

While the above observations regarding the auto-correlation function are in line with recent theoretical [94, 95] and experimental [92, 93] studies of the statistics of the in-plane potential fluctuations in graphene without electrolyte, we may conclude that the role of mobile ions in the electrolyte in boosting the screening of the in-plane potential fluctuations is strongly suppressed when the impurities are correlated. We stress, however, that such effects of the spatial correlation should not be too surprising since the potential landscape in graphene is expected to be flatter when the distances among the impurities are maximized for a given impurity concentration. Thus, based on our results, it seems that the presence of mobile ions in the electrolyte may be expected to play the most prominent role in cases of uncorrelated impurities, or for very dilute assemblies of charged impurities, when one expects large fluctuations in the electrostatic potential in graphene.

There are several possible directions to develop further the present mathematical model of electrolytically gated graphene. It would be interesting to allow for high ion concentrations and large potential drops across the electric double layer by taking into account the effect of non-zero ion sizes in the electrolyte, [29, 42] as well as the dielectric saturation of the solvent due to possibly large electric fields near graphene [3, 78]. In particular, one

may expect that the degree of ion-ion correlation will increase with increasing ion concentration in the electrolyte, [35] which could give rise to a reversal of the ionic effect, going from a pronounced contribution to graphene's screening ability of the in-plane potential fluctuations to actually increasing the degree of corrugation in that potential at the length scales comparable to the ion-ion correlation length, as was recently observed [96].

Chapter 7

Ionic screening of charged impurities in electrolytically gated graphene: Partially linearized Poisson-Boltzmann equation

In the previous chapter, we have used the Debye-Hückel (DH) approximation for the ion distribution in the diffuse layer, which severely restricts the applicability of the resulting linearized Poisson-Boltzmann (PB) equation to low values of the potential drop across the that layer. In the case when the density of charged impurities is high, such model yields unrealistically high ion concentration close to graphene which would overemphasize the role of the mobile ions in screening those impurities in comparison to the charge density in graphene. In addition, the process of doping the graphene layer to high densities by a top gate immersed in the electrolyte is poorly described by the equations resulting from the solution of the one-dimensional (1D) problem for the surface average of the potential.

To remedy this situation, and still be able to provide an analytically solvable model for the screening of charged impurities by mobile ions, it is possible to resort to a model where the 1D equations for the surface averaged potential are solved exactly using the non-linearized PB equation, while fluctuations of the potential could be obtained by linearizing the resulting equations. In doing so, a linearized equation for the fluctuation potential in the diffuse layer arises with a coefficient that depends on the distance normal to graphene, which still allows an analytical solution. We take advantage of that situation and obtain a solution of the averaged equations that provides a more reliable description of the gating process of graphene at higher potentials than under the DH approximation. Of course, one has to be aware of the limitations that need to be placed on magnitudes of the gating potential and the ion concentration that pertain to the effects of finite ion size and/or dielectric saturation of water.

On the other hand, the availability of an analytical solution to the partially-linearized

PB equation enables us to use the concept of the Green's function, which we extend in this chapter to include, in addition to the charged impurities in the oxide, also charged bio-molecules in the electrolyte close to the Stern layer. In this way, our modeling of the screening gets us one stop closer to biochemical sensor applications of graphene by measuring its conductivity in the presence of an analyte. Moreover, since the effects of randomness of the charged impurities were found to play important role for graphene conductivity [74, 75], we improve in this chapter our model that takes care of the spatial correlation of those impurities. Instead of the simple step-correlation model of the previous chapter we use here the so-called hard-disc model, which provides an analytical expression for the structure factor that is applicable to much higher packing fractions than the step-correlation model.

The mathematical formulation of the problem at hand in this chapter follows the same outline as that in the previous chapter, and some equations will remain the same, but we shall present a complete formulation of our model with the partially-linearized PB equation for the sake of clarity.

7.1 Theoretical model

We consider here the same structure as shown in Fig. 6.1. We assume that the region I_1 contains a distribution of fixed charged impurities, whereas the region I_3 contains mobile salt ions in the electrolyte, which form the electric double layer (EDL), and possibly some small amounts of charged bio-molecules. A single layer of graphene in the plane $z = 0$ is assumed to carry a surface charge density σ_g. Noting that the charge carriers in graphene (electrons and holes) are also mobile, we expect that both the charge carriers in graphene and the mobile ions in the electrolyte will redistribute themselves so as to screen any spatial fluctuation in the electrostatic potential arising from the fixed charged impurities in the oxide substrate or from the charged bio-molecules in the electrolyte adjacent to the surface of graphene.

Similarly to the procedure outlined in the previous chapter, using a Cartesian coordinate system with $\mathbf{R} = (\mathbf{r}, z)$ as in Fig. 6.1, we first rewrite the potential in a piecewise manner as $\Phi_j(\mathbf{R})$ for $z \in I_j$, satisfying the following equations for $j = 1, 2, 3$

$$\epsilon_j \nabla^2 \Phi_j(\mathbf{R}) = -4\pi[\rho_j^{(\text{ion})}(\Phi_j(\mathbf{R})) + \rho_j^{(\text{ext})}(\mathbf{R})], \tag{7.1}$$

where $\rho_j^{(\text{ion})}$ is the local charge density due to mobile ions, defined as

$$\rho_j^{(\text{ion})}(\Phi_j(\mathbf{R})) = \begin{cases} 0 & \text{for} \quad j = 1, 2 \\ -2Zec \sinh\{\beta Ze[\Phi_3(\mathbf{R}) - \Phi_3(\infty)]\} & \text{for} \quad j = 3, \end{cases} \tag{7.2}$$

with $\beta = \frac{1}{k_B T}$ and $\Phi_3(\infty)$ being the (constant) value of the potential deep in the bulk of the electrolyte, $z \to \infty$, determined by a top gate. Moreover, we assume that the external

charge density in Eq. (7.1) may be decomposed into the density of charged impurities $\rho_{\rm imp}(\mathbf{R})$ in the region I_1 occupied by oxide and the density of charged bio-molecules $\rho_{\rm bio}(\mathbf{R})$ in the region I_3 occupied by electrolyte, so that

$$\rho_j^{(\rm ext)}(\mathbf{R}) = \begin{cases} \rho_{\rm imp}(\mathbf{R}) & \text{for} \quad j=1, \\ 0 & \text{for} \quad j=2, \\ \rho_{\rm bio}(\mathbf{R}) & \text{for} \quad j=3. \end{cases} \tag{7.3}$$

The equations (7.1) should be solved subject to the BCs at $z=-t$ and $z\to\infty$, such that

$$\Phi_1(\mathbf{R})\big|_{z=-t} = \phi_{bg}, \tag{7.4}$$

$$\Phi_3(\mathbf{R})\big|_{z\to\infty} \equiv \Phi_3(\infty) = \phi_{tg}, \tag{7.5}$$

where ϕ_{bg} and ϕ_{tg} are the (constant) electrostatic potentials at the back gate at $z=-t$ and at the top gate deep in the electrolyte, respectively. In addition, the electrostatic potential has to satisfy the following MCs at $z=0$ and $z=h$,

$$\Phi_1(\mathbf{R})\big|_{z=0} = \Phi_2(\mathbf{R})\big|_{z=0} \equiv \phi_0(\mathbf{r}) \tag{7.6}$$

$$\Phi_2(\mathbf{R})\big|_{z=h} = \Phi_3(\mathbf{R})\big|_{z=h} \tag{7.7}$$

$$-\epsilon_2 \left.\frac{\partial\Phi_2(\mathbf{R})}{\partial z}\right|_{z=0} + \epsilon_1 \left.\frac{\partial\Phi_1(\mathbf{R})}{\partial z}\right|_{z=0} = 4\pi\sigma_g[\phi_0(\mathbf{r})] \tag{7.8}$$

$$\epsilon_2 \left.\frac{\partial\Phi_2(\mathbf{R})}{\partial z}\right|_{z=h} = \epsilon_3 \left.\frac{\partial\Phi_3(\mathbf{R})}{\partial z}\right|_{z=h}. \tag{7.9}$$

We have defined in Eq. (7.6) the value of the electrostatic potential $\phi_0(\mathbf{r})$ in the plane $z=0$, which only depends on the lateral position $\mathbf{r}=(x,y)$ and we have indicated in Eq. (7.8) the charge density on graphene is a functional $\sigma_g[\phi_0(\mathbf{r})]$ of that potential.

We now assume that all quantities may be written as the sum of their average value taken over the large area $\mathcal{A}$ of graphene plus a small fluctuating part, as in Eqs. (6.12), (6.13), and (6.14), with the surface averages given in Eqs. (6.10), (6.11) and (6.15). To those equations we add in this chapter also the volume density of charged biomolecules in the region I_3,

$$\rho_{\rm bio}(\mathbf{R}) = \bar{\rho}_{\rm bio}(z) + \delta\rho_{\rm bio}(\mathbf{R}), \tag{7.10}$$

but we assume, for the sake of simplicity, that the average density of charged bio-molecules vanishes, $\bar{\rho}_{\rm bio}(z)=0$, even though its fluctuating part $\delta\rho_{\rm bio}(\mathbf{R})$ may be nonzero in region I_3. This assumption should be lifted in cases when graphene is used to probe charged membranes in the nearby electrolyte, such as lipid bilayers or arrays of single-stranded DNA molecules. However, in that case the solution of the equations for the average potential in the electrolyte become challenging.

For the charge density on graphene, $\sigma_g[\phi_0(\mathbf{r})]$, we use the same decomposition as that given in Eq. (6.16), where the average density, $\bar{\sigma}_g$, may be expressed in terms of the average potential in the plane of graphene, $\bar{\phi}_0$, as $\bar{\sigma}_g(\bar{\phi}_0) = -en(\varepsilon_{\rm F} + e\bar{\phi}_0)$, with the equilibrium surface density of charge carriers $n(\mu)$ given in Eq. (2.39), whereas the fluctuating part is given in the configuration space by a linear-response relation,

$$\delta\sigma_g(\mathbf{r}) = -e^2 \int \mathcal{X}(\mathbf{r}-\mathbf{r}')\delta\phi_0(\mathbf{r}')\, d^2\mathbf{r}', \tag{7.11}$$

with the response function $\mathcal{X}(\mathbf{r})$ being an inverse 2DFT of the static polarizability of graphene $\chi(\mathbf{q})$. It should be noted that $\chi(\mathbf{q})$ and hence $\mathcal{X}(\mathbf{r})$ are strongly dependent on the equilibrium charge density $\bar{\sigma}_g(\bar{\phi}_0)$ on graphene that is generally achieved through a dual gating process described in Fig. 6.1.

As for the density of mobile ions, which is only nonzero in the region I_3 by Eq. (7.2), we also write it as the sum of an average part and a fluctuation part as

$$\rho_3^{(\rm ion)}(\Phi_3(\mathbf{R})) = \bar{\rho}_3^{(\rm ion)}(\bar{\Phi}_3(z)) + \delta\rho_3^{(\rm ion)}(\delta\Phi_3(\mathbf{R})). \tag{7.12}$$

If we further assume that $|\delta\Phi_3(\mathbf{R})| \ll |\bar{\Phi}_3(z) - \bar{\Phi}_3(\infty)|$ in the region I_3, where $\bar{\Phi}_3(\infty) = \Phi_3(\infty) \equiv \phi_{tg}$, then Eq. (7.12) yields to the first order in $\delta\Phi_3$

$$\begin{aligned}
\rho_3^{(\rm ion)}(\Phi_3(\mathbf{R})) = &- 2Zec\,\sinh\{\beta Ze[\bar{\Phi}_3(z) - \bar{\Phi}_3(\infty) + \delta\Phi_j(\mathbf{R})]\} &(7.13)\\
\approx &- 2Zec\,\sinh\{\beta Ze[\bar{\Phi}_3(z) - \bar{\Phi}_3(\infty)]\} &(7.14)\\
&- 2\beta(Ze)^2 c\,\delta\Phi_3(\mathbf{R})\,\cosh\{\beta Ze[\bar{\Phi}_3(z) - \bar{\Phi}_3(\infty)]\}. &(7.15)
\end{aligned}$$

Thus, the average and the fluctuation parts of $\rho_3^{(\rm ion)}$ in the region I_3 are written as

$$\begin{aligned}
\bar{\rho}_3^{(\rm ion)}(\bar{\Phi}_3(z)) &= -2Zec\,\sinh\{\beta Ze[\bar{\Phi}_3(z) - \bar{\Phi}_3(\infty)]\}, &(7.16)\\
\delta\rho_3^{(\rm ion)}(\delta\Phi_3(\mathbf{R})) &= -2\beta(Ze)^2 c\,\delta\Phi_3(\mathbf{R})\cosh\{\beta Ze[\bar{\Phi}_3(z) - \bar{\Phi}_3(\infty)]\}. &(7.17)
\end{aligned}$$

Finally, Eq. (7.1) now becomes in the three regions with $j = 1, 2, 3$

$$\nabla^2[\bar{\Phi}_1(z) + \delta\Phi_1(\mathbf{R})] = -\frac{4\pi}{\epsilon_1}[\bar{\rho}_{\rm imp}(z) + \delta\rho_{\rm imp}(\mathbf{R})], \tag{7.18}$$

$$\nabla^2[\bar{\Phi}_2(z) + \delta\Phi_2(\mathbf{R})] = 0, \tag{7.19}$$

$$\nabla^2[\bar{\Phi}_3(z) + \delta\Phi_3(\mathbf{R})] = -\frac{4\pi}{\epsilon_3}[\bar{\rho}_3^{(\rm ion)}(\bar{\Phi}_3(z)) + \delta\rho_3^{(\rm ion)}(\delta\Phi_j(\mathbf{R})) + \delta\rho_{\rm bio}(\mathbf{R})], \tag{7.20}$$

where in the last equation we have set $\bar{\rho}_{\rm bio}(z) = 0$, by assumption. In the following sections we shall solve separately both the averaged and the fluctuating parts of each of these equations.

7.1.1 Averaged part of partially linearized Poisson-Boltzmann equation

For the averaged parts of Eqs. (7.18), (7.19) and (7.20) we obtain the following set of ODEs in regions $j = 1, 2, 3$,

$$\epsilon_1 \frac{\mathrm{d}^2\bar{\Phi}_1(z)}{\mathrm{d}z^2} = -4\pi\bar{\rho}_{\mathrm{imp}}(z), \tag{7.21}$$

$$\epsilon_2 \frac{\mathrm{d}^2\bar{\Phi}_2(z)}{\mathrm{d}z^2} = 0, \tag{7.22}$$

$$\frac{\mathrm{d}^2\bar{\Phi}_3(z)}{\mathrm{d}z^2} = 8\pi\frac{Zec}{\epsilon_3}\,\sinh\{\beta Ze[\bar{\Phi}_3(z) - \bar{\Phi}_3(\infty)]\}. \tag{7.23}$$

We assume that the averaged potential satisfies the same BCs,

$$\bar{\Phi}_1(-t) = \phi_{bg}, \tag{7.24}$$

$$\bar{\Phi}_3(\infty) = \phi_{tg} \tag{7.25}$$

and the same MCs,

$$\bar{\Phi}_1(0) = \bar{\Phi}_2(0) \equiv \bar{\phi}_0 \tag{7.26}$$

$$\bar{\Phi}_2(h) = \bar{\Phi}_3(h) \equiv \bar{\phi}_h \tag{7.27}$$

$$-\epsilon_2\frac{\mathrm{d}\bar{\Phi}_2(0)}{\mathrm{d}z} + \epsilon_1\frac{\mathrm{d}\bar{\Phi}_1(0)}{\mathrm{d}z} = 4\pi\bar{\sigma}_g(\bar{\phi}_0) \tag{7.28}$$

$$\epsilon_2\frac{\mathrm{d}\bar{\Phi}_2(h)}{\mathrm{d}z} = \epsilon_3\frac{\mathrm{d}\bar{\Phi}_3(h)}{\mathrm{d}z}, \tag{7.29}$$

as the full potential in the previous subsection, with the only difference being the use of the average charge density on graphene in Eq. (7.28). Note that in Eq. (7.27) we have defined the surface average of the potential $\bar{\phi}_h$ in the plane $z = h$, i.e., at the boundary between the Stern layer and electrolyte.

Solving Eq. (7.21) with the BC in Eq. (7.24) gives an expression in Eq. (6.21), whereas the general solution of Eq. (7.22) in the Stern layer is given in Eq. (6.22). Using the MCs in Eqs. (7.26), (7.27), (7.28) and (7.29) we can determine the coefficients A, B and C, as well as the average potential $\bar{\phi}_h$.

However, unlike the linear equation in Eq. (6.23) in the DH approximation for the region I_3, the nonlinear equation in Eq. (7.23) requires special treatment. It can be reduced to the one-dimensional non-linearized PB equation, Eq. (4.4), which may be further written in terms of a non-dimensional electrostatic potential $\psi(z) = \beta Ze[\bar{\Phi}_3(z) - \bar{\Phi}_3(\infty)]$ as

$$\frac{d^2\psi(z)}{dz^2} = \kappa^2\sinh[\psi(z)]. \tag{7.30}$$

Solving this equation subject to the BC in Eq. (7.25), which gives $\psi(\infty) = 0$, one obtains [16]

$$\psi(z) = 4\tanh^{-1}[e^{-\kappa(z+z_0)}]\,\mathrm{sign}(\psi_h), \tag{7.31}$$

where $\psi_h \equiv \psi(h) = \beta Ze(\bar{\phi}_h - \phi_{tg})$ is a non-dimensional average of the potential drop across the diffuse layer in the electrolyte. In Eq. (7.31) we introduced an auxiliary parameter z_0 defined by

$$z_0 = -h - \frac{1}{\kappa}\ln\left|\tanh\left(\frac{\psi_h}{4}\right)\right|. \tag{7.32}$$

For the calculation of the fluctuation part in the next subsection, we also need an expression

$$\cosh[\psi(z)] = 1 + 2\,\mathrm{cosech}^2[\kappa\,(z + z_0)], \tag{7.33}$$

which is easily deduced from the solution in Eq. (7.31).

Finally, from the BCs in Eqs. (7.24) and (7.25) and from MCs in Eqs. (7.26), (7.27), (7.28) and (7.29) we obtain two coupled transcendental equations, which determine the average potential on graphene $\bar{\phi}_0$ (and hence the average charge density on graphene $\sigma_0(\bar{\phi}_0)$), as well as the potential $\bar{\phi}_h$ (and hence the parameters ψ_h and z_0 that determine the ionic charge accumulated in the EDL) in terms of the externally applied gate potentials $\phi_{bg} = \bar{\Phi}_1(-t)$ and $\phi_{tg} = \bar{\Phi}_3(\infty)$ as

$$C_{ox}(\bar{\phi}_0 - \phi_{bg}) + C_S(\bar{\phi}_0 - \bar{\phi}_h) = \bar{\sigma}_g(\bar{\phi}_0) + \bar{\sigma}_{\mathrm{imp}} \tag{7.34}$$

$$C_{ox}(\bar{\phi}_0 - \phi_{bg}) + \frac{\epsilon_3\kappa}{2\pi\beta Ze}\sinh\left(\frac{\psi_h}{2}\right) = \bar{\sigma}_g(\bar{\phi}_0) + \bar{\sigma}_{\mathrm{imp}} \tag{7.35}$$

where $C_{ox} = \epsilon_1/(4\pi t)$ and $C_S = \epsilon_2/(4\pi h)$ are defined as the capacitances per unit area of the oxide layer and the Stern layer, respectively. In the above equations, $\bar{\sigma}_{\mathrm{imp}}$ is the average surface density of charged impurities in the oxide given in Eq. (6.29). The equations Eq. (7.34) and (7.35) may be used to determine the average doping density $\bar{\sigma}_g$ of graphene in the regime of dual gating. Then, one may determine μ from the relation $\bar{\sigma}_g = -en(\mu)$ via Eq. (2.39), and use this μ value to calculate the polarizability $\chi(q)$ of doped graphene.

7.1.2 Fluctuating part of partially linearized Poisson-Boltzmann equation

We want to determine how the fluctuations in the electrostatic potential in the plane of graphene, which arise from the randomness in the positions of charged impurities in the oxide, will be screened by the charged impurities in graphene and by the mobile ions in the electrolyte. This can be achieved in a compact and elegant manner by using the method of Green's function to solve the partially linearized PB equation.

For the fluctuating parts of Eqs. (7.18), (7.19) and (7.20) we obtain in regions $j = 1, 2, 3$ the following set of linear second-order PDEs

$$\nabla^2\delta\Phi_1(\mathbf{R}) = -\frac{4\pi}{\epsilon_1}\delta\rho_{\mathrm{imp}}(\mathbf{R}), \tag{7.36}$$

$$\nabla^2 \delta\Phi_2(\mathbf{R}) = 0, \tag{7.37}$$

$$\nabla^2 \delta\Phi_3(\mathbf{R}) - \frac{8\pi\beta(Ze)^2 c}{\epsilon_3} \cosh\{\beta Ze[\bar{\Phi}_3(z) - \bar{\Phi}_3(\infty)]\}\delta\Phi_3(\mathbf{R}) = -\frac{4\pi}{\epsilon_3}\delta\rho_{\text{bio}}(\mathbf{R}), \tag{7.38}$$

which must satisfy the homogeneous BCs,

$$\delta\Phi_1(\mathbf{R})|_{z=-t} = 0, \tag{7.39}$$

$$\delta\Phi_3(\mathbf{R})|_{z\to\infty} = 0, \tag{7.40}$$

and the following MCs at $z = 0$ and $z = h$,

$$\delta\Phi_1(\mathbf{R})|_{z=0} = \delta\Phi_2(\mathbf{R})|_{z=0} \equiv \delta\phi_0(\mathbf{r}) \tag{7.41}$$

$$\delta\Phi_2(\mathbf{R})|_{z=h} = \delta\Phi_3(\mathbf{R})|_{z=h} \tag{7.42}$$

$$-\epsilon_2 \left.\frac{\partial\delta\Phi_2(\mathbf{R})}{\partial z}\right|_{z=0} + \epsilon_1 \left.\frac{\partial\delta\Phi_1(\mathbf{R})}{\partial z}\right|_{z=0} = 4\pi\,\delta\sigma_g[\delta\phi_0(\mathbf{r})] \tag{7.43}$$

$$\epsilon_2 \left.\frac{\partial\delta\Phi_2(\mathbf{R})}{\partial z}\right|_{z=h} = \epsilon_3 \left.\frac{\partial\delta\Phi_3(\mathbf{R})}{\partial z}\right|_{z=h}. \tag{7.44}$$

Note that $\delta\sigma_g(\mathbf{r})$ in Eq. (7.43) was defined in Eq. (7.11) as a linear functional of the fluctuating potential in the plane of graphene, $\delta\phi_0(\mathbf{r})$. The above equations will be used to derive a full Green's function for the fluctuating potential in the structure shown in Fig. 6.1 in the presence of arbitrary values of the gate potentials and the average density of charged impurities. However, following the procedure outlined in the Appendix 8.5 based on the Dyson-Schwinger (DS) equation, we may safely omit graphene from the calculations of the GF and include it later by using the DS equation approach. Hence we set $\delta\sigma_g[\delta\phi_0(\mathbf{r})] = 0$ in Eq. (7.43) and proceed to find the GF for the structure in Fig. 6.1 without graphene. The details of such procedure are give in the Appendix 8.5.

It is noteworthy that we may substitute $\cosh\{\beta Ze[\bar{\Phi}_3(z) - \bar{\Phi}_3(\infty)]\} = \cosh[\psi(z)]$ in the left-hand side of Eq. (7.38), and use the identity given in Eq. (7.33) to obtain a more compact form of the partially linearized PB equation in the electrolyte,

$$\nabla^2 \delta\Phi_3(\mathbf{R}) - \kappa^2 \left\{1 + 2\,\text{csch}^2[\kappa\,(z + z_0)]\right\} \delta\Phi_3(\mathbf{R}) = -\frac{4\pi}{\epsilon_3}\delta\rho_{\text{bio}}(\mathbf{R}), \tag{7.45}$$

where we have defined csch as a shorthand for the cosech function. Notice that, through the parameter z_0, this equation contains information about the average charge densities in the overall structure and the external gate potentials from Eqs. (7.34) and (7.35).

Owing to the 2D translational invariance of the structure, we may now apply the 2DFT to the fluctuating potentials $\delta\Phi_j(\mathbf{R}) \equiv \delta\Phi_j(\mathbf{r}, z)$ for all j, defined as

$$\tilde{\Phi}_j(\mathbf{q}, z) = \int \mathrm{e}^{-i\mathbf{q}\cdot\mathbf{r}}\delta\Phi_j(\mathbf{r}, z)\, d^2\mathbf{r}, \tag{7.46}$$

with similar definitions for the fluctuating parts of the densities of charged impurities and bio-molecules, $\widetilde{\rho}_{\rm imp}(\mathbf{q},z)$ and $\widetilde{\rho}_{\rm bio}(\mathbf{q},z)$, respectively. As a result, we obtain from Eqs. (7.36), (7.38) and (7.38),

$$\frac{\partial\tilde{\Phi}_1(\mathbf{q},z)}{\partial z^2}-q^2\tilde{\Phi}_1(\mathbf{q},z)=-\frac{4\pi}{\epsilon_1}\widetilde{\rho}_{\rm imp}(\mathbf{q},z), \tag{7.47}$$

$$\frac{\partial\tilde{\Phi}_2(\mathbf{q},z)}{\partial z^2}-q^2\tilde{\Phi}_2(\mathbf{q},z)=0, \tag{7.48}$$

$$\left\{\frac{\partial^2}{\partial z^2}-q^2-\kappa^2-2\kappa^2{\rm csch}^2\left[\kappa\left(z+z_0\right)\right]\right\}\tilde{\Phi}_3(\mathbf{q},z)=-\frac{4\pi}{\epsilon_3}\widetilde{\rho}_{\rm bio}(\mathbf{q},z). \tag{7.49}$$

It can be shown that there are two linearly independent eigenfunctions of the differential operator on the left-hand side in Eq. (7.49), which are defined for $z\geq h$ by

$$U_+(z) = e^{z\sqrt{q^2+\kappa^2}}\left\{1-\frac{\coth[\kappa(z+z_0)]}{\sqrt{q^2+\kappa^2}}\kappa\right\}, \tag{7.50}$$

$$U_-(z) = e^{-z\sqrt{q^2+\kappa^2}}\left\{1+\frac{\coth[\kappa(z+z_0)]}{\sqrt{q^2+\kappa^2}}\kappa\right\}, \tag{7.51}$$

with the corresponding derivatives being

$$U'_+(z) = \sqrt{q^2+\kappa^2}\,U_+(z)+\frac{\kappa^2}{\sqrt{q^2+\kappa^2}}e^{z\sqrt{q^2+\kappa^2}}\,{\rm csch}^2[\kappa(z+z_0)], \tag{7.52}$$

$$U'_-(z) = -\sqrt{q^2+\kappa^2}\,U_-(z)-\frac{\kappa^2}{\sqrt{q^2+\kappa^2}}e^{-z\sqrt{q^2+\kappa^2}}\,{\rm csch}^2[\kappa(z+z_0)]. \tag{7.53}$$

Hence the Wronskian of those functions is given by

$$W\equiv U_+(z)U'_-(z)-U_-(z)U'_+(z)=-\frac{2q^2}{\sqrt{q^2+\kappa^2}}. \tag{7.54}$$

The above expressions for the eigenfunctions $U_+(z)$ and $U_-(z)$ of the partially linearized PB operator in Eq. (7.49) will be used to construct the components of the FTGF in the region occupied by electrolyte.

7.1.3 Effects of the averaged quantities on screening

To make contact with the externally applied voltages at the top gate and the bottom gate, $V_{\rm tg}$ and $V_{\rm bg}$, we use Eq. (5.12) to reexpress the average charge density on graphene in terms of the doping potential $V_q\equiv\mu/e=\left(\varepsilon_{\rm F}-\bar{\varepsilon}_{\rm D}\right)/e=\varepsilon_{\rm F}/e+\bar{\phi}_0$. We further define the gate potentials as $V_{\rm bg}=\phi_{bg}+\varepsilon_{\rm F}/e$ and $V_{\rm tg}=\phi_{tg}+\varepsilon_{\rm F}/e$ neglecting the potential offsets due to

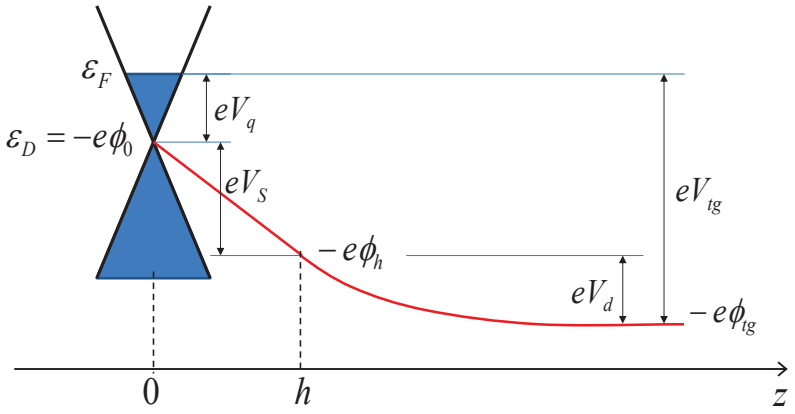

Figure 7.1: Schematic diagram showing the electrostatic potential $\phi(z)$ (red curve) as a function of distance z in electrolytically gated graphene, along with the electron energies at: the Fermi level ε_F, the Dirac point $\varepsilon_D = -e\phi(0) \equiv -e\phi_0$, the Stern plane $-e\phi(h) \equiv -e\phi_h$ and the top gate $-e\phi(\infty) \equiv -e\phi_{tg}$. Also shown are the potential differences that occur: inside graphene at $z = 0$ giving rise to its doping, $V_q = \phi_0 + \varepsilon_F/e$, across the Stern layer, $V_S = \phi_h - \phi_0$ for $0 \le z \le h$, and across the diffuse layer, $V_d = \phi_{tg} - \phi_h$ for $z \ge h$, so that the total applied top gate potential is $V_{\rm tg} = \phi_{tg} + \varepsilon_F/e = V_d + V_S + V_q$. Here, $e > 0$ is the proton charge.

differences in the work functions (or relative electron affinities) between different media. This enables us to write the potential drops across the oxide layer and across the Stern layer as $\bar{\phi}_0 - \phi_{bg} = V_q - V_{\rm bg}$ and $\bar{\phi}_0 - \bar{\phi}_h = V_q + V_d - V_{\rm tg}$, respectively, where $V_d \equiv \phi_{tg} - \bar{\phi}_h$ is the potential drop across the diffuse layer in the electrolyte. We further use Gauss' law to express the effective surface charge density in the diffuse layer as

$$\bar{\sigma}_d(V_d) = \frac{e}{2\pi Z}\,\frac{\kappa}{\lambda_B}\,\sinh\!\left(\frac{1}{2}\beta Z e V_d\right), \tag{7.55}$$

where $\lambda_B = e^2\beta/\epsilon_3$ is the Bjerrum length in the solvent [16]. Thus, the equations Eq. (7.34) and (7.35) may be rewritten as

$$C_{ox}(V_q - V_{\rm bg}) + C_S(V_q + V_d - V_{\rm tg}) = \bar{\sigma}_g(V_q) + \bar{\sigma}_{\rm imp}, \tag{7.56}$$

$$C_{ox}(V_q - V_{\rm bg}) = \bar{\sigma}_d(V_d) + \bar{\sigma}_g(V_q) + \bar{\sigma}_{\rm imp}, \tag{7.57}$$

where $\bar{\sigma}_g(V_q)$ is defined in Eq. (5.12). As in the previous chapter, we shall only consider the case of electrolytically gated graphene, so we set $V_q = V_{\rm tg}$ or take the oxide thickness $t \to \infty$, in which case the left hand side in Eq. (7.57) vanishes, giving rise to the neutrality condition $\bar{\sigma}_d(V_d) + \bar{\sigma}_g(V_q) + \bar{\sigma}_{\rm imp} = 0$. In that case, a schematic diagram of the doping of

graphene with electrons by applying a positive potential to the top gate in the electrolyte is shown in Fig. (7.1).

On the other hand, using the results for the Green's function of partially-linearized PB model given in the Appendix 8.6, one can invoke expressions derived in the previous chapter for the screened potential fluctuations in the plane of graphene in Eq. (6.40) with the effective dielectric function of the system in the presence of graphene in Eq. (6.41). In the case of the partially linearized PB model, the background dielectric constant of the media surrounding the graphene layer is given by

$$\epsilon_{\rm bg}(q) \equiv \frac{1}{2}\left[\epsilon_1 + \epsilon_2 \Gamma_*(q)\right]. \tag{7.58}$$

Here, $\Gamma_*(q)$ generalizes the auxiliary function $\Gamma(q)$ defined in Eq. (E.32) for the DH approximation to

$$\Gamma_*(q) = \frac{\epsilon_2 q \tanh(qh) + \epsilon_3 \Delta}{\epsilon_2 q + \epsilon_3 \Delta \tanh(qh)}, \tag{7.59}$$

where

$$\Delta = \sqrt{q^2+\kappa^2} + \frac{\kappa^2 \mathrm{csch}^2[\kappa(h+z_0)]}{\sqrt{q^2+\kappa^2} + \kappa \coth[\kappa(h+z_0)]}. \tag{7.60}$$

It can be shown that $\coth[\kappa(h+z_0)] = \cosh(\psi_h/2)$ and $\mathrm{csch}[\kappa(h+z_0)] = \sinh(\psi_h/2)$. On the other hand, the effective surface density of charge in the diffuse layer follows from the Gauss' law as $\bar{\sigma}_d = -\frac{e}{2\pi Z}\frac{\kappa}{\lambda_B}\sinh(\psi_h/2)$. Thus, from the neutrality condition for electrolytically gated graphene, $\bar{\sigma}_d + \bar{\sigma}_g + \bar{\sigma}_{\rm imp} = 0$, one may conclude that

$$\Delta = \sqrt{q^2+\kappa^2} + \frac{q_*^2}{\sqrt{q^2+\kappa^2} + \sqrt{q_*^2+\kappa^2}}, \tag{7.61}$$

where

$$q_* = \frac{2\pi}{e} Z \lambda_B \left|\bar{\sigma}_g + \bar{\sigma}_{\rm imp}\right|. \tag{7.62}$$

Notice that by letting $q_* \to 0$ in Eq. (7.62) we recover the expression for the background dielectric constant in the DH approximation in Eq. (6.42), which only depends on the ion concentration in the bulk electrolyte c. Alternatively, Eq. (7.61) mae be rewritten in terms of the potential drop in the diffuse layer as

$$\Delta = \kappa \cosh(\beta Z e V_d/2) + \frac{q^2}{\sqrt{q^2+\kappa^2} + \kappa \cosh(\beta Z e V_d/2)}, \tag{7.63}$$

with the DH limit approached when $\beta|ZeV_d| \ll 1$.

In conclusion, from Eqs. (7.56) and (7.57) one can determine V_q for any combination of the values for the top gate potential $V_{\rm tg}$ and the average charge density of impurities

$\bar{\sigma}_{\rm imp}$. In the next step, one may use Eq. (5.12) to determine the average charge density on graphene, $\bar{\sigma}_g$, which together with $\bar{\sigma}_{\rm imp}$ determines the parameter q_* in Eq. (7.62), which in turn affects the screening ability of the mobile ions of concentration c via Eq. (7.58). On the other hand, using the chemical potential $\mu = eV_q$ in Eq. (B.24) will yield the polarization function of graphene $\chi(q)$ for the given combination of $V_{\rm tg}$ and $\bar{\sigma}_{\rm imp}$.

Referring to Eq. (6.46), the screening of a single point charge at a depth d in the oxide layer may be assessed by considering the contributions of the mobile ions in the electrolyte and the charged impurities in graphene to the effective dielectric function of the entire structure multiplied by the wavenumber, $q\epsilon(q) = q\epsilon_{\rm bg}(q) + 2\pi e^2\chi(q)$, see Eq. (6.41). One concludes that the former screening mechanism may be analyzed via the function $q\epsilon_{\rm bg}(q)$, while the latter screening mechanism is governed by the scaled polarizability of graphene $2\pi e^2\chi(q)$.

7.2 Results

In this section we shall first study the effects of the top gate potential, ion concentration and the density of charged impurities on the equilibrium doping charge density in graphene by solving the fully nonlinear set of equations for the surface averaged quantities. Next, we shall assess the the screening abilities of the mobile ions in the electrolyte and the charge carriers in doped graphene by comparing the q dependencies of the functions $q\epsilon_{\rm bg}(q)$ and $2\pi e^2\chi(q)$.

The effects of various gating conditions of graphene will be further explored by computing the screened potential $\varphi(r)$ due to a single charge defined in Eq. (6.46) and the autocorrelation function $C(r)$ defined in Eq. (6.54) for a distribution of charged impurities determined by a geometric structure factor $I(q)$ defined in Eq. (6.55). In order to study the effects of the spatial correlation between charged impurities, we shall employ in this chapter the model of hard discs, which has a broader range of applicability than the step-correlation model used in the previous chapter.

We shall assume here that the impurities are singly charged, either positively or negatively, with the effective number density per unit area of $\bar{n}_{\rm imp} = \bar{\sigma}_{\rm imp}/e$. Similarly, the charge density of graphene will be characterized by the number density of elementary charges, $\bar{n}_g = \bar{\sigma}_g/e$. Note that both $\bar{n}_{\rm imp}$ and $\bar{n}_g$ are signed quantities, bearing the same sign as the corresponding charge densities $\bar{\sigma}_{\rm imp}$ and $\bar{\sigma}_g$, respectively.

7.2.1 Gating of graphene via averaged solution of the PB equation

We first examine the effect of using the Debye-Hückel (DH) approximation in the equation for the averaged doping potential in graphene given in Eq. (6.30) by setting all the potential

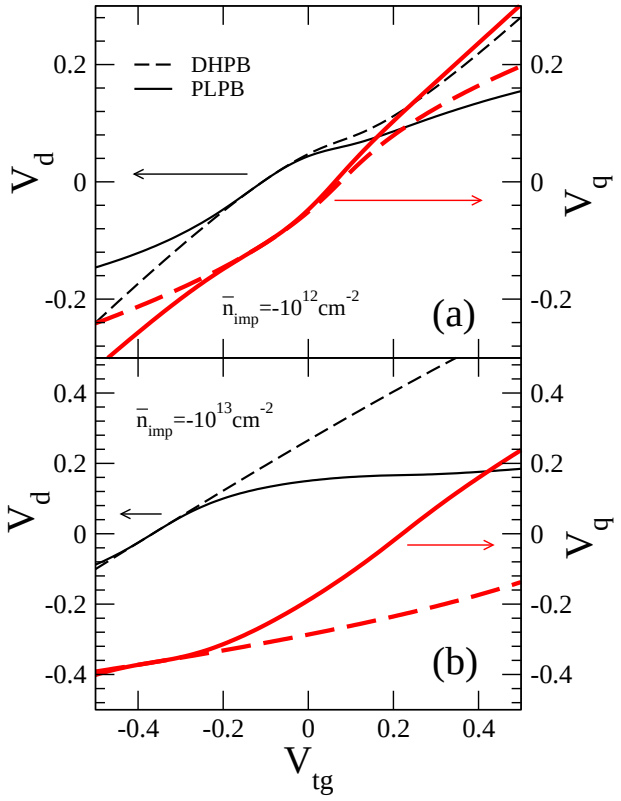

Figure 7.2: The dependence of the doping potential of graphene V_q (in V, thick red lines) and the potential drop in the diffuse layer V_d (in V, thin black lines), as functions of the top gate potential $V_{\rm tg}$ (in V) for ion concentration in the bulk electrolyte of $c = 10^{-4}$ M when the average number density per unit area of (negatively charged) impurities is $\bar{n}_{\rm imp} \equiv \bar{\sigma}_{\rm imp}/e = -10^{12}$ cm^{-2} (panel a) and $\bar{n}_{\rm imp} = -10^{13}$ cm^{-2} (panel b). Results from the nonlinear model in Eqs. (7.56) and (7.57) (solid curves) are compared with the results from the DH approximation in Eq. (6.30) (dashed curves).

offsets to zero. Note that such equation may be obtained from Eqs. (7.56) and (7.57) in the DH limit by assuming $\beta Ze|V_d| \ll 1$ and approximating Eq. (7.55) as $\bar{\sigma}_d \approx C_D\, V_d$ where $C_{\rm D}$ is the Debye capacitance per unit area of the electrolyte defined in Eq. (6.28). Substituting this approximation in Eq. (7.57) enables analytical elimination of V_d from Eqs. (7.56) and (7.57) giving rise to Eq. (6.30) with all offsets $w \to 0$. We shall further assume that doping of graphene only arises from the top gate in the electrolyte and hence we let $C_{\rm ox} \to 0$ in Eq. (6.30). Even though it is not immediately obvious, referring to Eq. (7.55) and keeping in mind that $\kappa \propto \sqrt{c}$, Eq. (4.7), one may assert that large values of the ion concentration c also facilitate the DH approximation giving $\bar{\sigma}_d \approx C_D\, V_d$.

Results for the potential drop in diffuse layer V_d and the doping potential in graphene V_q from Eq. (6.30) are compared in Fig. 7.2 with those from the fully nonlinear set of equations in Eqs. (7.56) and (7.57) for $c = 10^{-4}$ M. One can see in Fig. 7.2 that the DH approximation only gives reliable results for V_d near the value $V_d = 0$ in a relatively

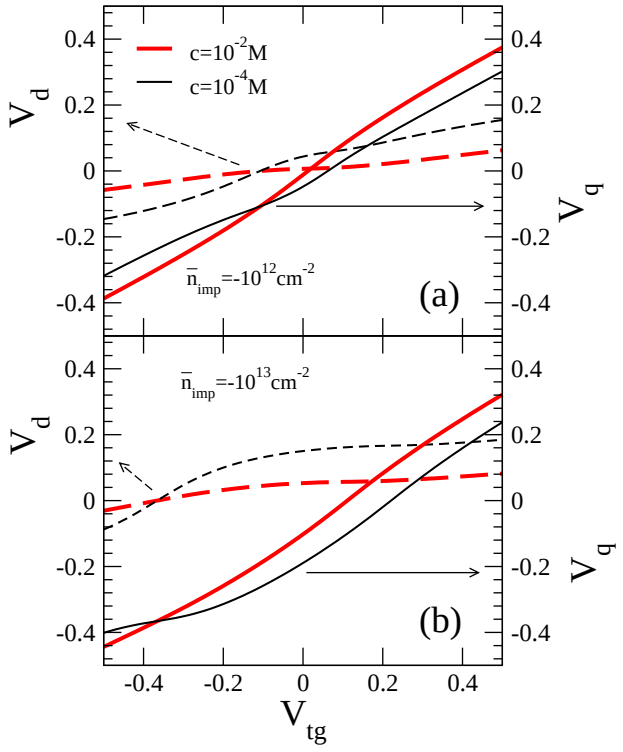

Figure 7.3: The dependence of the doping potential of graphene V_q (in V, solid lines) and the potential drop in the diffuse layer V_d (in V, dashed lines), obtained from Eqs. (7.56) and (7.57) as functions of the top gate potential $V_{\rm tg}$ (in V) for ion concentrations in the bulk electrolyte of $c = 10^{-2}$ M (thick red curves) and $c = 10^{-4}$ M (thin black curves), when the average number density per unit area of (negatively charged) impurities is $\bar{n}_{\rm imp} \equiv \bar{\sigma}_{\rm imp}/e = -10^{12}$ cm^{-2} (panel a) and $\bar{n}_{\rm imp} = -10^{13}$ cm^{-2} (panel b).

narrow window of the top gate potentials of the width $\Delta V_{\rm tg} \sim 0.2$ V. The disagreement between the linear and nonlinear treatments of the average potentials seems to grow fast away from that window for both V_d and V_q. For example, in the case of negatively charged impurities with the density $\bar{n}_{\rm imp} = -10^{13}$ cm^{-2}, the use of the DH approximation for the top gate potential of $V_{\rm tg} \approx 0.5$ V gives a completely false result for the doping potential in graphene of $V_q \approx -0.2$ V, whereas the nonlinear model gives about the same value but with the reversed sign, $V_q \approx 0.2$ V. A calculation of the functions V_d and V_q for a higher ion concentration of, e.g., $c = 10^{-4}$ M (results not shown) exhibits a much broader window of the gate potential values, $\Delta V_{\rm tg} \sim 0.3 - 0.4$ V, than in Fig. 7.2 for which the DHPB model provides a good approximation to the PLPB model. These results clearly point to the need, and advantage of using the PLPB model when the gating of graphene is performed with a large potential drop in the diffuse layer of an electrolyte containing a low concentration of ions.

In Fig. 7.3 we discuss the dependencies of the doping potential in graphene V_q and the potential drop in the diffuse layer V_d on the top gate potential $V_{\rm tg}$, obtained from

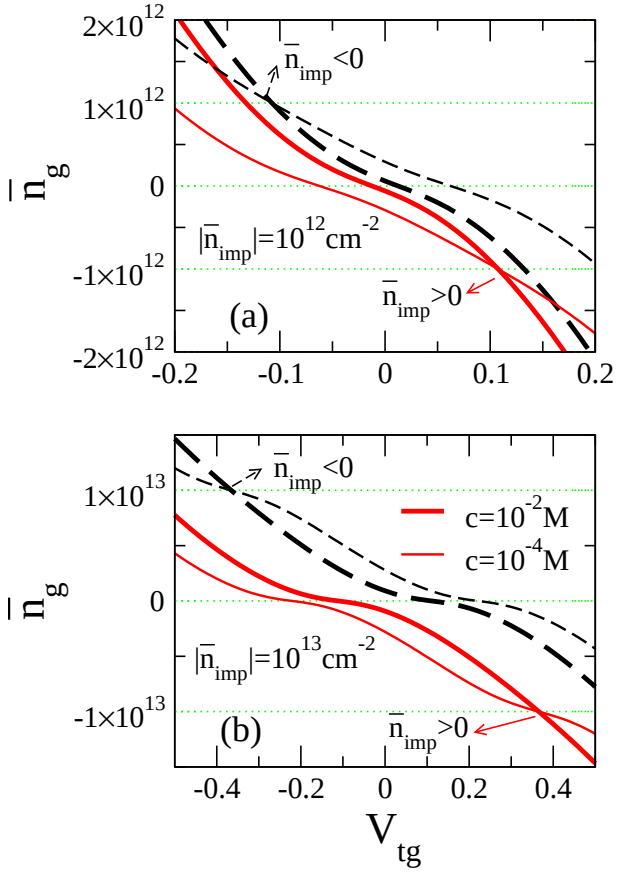

Figure 7.4: The dependence of the average charge density in graphene, $\bar{n}_g = \bar{\sigma}_g/e$ (in cm^{-2}), obtained from Eqs. (7.56) and (7.57), on the top gate potential V_{tg} (in V) for ion concentrations in the bulk electrolyte of $c = 10^{-2}$ M (thick curves) and $c = 10^{-4}$ M (thin curves) in the presence of the positively (solid red curves) and negatively (dashed black curves) singly charged impurities having the average number density per unit area of $|\bar{n}_{\mathrm{imp}}| = 10^{12}$ cm^{-2} (panel a) and $|\bar{n}_{\mathrm{imp}}| = 10^{13}$ cm^{-2} (panel b). Also shown are the horizontal lines (dotted green lines) corresponding to a neutral graphene with $\bar{n}_g = 0$ and with vanishing ion concentrations in the electrolyte when $\bar{n}_g = \mp\bar{n}_{\mathrm{imp}}$ in the cases of positively and negatively charged impurities, respectively.

Eqs. (7.56) and (7.57) for two ion concentrations and two densities of negatively charged impurities. One notices that, generally, a larger fraction of V_{tg} goes to graphene than to the diffuse layer, except when $0 \lesssim V_{\mathrm{tg}} \lesssim 0.2$ V in the case of $\bar{n}_{\mathrm{imp}} = -10^{12}$ cm^{-2} and $0.2 \lesssim V_{\mathrm{tg}} \lesssim 0.4$ V in the case of $\bar{n}_{\mathrm{imp}} = -10^{13}$ cm^{-2}. This demonstrates the efficiency of doping the graphene with a top gate in the electrolyte.

In Fig. 7.4 we show the dependence of the charge density in graphene on the gating potential in the presence of both positively and negatively charged impurities. Notice that the intersection points of the curves with different ion concentrations correspond to the cases when the effective charge density in the electrolyte is zero, that is, when all the

screening of the charged impurities is picked up by graphene at a suitable gate potential. Notice also that the intercepts for negatively charged impurities occur at the same values of the gate potential $V_{\rm tg}$ as the intercepts of curves with different ion concentrations in Fig. 7.3. On the other hand, intercepts of the curves in Fig. 7.4 with the value $\bar{n}_g = 0$, that is, for neutral graphene, show the effects of ion concentration and the charged impurity density on the position of the Dirac point in graphene, which is often measured in experiments by observing the dependence of the minimum conductivity on the gate potential [37, 89, 90]. The lowering of the Dirac point with increasing ion concentration in the positive range of the gate potential was suggested as an indication that the impurities in the substrate are negatively charged [37, 89, 90]. This is corroborated by the intercepts of the dashed curves in Fig. 7.4 with the horizontal line $\bar{n}_g = 0$, giving values in the range $0.1 \lesssim V_{\rm tg} \lesssim 0.3$ V, which decrease with increasing c. Note that, in the cases when graphene is neutral with $\bar{n}_g = 0$, most of the screening of the charged impurities at large distances is picked up by the mobile ions in the electrolyte.

7.2.2 Screening of charged impurities

We next compare the screening of charged impurities within the Debye-Hückel approximation for the Poisson-Boltzmann model, labeled DHPB, and the Partially linearized Poisson-Boltzmann model, labeled PLPB.

In Fig. 7.5 we show the q dependence of the function $q\epsilon_{\rm bg}(q)$, which describes screening by the mobile ions in the electrolyte for two combinations of the ion concentration and the charge density on graphene in the absence of impurities. On notices that the screening by the mobile ions is stronger in the PLPB model than in the DHPB model, and that the differences are more pronounced at long wavelengths, i.e., small wavenumbers q. In fact, it can be shown that $\lim_{q\to 0}\left[q\epsilon_{\rm bg}(q)\right] = 2\pi C^*_{\rm dl}$, where the capacitance of the double layer $C_{\rm dl}* = C_{\rm S}C_{GC}/\left(C_{\rm S} + C_{GC}\right)$ is defined in terms of the Stern layer capacitance $C_{\rm S}$, Eq. (6.27), and the Gouy-Chapman capacitance, $C_{GC} = C_D \cosh\left(\beta Z e V_d/2\right)$, Eq. (5.25), with C_D being the Debye capacitance defined in Eq. (6.28). Note that in the DH approximation $|\beta Z e V_d| \ll 1$ so that $C_{GC} \approx C_D$, as in Eq. (6.43). On the other hand, at the wavenumbers $q \gg 1/h$, the function $q\epsilon_{\rm bg}(q)$ seems the approach an asymptotic slope of $q\left(\epsilon_1 + \epsilon_2\right)/2$, which is independent of the model used. Since this value is determined by the dielectric constant ϵ_2 in the Stern layer rather than the dielectric constant of water, $\epsilon_3 =\approx 80$, it appears that the dielectric saturation and/or the ion crowding near the surface of graphene should play an important role in reducing the screening ability of the large dielectric constant of water. In Fig. 7.5 we also show the q dependence of the scaled polarizability of graphene, $2\pi e^2\chi(q)$. One notices typical saturation at a constant value for $q \to 0$ corresponding to the inverse TF screening length, $2\pi e^2\chi(q) \to q_{\rm TF}$, which appears comparable to the limiting $q \to 0$ values of the function $q\epsilon_{\rm bg}(q)$ in the case of $c = 10^{-4}$ M and $\bar{n}_g = 10^{12}$ cm^{-2}. On the other hand, $2\pi e^2\chi(q)$ is seen to approach the line $q\pi r_s/2$, where $r_s = e^2/(\hbar v_F) = 2.19$ for $q \gg k_F$. Thus, one may assert that, generally, the mobile ions provide a more efficient screening mechanism than the charge carriers in graphene, especially at short distances

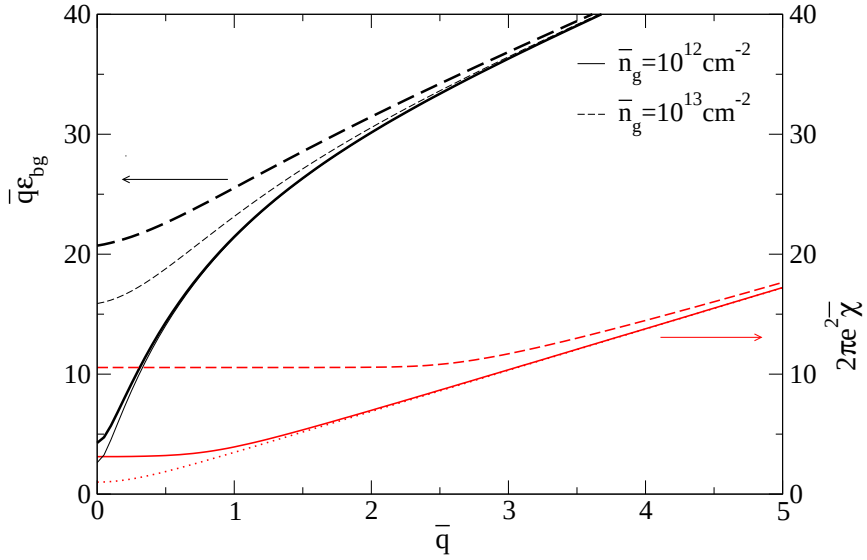

Figure 7.5: The dependence of $\bar{q}\epsilon_{\rm bg}(q)$ (black lines) and $2\pi e^2\bar{\chi}(q)$ (red lines) as functions of the reduced wavenumber $\bar{q}$ (where $\bar{q} = q/q_0$ and $\bar{\chi} = \chi/q_0$ with $q_0 = 0.047$ Å^{-1}) in the absence of impurities, $\bar{n}_{\rm imp} = 0$. Results for the function $\bar{q}\epsilon_{\rm bg}(q)$ describing the screening due to mobile ions are shown for the PLPB model (thick black lines) and the DHPB model (thin black lines), using two combinations of the ion concentration c in the bulk electrolyte and the average charge density $\bar{n}_g$ in graphene: $c = 10^{-4}$ M and $\bar{n}_g = 10^{12}$ cm^{-2} (solid black lines) and $c = 10^{-2}$ M and $\bar{n}_g = 10^{13}$ cm^{-2} (dashed black lines). The reduced polarization function of graphene $2\pi e^2\bar{\chi}(q)$ is shown for a neutral graphene ($\bar{n}_g = 0$, red dotted line) and for the charge densities of $\bar{n}_g = 10^{12}$ cm^{-2} (red solid line) and $\bar{n}_g = 10^{13}$ cm^{-2} (red dashed line).

(large q), although the two mechanisms of screening may well be comparable at large distances (small q).

We next analyze the potential due to single charged impurity in the PLPB and DHPB models. In Figs. 7.6 and 7.7 we show the screened potential due to single point charges at the depths $d = 2$ Å and $d = 10$ Å in the oxide, respectively, for several combinations of the ion concentration c and the charge density in graphene $\bar{n}_g$. One can see that differences between the two models arise for large $\bar{n}_g$ values and small c values with a general trend that the PLPB model provides a more efficient screening than the DHPB model. Also, the spread among the curves for different ion concentrations in the PLPB model is smaller than the spread between such curves in the DHPB model for the highest charge density in graphene of $\bar{n}_g = 10^{13}$ cm^{-2} shown in Figs. 7.6 and 7.7. It is interesting that for the largest ion concentration of $c = 1$ M, there are no visible differences between the two models for all charge densities in graphene. On the other hand, at the lowest charge density in graphene of $\bar{n}_g = 10^{11}$ cm^{-2} shown in Figs. 7.6 and 7.7, there are no visible differences between the two models for all ion concentrations. Moreover, while the screening seems to be relatively weaker for the larger depth $d = 10$ Å, it is interesting that for $d = 2$ Å one

notices oscillations in the potential for $\bar{n}_g = 10^{13}$ cm^{-2}, which are most pronounced for $c = 1$ M. This effect resembles Friedel oscillations in the potential due to quantum effects in the polarizability of graphene [62, 97], but it is somewhat surprising that it survives even in the presence of strong screening by the mobile ions.

We next study in Fig. 7.8 the r dependence of the autocorrelation function $C(r)$ for several combinations of the ion concentration c and the positive charge density in graphene $\bar{n}_g$, both in the PLPB and DHPB models. Here we assume a negative density of uncorrelated charged impurities at the depth $d = 2$ Å with the effective surface density of $\bar{n}_{\rm imp} = -10^{13}$ cm^{-2}, so that in the case of the charge density of $\bar{n}_g = 10^{13}$ cm^{-2} in graphene, the overall charge density due to mobile ions in the electrolyte vanishes. As expected, in that case there are no differences between the models, but one can see increasing differences as $\bar{n}_g$ decreases, which become more pronounced as the ion concentration c decreases. As with the potential, one sees that the spread among the curves with different ion concentrations in the PLPB model is smaller than the spread between such curves in the DHPB model, and is rather independent of the charge density in graphene.

In Figs. 7.9 and 7.10 we compare the autocorrelation function $C(r)$ for uncorrelated negatively charged impurities with those for correlated impurities at the depth $d = 2$ Å using the PLPB model for several combinations of the ion concentration c and the positive charge density in graphene $\bar{n}_g$. We use the hard disc model to describe spatial correlation between the impurities for two densities, $\bar{n}_{\rm imp} = -10^{12}$ cm^{-2} (with the correlation length $r_c = 7$ nm) and $\bar{n}_{\rm imp} = -10^{13}$ cm^{-2} (with $r_c = 2.2$ nm), which are shown in Figs. 7.9 and 7.10, respectively. Notice that the correlation lengths are chosen so that the packing fractions in both figures have about the same value of $p = \frac{\pi}{4}|\bar{n}_{\rm imp}|r_c^2 \approx 0.385$. One can clearly see that $C(r)$ exhibits a non-monotonic dependence on r in the case of correlated impurities with the narrower and deeper minima in the case of smaller correlation length (and hence larger density $\bar{n}_{\rm imp}$), whereas $C(r)$ decreases monotonically with r for uncorrelated impurities. The dependencies of the results on $\bar{n}_g$ seem to be weaker at the larger $\bar{n}_{\rm imp}$ value. Probably the most striking result is that the curves for the correlated impurities are very tightly packed for various ion concentrations, and they show little dependence on the $\bar{n}_g$ values. At the same time, the curves for the uncorrelated impurities exhibit more spread with different ion concentrations and show more variation with the charge density in graphene.

Finally, in Fig. 7.11 we show the c dependence of variance $C(0)$ for several values of the positive charge density on graphene $\bar{n}_g$ in the PLPB model in the presence of both uncorrelated and correlated negatively charged impurities within the hard disc model. The cases of two densities $\bar{n}_{\rm imp}$ are shown with equal packing fractions as in Figs. 7.9 and 7.10. One notices that correlated impurities exhibit much smaller values of $C(0)$, as well as much weaker dependence on the ion concentration c than uncorrelated impurities. Moreover, the groups of curves with different $\bar{n}_g$ values are much more closely packed in the case of correlated than uncorrelated impurities.

Note that we made choices in the above figures for the values of ion concentration c, charge density of graphene $\bar{n}_g$ and the negatively signed density of charged impurities, so

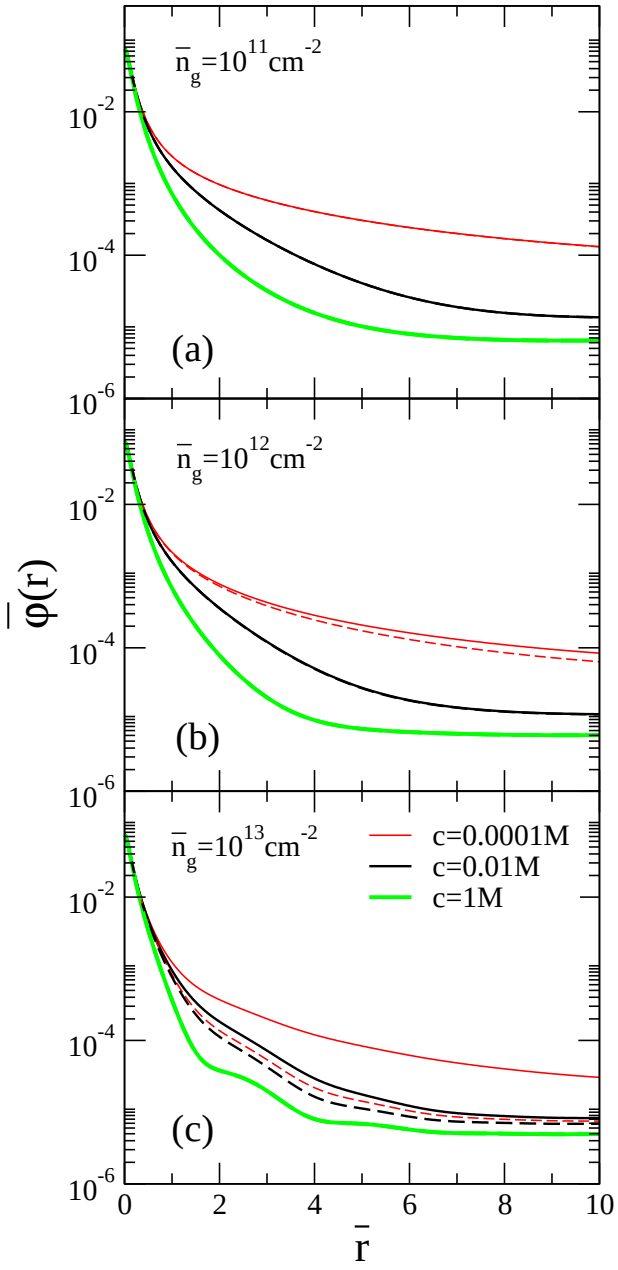

Figure 7.6: Reduced potential in the plane of graphene, $\bar{\varphi} = \varphi\, d/(Ze)$, shown as a function of the reduced distance $\bar{r} = r q_0$, where $q_0^{-1} = 2.1$ nm, due to a single point charge at depth $d = 2$ Å, for several values of the average charge density in graphene: (a) $\bar{n}_g = 10^{11}$ cm^{-2}, (b) $\bar{n}_g = 10^{12}$ cm^{-2}, and (c) $\bar{n}_g = 10^{13}$ cm^{-2}, and for several ion concentrations in the electrolyte: $c = 10^{-4}$ M (thin red lines), $c = 10^{-2}$ M (medium black lines), and $c = 1$ M (thick green lines). Results for the PLPB model are shown with dashed lines and the results for the DHPB model by the solid lines.

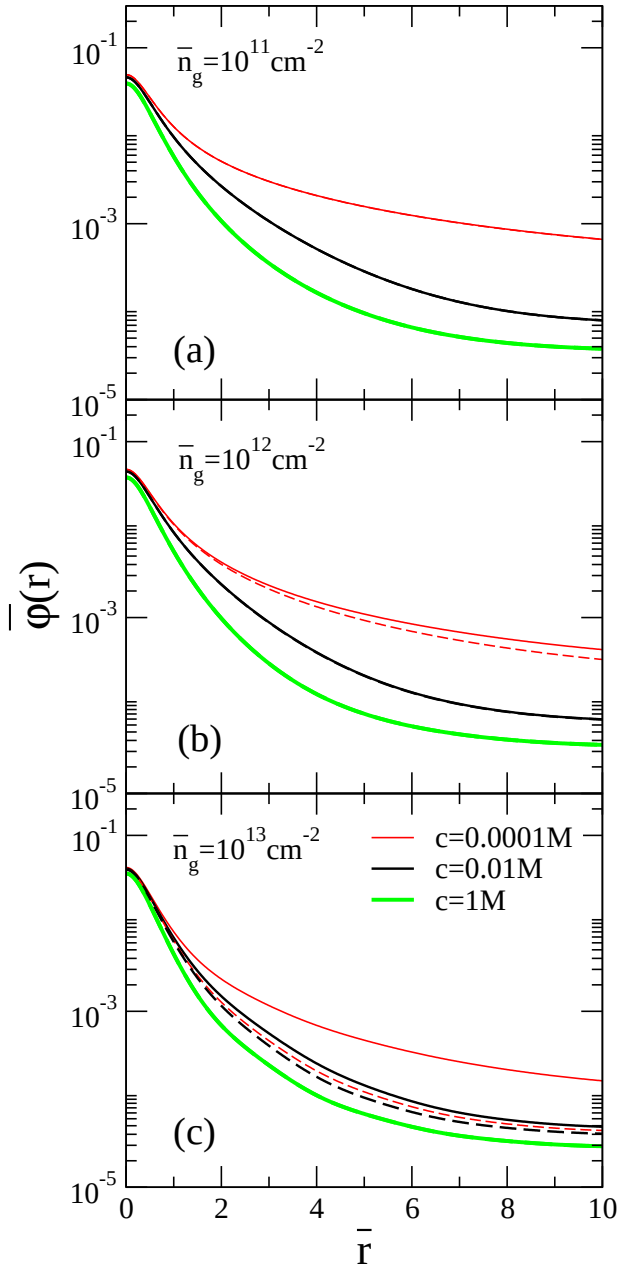

Figure 7.7: Reduced potential in the plane of graphene, $\bar{\varphi} = \varphi\, d/e$, shown as a function of the reduced distance $\bar{r} = r q_0$, where $q_0^{-1} = 2.1$ nm, due to a single point charge at depth $d = 1$ nm, for several values of the average charge density in graphene: (a) $\bar{n}_g = 10^{11}$ cm^{-2}, (b) $\bar{n}_g = 10^{12}$ cm^{-2}, and (c) $\bar{n}_g = 10^{13}$ cm^{-2}, and for several ion concentrations in the electrolyte: $c = 10^{-4}$ M (thin red lines), $c = 10^{-2}$ M (medium black lines), and $c = 1$ M (thick green lines). Results for the PLPB model are shown with dashed lines and the results for the DHPB model by the solid lines.

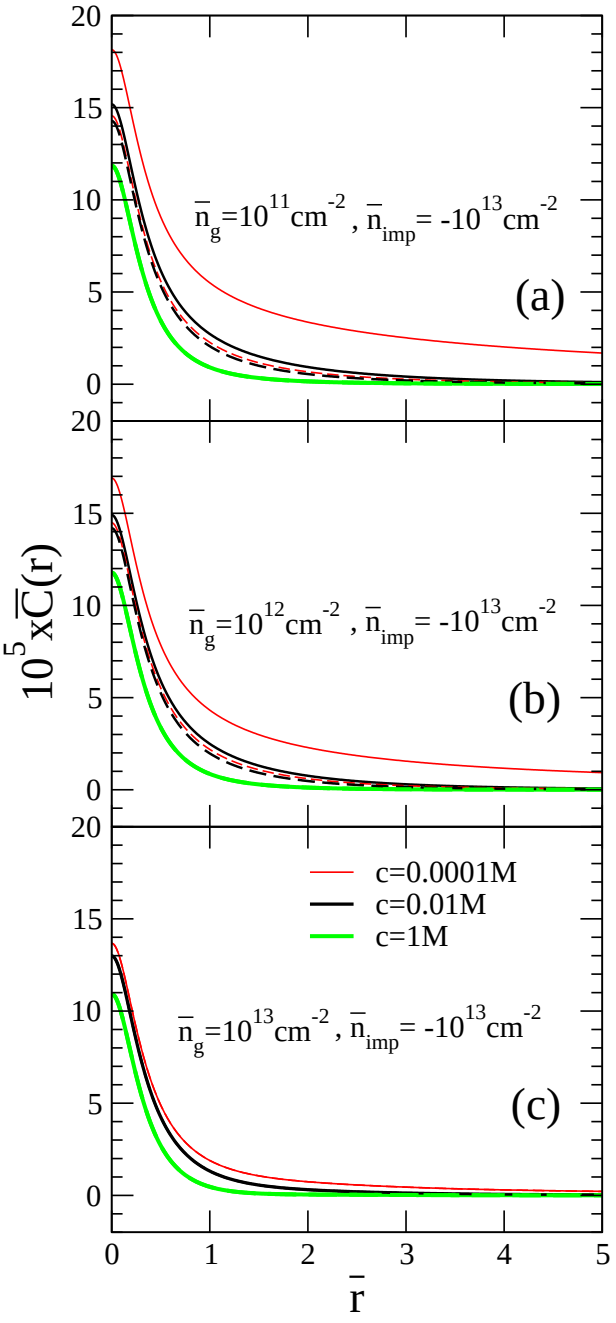

Figure 7.8: Reduced auto-correlation function of the potential in the plane of graphene, $\bar{C}(\bar{r}) = C(\bar{r})\, d^2/e^2$, shown as a function of the reduced distance $\bar{r} = rq_0$, where $q_0^{-1} = 2.1$ nm, due to an ensemble of (negatively charged) uncorrelated impurities at the depth $d =$ 2 Å with the effective surface density $\bar{n}_{\rm imp} = -10^{13}$ cm^{-2}, for several values of the average charge density in graphene: (a) $\bar{n}_g = 10^{11}$ cm^{-2}, (b) $\bar{n}_g = 10^{12}$ cm^{-2}, and (c) $\bar{n}_g = 10^{13}$ cm^{-2}, and for several ion concentrations in the electrolyte: $c = 10^{-4}$ M (thin red lines), $c = 10^{-2}$ M (medium black lines), and $c = 1$ M (thick green lines). Results for the PLPB model are shown with dashed lines and the results for the DHPB model by the solid lines.

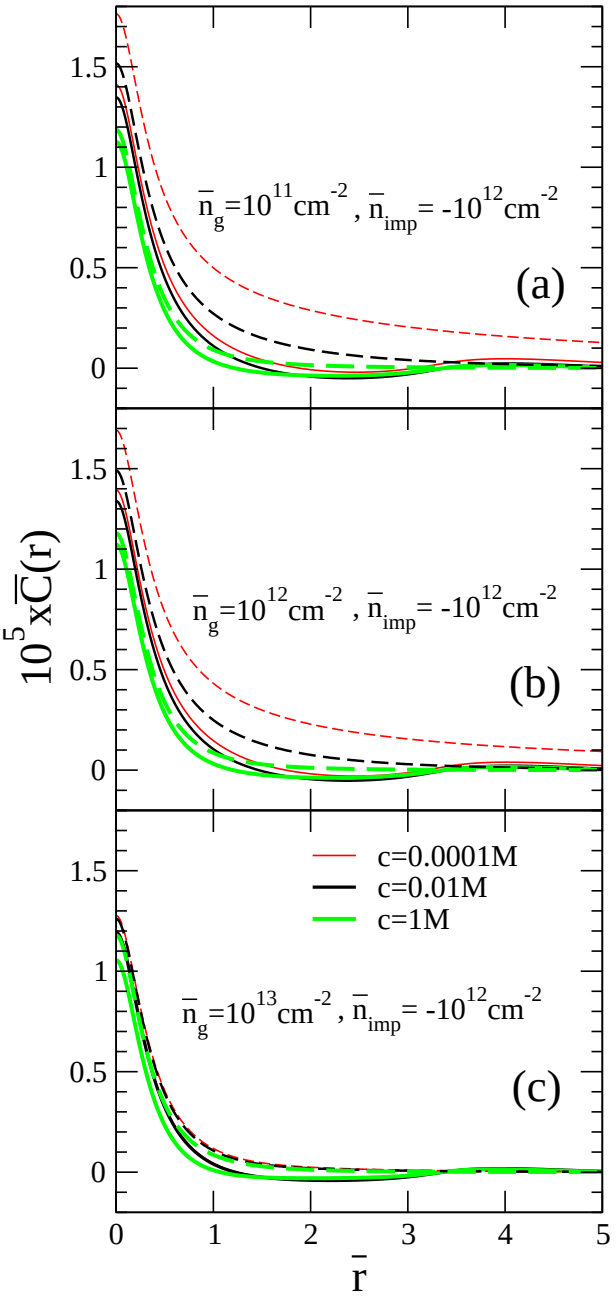

Figure 7.9: Reduced auto-correlation function of the potential in the plane of graphene, $\bar{C}(\bar{r}) = C(\bar{r})\, d^2/e^2$, shown as a function of the reduced distance $\bar{r} = rq_0$, where $q_0^{-1} = 2.1$ nm, due to an ensemble of (negatively charged) impurities at the depth $d = 2$ Å with the effective surface density $\bar{n}_{\rm imp} = -10^{12}$ cm^{-2}, for several values of the average charge density in graphene: (a) $\bar{n}_g = 10^{11}$ cm^{-2}, (b) $\bar{n}_g = 10^{12}$ cm^{-2}, and (c) $\bar{n}_g = 10^{13}$ cm^{-2}, and for several ion concentrations in the electrolyte: $c = 10^{-4}$ M (thin red lines), $c = 10^{-2}$ M (medium black lines), and $c = 1$ M (thick green lines). Dashed lines show the results for uncorrelated impurities and the solid lines show the results for the hard-disc model with correlation length $r_c = 7$ nm.

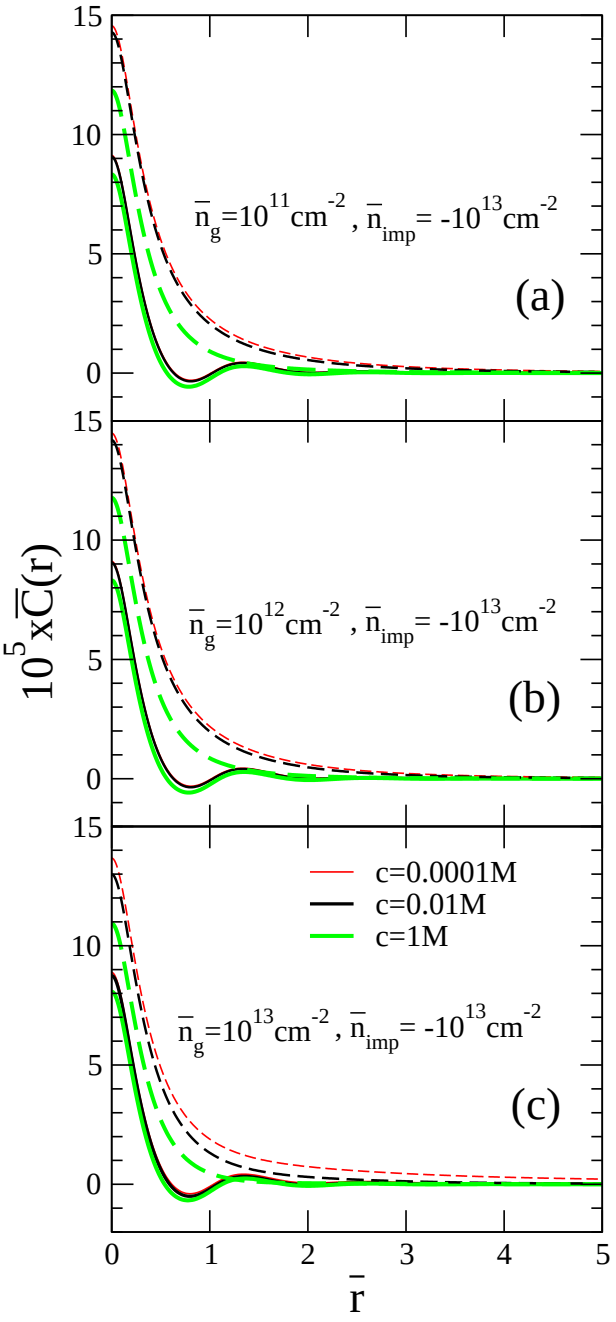

Figure 7.10: Reduced auto-correlation function of the potential in the plane of graphene, $\bar{C}(\bar{r}) = C(\bar{r})\, d^2/e^2$, shown as a function of the reduced distance $\bar{r} = rq_0$, where $q_0^{-1} = 2.1$ nm, due to an ensemble of (negatively charged) impurities at the depth $d = 2$ Å with the effective surface density $\bar{n}_{\rm imp} = -10^{13}$ cm^{-2}, for several values of the average charge density in graphene: (a) $\bar{n}_g = 10^{11}$ cm^{-2}, (b) $\bar{n}_g = 10^{12}$ cm^{-2}, and (c) $\bar{n}_g = 10^{13}$ cm^{-2}, and for several ion concentrations in the electrolyte: $c = 10^{-4}$ M (thin red lines), $c = 10^{-2}$ M (medium black lines), and $c = 1$ M (thick green lines). Dashed lines show the results for uncorrelated impurities and the solid lines show the results for the hard-disc model with correlation length $r_c = 2.2$ nm.

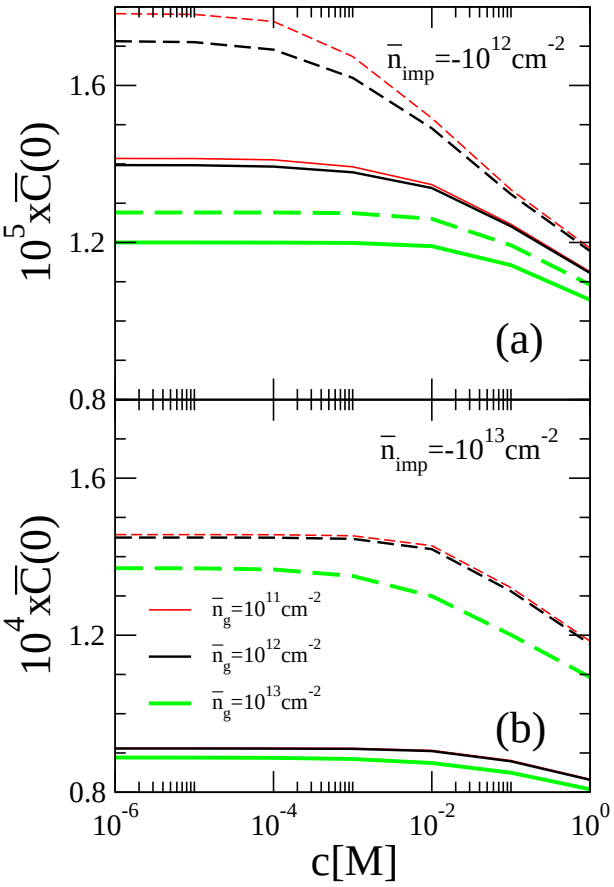

Figure 7.11: Reduced variance of the potential in the plane of graphene, $\bar{C}(0) = C(0)\, d^2/e^2$, shown as a function of the ion concentration in the electrolyte c in units of M (mol/litre) for several values of the average charge density in graphene: $\bar{n}_g = 10^{11}$ cm^{-2} (thin red lines), $\bar{n} = 10^{12}$ cm^{-2} (medium black lines), and $\bar{n} = 10^{13}$ cm^{-2} *thick green lines). Results for the uncorrelated impurities (dashed lines) are compared with those from the hard disc model (solid lines) for two ensembles of (negatively charged) impurities at depth $d = 2$ Å with the effective surface densities: $\bar{n}_{\rm imp} = -10^{12}$ cm^{-2} with correlation length $r_c = 7$ nm (panel a), and $\bar{n}_{\rm imp} = -10^{13}$ cm^{-2} with correlation length $r_c = 2.2$ nm (panel b).

that various cases could be covered, according to Figs. 7.3 and 7.4, including zero charge density in the diffuse layer, as well as (almost) neutral graphene with the low charge density of $\bar{n}_g = 10^{11}$ cm^{-2}. In addition, the largest values for those parameters are commensurate with those observed in experiments [37, 89, 90].

7.3 Concluding remarks

Our main emphasis in this chapter was to develop a model for ion screening in the electrolyte based on a partially linearized Poisson-Boltzmann (PLPB) equation and assess its advantages compared to the Debye-Hückel approximation for the Poisson-Boltzmann (DHPB) equation. As a secondary goal, we have introduced a hard-disc model for spatial correlation between charged impurities lying in a plane at a depth d inside the oxide, which is applicable to much higher packing fractions than the simple step correlation model of the previous chapter.

One of the main advantages in using the PLPB model instead of the DHPB model is its capacity to describe the equilibrium doping of graphene by an application of a high potential at the top gate in the electrolyte. This is achieved by solving a fully non-linear, one-dimensional PB equation for the surface average of the potential in the electrolyte, and connecting it with the nonlinear expression for the equilibrium charge carrier density in graphene. We have obtained a set of equations for the entire structure, including the Stern layer, which may be used to determine the doping potential in graphene and the potential drop in the diffuse electrolyte for any given combination of both the top gate and the back gate potentials, in the presence of an arbitrary density of charged impurities in the oxide, and for arbitrary ion concentration in the electrolyte. It was found that the equations based on the DH approximation yield reliable results for the average potentials only in a relatively narrow range of the top gate potential giving nearly vanishing potential drop in the diffuse layer. Results from the DH approximation were found equally poor for the doping potential in graphene. (In this work we only consider electrolytically gated graphene and assume that the average electric field in the oxide is zero.)

From the doping potential in graphene it is straightforward to determine both the average charge carrier density in graphene and the corresponding polarization function of graphene that determines its ability to screen fluctuations of the potential in the plane of graphene that arise from the randomness in the positions of charged impurities. In addition, from the potential drop in the diffuse layer, it is possible to determine the effective surface charge density in that layer due to polarization of the mobile ions. This density, which compensates the algebraic sum of the effective surface density of charged impurities in the oxide and the equilibrium charge density in graphene via the charge neutrality relation is an important parameter that defines the screening ability of the mobile ions in the electrolyte.

Further comparisons between the DHPB and PLPB models were conducted by studying the screened potential due to single point charge in the absence of other impurities and the auto-correlation of the fluctuating potential due to ensemble of uncorrelated charged impurities. Those two quantities were found to exhibit similar properties. We have seen that, generally, growing differences between the two models arise with decreasing ion concentration and increasing effective charge density in the diffuse layer. The latter effect may be traced to the large potential drops in the diffuse layer, which are poorly described in the DH approximation. Conversely, we have seen that there are practically no differences in the results for the screened potential and auto-correlation function at the highest ions

concentration of 1 mole/litre studied here.

Another important difference between the results from the two models for the screened potential and the auto-correlation function is weaker dependence on the ion concentration in the PLPB model as compared to the DHPB model. This suppression of the dependence on ion concentration is further reinforced by introducing correlation effects in the auto-correlation function by using the hard disc model for the positions of charged impurities in conjunction with the PLPB model. We have seen that the curves describing this function for correlated impurities are closely packed in a manner that is rather independent from the charge density in the diffuse layer. This is further evidenced in the plots of variance of the fluctuating potential, where curves for correlated impurities show very weak dependence on the ion concentration, especially at the higher density of charged impurities studied, and they show more clustering for different values of the charge density in graphene.

Chapter 8

Summary and outlook

In this thesis we have studied several aspects of the interaction of graphene with a nearby electrolyte containing mobile ions in the configuration of a field effect transistor (FET). We considered a layered structure with large area, which consists of a metallic back gate, an oxide layer of finite thickness, a single sheet of graphene of zero thickness, and a semi-infinite layer of electrolyte, separated from graphene by a Stern layer of finite thickness. The presence of a top gate defines the value of the electrostatic potential deep in the bulk of the electrolyte.

Our first goal was to analyze the doping of graphene by applying external potential to the gate(s) in the presence of a given concentration of mobile ions, as well as a given density of fixed charged impurities in the oxide. For the equilibrium surface density of charge carriers in graphene we have used a full density of states for its π electron bands obtained from the Tight Binding approximation. On the other hand, the solvent was described as a dielectric continuum, whereas the distribution of dissolved ions in thermal equilibrium was described by a Boltzmann distribution and its generalizations. The electrostatic potential throughout the structure was found by solving the Poisson's equation subject to the usual electrostatic conditions at the planar boundaries between different layers.

Since the graphene based FETs often operate in the regime of a high doping density, we have adopted two modifications of the Poisson-Boltzmann (PB) model in the electrolyte, which deal with two important effects that may arise from a large potential drop in the electrolyte and large ion concentration. The effect due to finite size of the hydrated ions in the electrolyte was described by the Bikerman model, which replaces the Boltzmann distribution with a Fermi-like distribution of ions and thus regulates the ion crowding near a highly charged surface of graphene. The effect of dielectric saturation of the solvent due to the dipole orientational ordering of its molecules was described by the Booth model, which expresses a decrease of the dielectric constant of the solvent in the presence of an increasing electric field that may arise close to the charged surface of graphene.

Those modifications of the PB model were used to calculate the total capacitance of a graphene-electrolyte interface, where we neglected the Stern layer, for a broad range of

values for the potential applied to the top gate under equilibrium conditions. We have found that for the gate potentials $\lesssim 1$ V, which are of interest in most graphene applications, the total capacitance is dominated by the quantum capacitance of graphene, for which it suffices to use the linear approximation for the density of states for its π electron bands that follows from the Dirac cone approximation of those bands. Moreover, we have found that the capacitance of the electric double layer in the electrolyte may be adequately described for the same range of gate potentials $\lesssim 1$ V by using the PB model in its standard, nonlinear form, without the need of additional modifications. We have also shown that changing the ion concentration exerts only relatively weak effects on the capacitance, as well as that the most of the potential applied through the electrolyte goes to doping the graphene for concentrations.

Our next goal was to study the screening properties of doped graphene in the presence of mobile ions in the electrolyte for a range of the gate potentials of interest for sensing applications. Analytical progress in that direction was possible based on the use of the standard PB model without the need for the Bikerman or Booth modifications. However, we retained the Stern layer in the structure as a simple means to phenomenologically amend the PB model without impeding its tractability, or to possibly represent a thin layer of an insulating oxide, which is sometimes used with conventional silicon-based FETs in contact with electrolyte.

The screening of the electrostatic potential was formulated mathematically in terms of an effective dielectric function, which was deduced by using the Green's function (GF) to express a solution of the Poisson equation throughout the entire structure. As a result of employing the Dyson-Schwinger equation to obtain the GF for the structure with graphene in term of the GF for the same structure without graphene, the resulting dielectric function consists of two terms: one that pertains to the electrolyte with the surrounding solid dielectrics, and the other that is given by the polarization function of graphene. We have used a result for the polarization function of doped graphene obtained by the method of random phase approximation for its π electron bands in the Dirac cone approximation. That function depends on the equilibrium doping density of graphene at finite temperature.

On the other hand, two approximations were considered for the PB model in the electrolyte: one in which the Boltzmann distribution of ions is fully linearized from the outset, also known as the Debye-Hückel (DH) approximation for the PB (DHPB) model, and the other where a linearization was performed only for the fluctuating part of the potential about an average value that is obtained from a solution of the standard nonlinear PB model in one dimension for the surface average of the potential. The latter approximation is called partially linearized PB (PLPB) model.

A comparison between those two models was first performed by calculating the surface averaged potential in the entire structure and the equilibrium doping charge density in graphene for a range of values of the external parameters: the gate potential(s), the ion concentration in the electrolyte and the average density of charged impurities in the oxide. It was shown that the averaged potential and the graphene doping density are reliably obtained from the DHPB model only when the potential drop across the diffuse layer in

the electrolyte is small and/or when the ion concentration is large. On the other hand, the PLPB model yields the doping density of graphene and the potential drop across the diffuse layer (which determines the surface density of the accumulated charge in that layer), with better accuracy and in a broader range of values of the external parameters than the DHPB model. This consistency with the external parameters is the main advantage of the PLPB model because the equilibrium doping density of graphene enters its polarization function, whereas the surface density of the accumulated charge in the diffuse layer enters that part of the dielectric function which pertains to the electrolyte. It was shown that, by choosing suitable combinations of the external parameters, it is possible to change the relative roles of graphene and mobile ions in the screening process by either rendering graphene neutral or by making the charge density in the diffuse layer vanish.

In the following step, we have used both the DHPB and the PLPB models to calculate the screened electrostatic potential in the plane of graphene due to single charged impurity in the oxide, as well as the auto-covariance of fluctuations in the potential that arise from an ensemble of uncorrelated charged impurities with random positions in a plane parallel to graphene. Both models showed an increased screening at large distances with increasing ion concentration. However, the degree of variation in screening with changing ion concentration was reduced in the PLPB model in comparison to the DHPB model for larger values of the charge density in the diffuse layer. This shows that the ion concentration alone is not a sufficient parameter to determine the role of the mobile ions in the screening of charged impurities, but rather all of the external parameters that enter the GF in the PLPB model are needed to make a contact with the full information on the equilibrium gating conditions.

Finally, we have also explored the effect of spatial correlation among the charged impurities on both the auto-correlation and variance of the fluctuations in the potential in the plane of graphene by means of the geometric structure factor for the impurities exhibiting a step-like correlation and a hard disc type of spatial correlation. Such an analysis of the statistical properties of charged impurities is important for determining the electrical resistivity of graphene due to Coulomb scattering of its charge carriers on the fluctuating electrostatic potential. We have found that both the DHPB and the PLPB models exhibit a very weak dependence on ion concentration for both the auto-correlation and variance of the potential when compared to the uncorrelated charged impurities. This may be related to the fact that variation in the ion concentration mostly affects the screening at large distances, whereas spatial correlation among the impurities may give rise to a destructive interference in the fluctuations of the potential at such distances.

There are many possible directions that may be taken in future work in order to further improve the models presented in this thesis. One of the most obvious and straightforward extensions of our model would be to introduce the effects of possible ion adsorption at the boundary between the diffuse layer and the Stern layer by using suitable models for the equilibrium chemical reactions. Similarly, driven by the current interest in the sensitivity of graphene to the pH in the nearby solution, one can amend our model of the electrolyte by introducing the redox processes taking place at the graphene surface.

As regards the solvents used in the electrolyte, many current experiments with graphene employ ionic liquids or ion gels, which could be introduced in our model by amending the PB equation, albeit at the expense of its analytical tractability.

One of the main advantages of our model lies in the use of the GF, which expresses the fluctuation in the electrostatic potential in terms of the fluctuations in the external charge density. Our main focus here was to study the effects of random positions of the charged impurities in the oxide. The compact expressions obtained from the GF for the fluctuating potential will be used in future to compute the conductivity of electrolytically top gated graphene in the presence of charged impurities.

However, in the next step we could assume that there also exists a charged biological structure in the electrolyte close to graphene that may be represented by a laterally uniform charged layer, or a membrane parallel to graphene such as lipid layer, plus a fluctuating charge distribution in that layer that may be described by a structure factor. Then it would be worthwhile attempting to solve the one-dimensional nonlinear PB model for the average potential in such a structure to establish the new gating conditions for graphene in the presence of a membrane, with a possibility to amend our GF formulation of the problem by considering small fluctuations in the potential due to a structured distribution of charges within the membrane.

APPENDICES

Appendix A

Derivation of $\bar{M}^{l,l'}_{\mathbf{k},\mathbf{k+q}}$

The matrix $\bar{M}^{l,l'}_{\mathbf{k},\mathbf{k+q}}$ is given by the integral,

$$\begin{aligned}\bar{M}^{l,l'}_{\mathbf{k},\mathbf{k+q}} &= \iint d^2\mathbf{r} \int dz \psi^*_{\mathbf{k},l}(\mathbf{r},z) e^{-i\mathbf{q}\cdot\mathbf{r}} \psi_{\mathbf{k+q},l'}(\mathbf{r},z) \\ &= \iint d^2\mathbf{r} \int dz [a^*_{\mathbf{k},l}\psi^*_{A,\mathbf{k}} + b^*_{\mathbf{k},l}\psi^*_{B,\mathbf{k}}] e^{-i\mathbf{q}\cdot\mathbf{r}} [a_{\mathbf{k+q},l'}\psi_{A,\mathbf{k+q}} + b_{\mathbf{k+q},l}\psi_{B,\mathbf{k+q}}]. \qquad \text{(A.1)}\end{aligned}$$

We may express the terms $\psi_{A,\mathbf{k}}$ and $\psi_{B,\mathbf{k}}$ as a sum over the p_z orbitals via utilizing Eq. (2.11). Taking into account the individual terms without their coefficients and expanding the integral with reference to the p_z orbitals we get,

$$\begin{aligned}(\bar{M}^{l,l'}_{\mathbf{k},\mathbf{k+q}})^{i,j} &= \iint d^2\mathbf{r} \int dz \psi^*_{i,\mathbf{k}} e^{-i\mathbf{q}\cdot\mathbf{r}} \psi_{j,\mathbf{k}} \\ &= \frac{1}{N} \sum_{\mathbf{R}} \sum_{\mathbf{R}'} e^{i(\mathbf{k+q})\cdot(\mathbf{R}+\mathbf{t}_i) - i\mathbf{k}\cdot(\mathbf{R}'+\mathbf{t}_j)} \qquad \text{(A.2)} \\ &\times \iint d^2\mathbf{r} \int dz \Upsilon^*_{p_z}(\mathbf{r}-\mathbf{R}'-\mathbf{t}_j,z) e^{-i\mathbf{q}\cdot\mathbf{r}} \Upsilon_{p_z}(\mathbf{r}-\mathbf{R}-\mathbf{t}_i,z). \qquad \text{(A.3)}\end{aligned}$$

Here indices (i and j) correspond to either position A or position B atoms in the sub-lattice, respectively, $\mathbf{t}_i$ are the nearest neighbour vectors and $\mathbf{R}$ are the Bravias lattice vectors. As the overlap integral between p_z orbitals on different Bravais lattice sites (i.e. $\mathbf{R} \neq \mathbf{R}'$) will be negligible, we will ignore them. Hence, our integral reduces to

$$\begin{aligned}(\bar{M}^{l,l'}_{\mathbf{k},\mathbf{k+q}})^{i,j} &= \frac{1}{N} \sum_{\mathbf{R}} e^{i(\mathbf{k+q})\cdot(\mathbf{t}_i-\mathbf{t}_j)+i\mathbf{q}\cdot\mathbf{t}_j} \iint d^2\mathbf{r} \int dz \qquad \text{(A.4)} \\ &\times \Upsilon^*_{p_z}(\mathbf{r}-\mathbf{R}-\mathbf{t}_j,z) e^{-i\mathbf{q}\cdot(\mathbf{r}-\mathbf{R})} \Upsilon_{p_z}(\mathbf{r}-\mathbf{R}-\mathbf{t}_i,z) \\ &= \sum_{\alpha} e^{i(\mathbf{k+q})\cdot\mathbf{w}_\alpha} \iint d^2\mathbf{r} \int dz \Upsilon^*_{p_z}(\mathbf{r},z) e^{-i\mathbf{q}\cdot\mathbf{r}} \Upsilon_{p_z}(\mathbf{r}-\mathbf{w}_i,z), \qquad \text{(A.5)}\end{aligned}$$

where we define $\mathbf{w}_\alpha = \mathbf{t}_i - \mathbf{t}_j$ to be a difference between nearest neighbour positions within the unit cell. Once again, assuming that the nearest neighbour overlap integral is negligible, we are left with

$$(\bar{M}^{l,l'}_{\mathbf{k},\mathbf{k}+\mathbf{q}})^{i,i} = \iint d^2\mathbf{r} \int dz |\Upsilon_{p_z}(\mathbf{r},z)|^2 e^{-i\mathbf{q}\cdot\mathbf{r}}. \tag{A.6}$$

Using the hydrogen like wavefunctions for the p_z orbital, we obtain,

$$(\bar{M}^{l,l'}_{\mathbf{k},\mathbf{k}+\mathbf{q}})^{A,A} = (\bar{M}^{l,l'}_{\mathbf{k},\mathbf{k}+\mathbf{q}})^{B,B} = \left[1 + \left(\frac{a_0 q}{Z_{eff}}\right)^2\right]^{-3}, \tag{A.7}$$

where a_0 is the Bohr radius and Z_{eff} is the effective charge of the nucleus of the carbon atom. Now to include the coefficients in our analysis, we recall that the coefficients for sublattice sites A and B are $a_{\mathbf{k},l} = 1$ and $b_{\mathbf{k},l} = \dfrac{f(\mathbf{k})}{|f(\mathbf{k})|}$ respectively. So the final equation for the matrix is

$$\bar{M}^{l,l'}_{\mathbf{k},\mathbf{k}+\mathbf{q}} = \left[1 + \left(\frac{a_0 q}{Z_{eff}}\right)^2\right]^{-3} \left[1 + \frac{f(\mathbf{k}) f(\mathbf{k}+\mathbf{q})}{|f(\mathbf{k})||f(\mathbf{k}+\mathbf{q})|}\right]. \tag{A.8}$$

Appendix B

Static polarizability of graphene

We follow here the derivation of static polarization function, given in Ref. [71] in the approximation of linear energy dispersion, $\varepsilon_{l\mathbf{k}} = (-1)^l \hbar v_F |\mathbf{k}|$, where $\mathbf{k}$ is a small displacement wavenumber from either of the two Dirac points in the first Brillouin zone.

$$\chi(\mathbf{q}) = -\frac{g_d}{L^2} \sum_{l,l',\mathbf{k}} (f_{l\mathbf{k}} - f_{l'\mathbf{k}+\mathbf{q}}) \frac{|\langle \mathbf{F}_{l\mathbf{k}}^\dagger | \mathbf{F}_{l'\mathbf{k}+\mathbf{q}} \rangle|^2}{\varepsilon_{l\mathbf{k}} - \varepsilon_{l'\mathbf{k}+\mathbf{q}}} \tag{B.1}$$

where $A \equiv L^2$ is the (large) normalization area of graphene, $f_{l\mathbf{k}} \equiv f(\varepsilon_{l\mathbf{k}})$ is the Fermi-Dirac distribution, and $g_d = 4$ is the degeneracy factor that takes into account both the spin and the valley degeneracy in graphene π-bands (corresponding to the two Dirac points). In the notation of Ref. [71], we have $|\bar{M}^{l,l'}_{\mathbf{k},\mathbf{k}'}|^2 \equiv |\langle \mathbf{F}_{l\mathbf{k}}^\dagger | \mathbf{F}_{l'\mathbf{k}+\mathbf{q}} \rangle|^2$ with

$$\begin{aligned} |\langle \mathbf{F}_{l\mathbf{k}}^\dagger | \mathbf{F}_{l'\mathbf{k}+\mathbf{q}} \rangle|^2 &= \frac{1}{4} \left\{ 1 + (ll')^2 + (ll') \left[e^{i(\theta'_k - \theta_k)} + e^{-i(\theta'_k - \theta_k)} \right] \right\} \\ &= (1 + ll' \cos\theta_{kk'})/2, \end{aligned} \tag{B.2}$$

where $\cos\theta_{kk'} \equiv \cos(\theta_{k'} - \theta_k)$ is the angle between the vectors $\mathbf{k}$ and $\mathbf{k}' \equiv \mathbf{k} + \mathbf{q}$.

It is convenient to define $\chi^0(\mathbf{q})$ as

$$\chi^0(\mathbf{q}) = -\frac{g_d}{L^2} \sum_{l,l',\mathbf{k}} (f^0_{l\mathbf{k}} - f^0_{l'\mathbf{k}+\mathbf{q}}) \frac{|\langle \mathbf{F}_{l\mathbf{k}}^\dagger | \mathbf{F}_{l'\mathbf{k}+\mathbf{q}} \rangle|^2}{\varepsilon_{l\mathbf{k}} - \varepsilon_{l'\mathbf{k}+\mathbf{q}}}, \tag{B.3}$$

where

$$f^0_{l\mathbf{k}} = \begin{cases} 1 & \text{if } l = -1, \\ 0 & \text{if } l = +1. \end{cases} \tag{B.4}$$

Defining

$$\tilde{f}_{l\mathbf{k}} = f_{l\mathbf{k}} - f^0_{l\mathbf{k}} \tag{B.5}$$

if the Fermi level lies in the conduction band, the polarization function may be written as

$$\chi(\mathbf{q}) = -\frac{g_d}{L^2}\sum_{l,l',\mathbf{k}}(\tilde{f}_{l\mathbf{k}} - \tilde{f}_{l'\mathbf{k}+\mathbf{q}})\frac{|\langle \mathbf{F}^{\dagger}_{l\mathbf{k}}|\mathbf{F}_{l'\mathbf{k}+\mathbf{q}}\rangle|^2}{\varepsilon_{l\mathbf{k}} - \varepsilon_{l'\mathbf{k}+\mathbf{q}}}, \tag{B.6}$$

Performing the summation over l, l', the polarization function becomes

$$\chi(q) = -\frac{g_d}{2L^2}\sum_{\mathbf{k}}\left\{\frac{[\tilde{f}_{\mathbf{k}+} - \tilde{f}_{\mathbf{k}'+}](1+\cos\theta_{kk'})}{\varepsilon_{\mathbf{k}} - \varepsilon_{\mathbf{k}'}} + \frac{[\tilde{f}_{\mathbf{k}+} - \tilde{f}_{\mathbf{k}'+}](1-\cos\theta_{kk'})}{\varepsilon_{\mathbf{k}} + \varepsilon_{\mathbf{k}'}}\right. \tag{B.7}$$

$$\left. - \frac{[\tilde{f}_{\mathbf{k}-} - \tilde{f}_{\mathbf{k}'-}](1-\cos\theta_{kk'})}{\varepsilon_{\mathbf{k}} + \varepsilon_{\mathbf{k}'}} - \frac{[\tilde{f}_{\mathbf{k}-} - \tilde{f}_{\mathbf{k}'-}](1+\cos\theta_{kk'})}{\varepsilon_{\mathbf{k}} - \varepsilon_{\mathbf{k}'}}\right\} \tag{B.8}$$

Redistributing the terms, we may write the polarization function as

$$\chi(q) = \chi^{+}(q) + \chi^{-}(q) \tag{B.9}$$

where

$$\chi^{+}(q) = -\frac{g_d}{2L^2}\sum_{\mathbf{k}}\left[\frac{[\tilde{f}_{\mathbf{k}+} - \tilde{f}_{\mathbf{k}'+}](1+\cos\theta_{kk'})}{\varepsilon_{\mathbf{k}} - \varepsilon_{\mathbf{k}'}} + \frac{[\tilde{f}_{\mathbf{k}+} - \tilde{f}_{\mathbf{k}'+}](1-\cos\theta_{kk'})}{\varepsilon_{\mathbf{k}} + \varepsilon_{\mathbf{k}'}}\right] \tag{B.10}$$

$$\chi^{-}(q) = +\frac{g_d}{2L^2}\sum_{\mathbf{k}}\left[\frac{[\tilde{f}_{\mathbf{k}-} - \tilde{f}_{\mathbf{k}'-}](1-\cos\theta_{kk'})}{\varepsilon_{\mathbf{k}} + \varepsilon_{\mathbf{k}'}} + \frac{[\tilde{f}_{\mathbf{k}-} - \tilde{f}_{\mathbf{k}'-}](1+\cos\theta_{kk'})}{\varepsilon_{\mathbf{k}} - \varepsilon_{\mathbf{k}'}}\right]. \tag{B.11}$$

Here $\mathbf{k}' \equiv \mathbf{k} + \mathbf{q}$ and we have utilized the linear expression of the energy spectrum, $\varepsilon_{\mathbf{k}\pm} = \pm\hbar v_F|\mathbf{k}|$. In the limit of a large system, that is of closely-spread k-values, we may replace the summation with an integral as

$$\frac{1}{L^2}\sum_{\mathbf{k}} \to \frac{1}{(2\pi)^2}\int d\mathbf{k} \tag{B.12}$$

As the integrand involving the terms of $\tilde{f}_{\mathbf{k}'\pm}$ is symmetrical, we may change the variable $\mathbf{k} \to \mathbf{k} + \mathbf{q}$ to express the polarization function terms as

$$\begin{aligned}\chi^{+}(q) &= -\frac{g_d}{(2\pi)^2}\int d\mathbf{k}\left[\frac{\tilde{f}_{\mathbf{k}+}(1+\cos\theta_{kk'})}{\varepsilon_{\mathbf{k}} - \varepsilon_{\mathbf{k}'}} + \frac{\tilde{f}_{\mathbf{k}+}(1-\cos\theta_{kk'})}{\varepsilon_{\mathbf{k}} + \varepsilon_{\mathbf{k}'}}\right] \\ &= -\frac{2g_d}{(2\pi)^2}\int d\mathbf{k}\left[\frac{\tilde{f}_{\mathbf{k}+}(\varepsilon_{\mathbf{k}} + \varepsilon_{\mathbf{k}'}\cos\theta_{kk'})}{\varepsilon_{\mathbf{k}}^2 - \varepsilon_{\mathbf{k}'}^2}\right],\end{aligned} \tag{B.13}$$

$$\begin{aligned}\chi^{-}(q) &= +\frac{g_d}{(2\pi)^2}\int d\mathbf{k}\left[\frac{\tilde{f}_{\mathbf{k}-}(1+\cos\theta_{kk'})}{\varepsilon_{\mathbf{k}} - \varepsilon_{\mathbf{k}'}} + \frac{\tilde{f}_{\mathbf{k}-}(1-\cos\theta_{kk'})}{\varepsilon_{\mathbf{k}} + \varepsilon_{\mathbf{k}'}}\right] \\ &= +\frac{2g_d}{(2\pi)^2}\int d\mathbf{k}\left[\frac{\tilde{f}_{\mathbf{k}-}(\varepsilon_{\mathbf{k}} + \varepsilon_{\mathbf{k}'}\cos\theta_{kk'})}{\varepsilon_{\mathbf{k}}^2 - \varepsilon_{\mathbf{k}'}^2}\right],\end{aligned} \tag{B.14}$$

$\theta_{kk'}$ is the angle between the $\mathbf{k}$ and $\mathbf{k}+\mathbf{q}$ and it is related to angle between $\mathbf{k}$ and $\mathbf{q}$, and ϕ as

$$\mathbf{k}\cdot(\mathbf{k}+\mathbf{q}) = k|\mathbf{k}+\mathbf{q}|\cos\theta_{kk'} = k^2 + \mathbf{k}\cdot\mathbf{q} = k^2 + kq\cos\phi \tag{B.15}$$

and

$$\cos\theta_{kk'} = (k + q\cos\phi)/|\mathbf{k}+\mathbf{q}|. \tag{B.16}$$

Substituting the expression for $\cos\theta_{kk'}$ in the integrals, we obtain

$$\chi^+(q) = \frac{2g_d}{(2\pi)^2}\frac{1}{\hbar v_F q}\int dk d\phi\ k\frac{\tilde{f}_{\mathbf{k}+}(2k+q\cos\phi)}{q+2k\cos\phi} \tag{B.17}$$

and

$$\chi^-(q) = -\frac{2g_d}{(2\pi)^2}\frac{1}{\hbar v_F q}\int dk d\phi\ k\frac{\tilde{f}_{\mathbf{k}-}(2k+q\cos\phi)}{q+2k\cos\phi} \tag{B.18}$$

The angular integral is

$$\begin{aligned}
\int_0^{2\pi}\frac{2k+q\cos\phi}{q+2k\cos\phi}d\phi &= 2\int_0^{\pi}d\phi\frac{q}{2k} + 2\left(\frac{\Xi^2}{2k}\right)\int_0^{\pi}d\phi\frac{1}{q+2k\cos\phi} \\
&= \frac{\pi q}{k} + \frac{\Xi}{k}\left\{\begin{array}{ll} -2\tan^{-1}\left(\dfrac{\Xi\tan(\phi/2)}{q+2k}\right)\Big|_0^{\pi} & \text{if } q>2k \\ \ln\left(\dfrac{\Xi\tan(\phi/2)+q+2k}{\Xi\tan(\phi/2)-q-2k}\right)\Big|_0^{\pi} & \text{if } q<2k \end{array}\right\} \\
&= \frac{\pi q}{k} + \frac{\Xi}{k}\left\{\begin{array}{ll} -\pi & \text{if } q>2k \\ \text{non-physical answer} & \text{if } q<2k, \end{array}\right\}
\end{aligned} \tag{B.19}$$

where $\Xi = \sqrt{|4k^2-q^2|}$. Therefore, doing the angular integral, we obtain

$$\chi^+(q) = \frac{2g_d}{(2\pi)^2}\frac{\pi}{\hbar v_F}\left\{\int_0^{\infty}dk\tilde{f}_{\mathbf{k}+} - \int_0^{q/2}dk\tilde{f}_{\mathbf{k}+}\sqrt{1-(2k/q)^2}\right\}, \tag{B.20}$$

and

$$\chi^-(q) = \frac{2g_d}{(2\pi)^2}\frac{\pi}{\hbar v_F}\left\{\int_0^{\infty}dk\tilde{f}_{\mathbf{k}-} - \int_0^{q/2}dk\tilde{f}_{\mathbf{k}-}\sqrt{1-(2k/q)^2}\right\}, \tag{B.21}$$

Considering the first integral in each expression, we have

$$\chi^+(q) = \frac{g_d}{\pi\beta(\hbar v_F)^2}\left[\frac{1}{2}\ln[2\cosh(\beta\mu/2)] - \frac{q}{2q_t}\int_0^1 du\frac{\sqrt{1-u^2}}{1+e^{uq/q_t-\beta\mu}}\right] \tag{B.22}$$

and

$$\chi^{-}(q) = \frac{g_d}{\pi\beta(\hbar v_F)^2}\left[\frac{1}{2}\ln[2\cosh(\beta\mu/2)] + \frac{\pi q}{8q_t} - \frac{q}{2q_t}\int_0^1 du \frac{\sqrt{1-u^2}}{1+e^{uq/q_t+\beta\mu}}\right] \tag{B.23}$$

where we have defined a thermal inverse screening length by $q_t = 2/(\beta\hbar v_F)$. The total polarization function is

$$\chi(q) = \frac{g_d}{\pi\beta(\hbar v_F)^2}\left[\ln[2\cosh(\beta\mu/2)] + \frac{\pi q}{8q_t} - \frac{q}{2q_t}\int_0^1 du\sqrt{1-u^2}\left(\frac{1}{1+e^{uq/q_t-\beta\mu}} + \frac{1}{1+e^{uq/q_t+\beta\mu}}\right)\right] \tag{B.24}$$

Note that μ, which is used in Eq. (B.24), may be obtained from Eq. (2.39) for any given temperature and equilibrium charge carrier density n. This is the main result for the polarization function of graphene in RPA, which is used throughout this thesis. It may be noticed that, in the limit $q \ll k_F$, we have that $\chi(q) \equiv \chi(q) \to \chi_{TF}$, given in Eq. (3.4), which is independent of q.

However, when $q \geq k_F$, important differences arise between the RPA polarization function and its TF limit χ_{TF}. Those differences are best seen in the zero temperature limit when $\mu \to \varepsilon_F$, where $\varepsilon_F = \hbar v_F k_F \text{sign}(n)$ is the Fermi energy with $k_F = \sqrt{\pi|n|}$ being the Fermi momentum in graphene with the equilibrium charge carrier density n. In that limit, one obtains

$$\chi^{+}(q) = \frac{g_d k_F}{2\pi\hbar v_F}\begin{cases} 1 - \dfrac{q}{8k_F} & \text{if } q \leq 2k_F \\ 1 - \dfrac{1}{2}\sqrt{1-\dfrac{4k_F^2}{q^2}} - \dfrac{q}{4k_F}\sin^{-1}\left[\dfrac{2k_F}{q}\right] & \text{if } q \geq 2k_F, \end{cases} \tag{B.25}$$

and

$$\chi^{-}(q) = \frac{g_d q}{16\pi\hbar v_F} \tag{B.26}$$

Hence

$$\chi(q) = \frac{g_d k_F}{2\pi\hbar v_F}\left(1 + \left\{\frac{q}{4k_F}\cos^{-1}\left[\frac{2k_F}{q}\right] - \frac{1}{2}\sqrt{1-\left[\frac{2k_F}{q}\right]^2}\right\}H(q-2k_F)\right), \tag{B.27}$$

where H is the Heaviside step function. Unlike the linear Thomas-Fermi case, we see that $\chi_{RPA}(q) = q/(4\hbar v_F)$ in intrinsic graphene at zero temperature. Since this is also the short wavelength limit of $\chi_{RPA}(q)$ when $n \neq 0$, one may assert that the RPA results will provide a more efficient screening of external charges at short distances. However, it can be seen Eq. (B.27) that the RPA polarization function is not continuously differentiable at $q = 2k_F$. This gives rise the the so-called Friedel oscillations in the screened potential at large distance, which are the consequences of quantum nature of the RPA polarization function [70].

Appendix C

Effect of mobile ions on Dirac plasmons in graphene

Even though we are focused in this thesis on the static polarization of graphene, it is interesting to mention that, for doped graphene we may easily estimate the effect of ion concentration on the dispersion of low-frequency, collective oscillations of charge carriers in graphene, also known as the Dirac plasmon, or sheet plasmon. A simple estimate of the plasmon frequency $\omega_{\rm p}$ in graphene at frequencies $\omega > qv_{\rm F}$ is found from the expression for the polarization function within the kinetic model [97],

$$\chi(q,\omega) = \frac{q_{\rm TF}}{2\pi e^2}\left\{1 - \left[1 - \left(\frac{qv_{\rm F}}{\omega}\right)^2\right]^{-1/2}\right\}, \tag{C.1}$$

giving from Eq. (6.41)

$$\omega_{\rm p}(q) = v_{\rm F}\left[q + \frac{q_{\rm TF}}{\epsilon_{\rm bg}(q)}\right]\sqrt{\frac{q}{q + 2\frac{q_{\rm TF}}{\epsilon_{\rm bg}(q)}}}. \tag{C.2}$$

Thus, in the absence of mobile ions in the electrolyte, $c = 0$, we obtain in the long wavelength limit

$$\omega_{\rm p}(q) \sim v_{\rm F}\sqrt{\frac{q_{\rm TF}q}{\epsilon_1 + \epsilon_3}}, \tag{C.3}$$

which is a typical $\omega_{\rm p} \propto \sqrt{q}$ plasmon dispersion for a 2D electron gas, such as doped graphene [1, 39].

However, for even very small values of c, one can show from Eq. (6.42) that, in the long wavelength limit,

$$\epsilon_{\rm bg}(q) \to \frac{2\pi}{q}C_{\rm dl}, \tag{C.4}$$

where the capacitance of the double layer $C_{\rm dl}$ is defined in Eqs. (6.26), (6.27), and (6.28). Then from Eq. (C.2) it follows that the Dirac plasmon in graphene exhibits a quasi-acoustic form of the long wavelength dispersion,

$$\omega_{\rm p}(q) \sim v_{\rm F} q \frac{\left(1+\frac{C_{\rm q}}{C_{\rm dl}}\right)}{\sqrt{1+2\frac{C_{\rm q}}{C_{\rm dl}}}}, \tag{C.5}$$

where quantum capacitance of graphene is defined in Eq. (6.17). A similar effect of the salt on plasmons was found in a work conducted for carbon nanotubes [98]. Without further pursuing this effect, we note that such an extreme sensitivity of plasmon dispersion to the presence of mobile ions may be used for sensing applications of graphene within the area of Nano-plasmonics [99].

Appendix D

Geometric structure models for charged impurities

We discuss here models used in this thesis for the pair correlation (or radial distribution) function $g(r)$ in a two-dimensional (2D) distribution of charged impurities lying in a plane embedded into the substrate underneath electrolytically gated graphene sheet. In addition to uncorrelated impurities with $g(r) = 1$, we consider two models that contain a single parameter r_c characterizing the inter-particle correlation distance: a step-correlation (SC) model with $g(r) = H(r - r_c)$, where H is the Heaviside unit step function, which was often used in previous studies of charged impurities in graphene [95, 94], and the model of hard discs (HD), in which particles interact with each other as impenetrable disks of the diameter r_c [100].

There are several advantages to using the HD model over the SC model to evaluate the the 2D structure factor $I(q)$ in Eq. (6.53). First, the former model is based on a Hamiltonian equation for the thermodynamic state of a 2D fluid with a well-defined pair potential between impurities, whereas the latter model is an *ad hoc* description of the impurity distribution, made-up for simple, analytic results. That is not to say that the SC model is poor at capturing the interesting effects due to correlated impurities [95, 94]. It is well known that the long wavelength limit of the 2D structure factor, $I(0)$, is related to the isothermal compressibility of a 2D fluid [101], which may be expressed as a function of the packing fraction defined by $p = \pi n_{\text{imp}} r_c^2/4$. Thus, p is a key measure of performance of the two models. It was recently shown by Li *et al.*[94] that the SC model gives reliable results for the conductivity of graphene for packing fractions $p \ll 1$ by comparing the analytical result for the 2D structure factor in that model, $I(q)$, with a numerically calculated structure factor of a hexagonal lattice of impurities. However, the analytical limit $I_{SC}(0) = 1 - 4p$ shows that the SC model already breaks down for $p \geq 0.25$ because the corresponding compressibility becomes negative at higher packing fractions. On the other hand, it was recently shown that the interaction potential between two point ions near doped graphene is heavily screened and, moreover, exhibits Friedel oscillations with inter-particle distance, giving rise to a strongly repulsive core region of distances on the order of k_F^{-1} that resembles

the interaction among hard disks with diameter $r_c \sim k_F^{-1}$. Therefore, we may estimate that the packing factor could reach values on the order $p \sim n_{\rm imp}/\bar{n}$ that may not always be negligibly small, necessitating the use of a model that goes well beyond the SC model, at least for systems of adsorbed alkali-atom submonolayers on graphene [95]. In that respect, we note that various parameterizations of the HD model extend its applicability to include phase transitions in a 2D fluid as a function of the packing fraction [102], even going up about $p = 0.9$, corresponding to a crystalline closest packing where hard disks form a hexagonal structure in 2D [103]. In this work, we use a simple analytical parametrization for the 2D structure factor in the HD model, $I_{HD}(q)$, provided by Rosenfeld [100], which works reasonably well for packing fractions up to about $p = 0.69$, just near the freezing point of a 2D fluid.

We summarize expressions that define the structure factor for the Hard disk (HD) model due to Rosenfeld[100] for a 2D planar distribution of charged impurities with the packing fraction $p = \pi n_{\rm imp} r_c^2/4$, where $n_{\rm imp} = N/A$ is their areal number density and r_c is the disk diameter,

$$I_{HD}(q) = \left\{ 1 + 16a \left[\frac{J_1(qr_c/2)}{qr_c} \right]^2 + 8b \frac{J_0(qr_c/2) J_1(qr_c/2)}{qr_c} + \frac{8p}{1-p} \frac{J_1(qr_c)}{qr_c} \right\}^{-1} \tag{D.1}$$

with

$$\begin{aligned} a &= 1 + x(2p-1) + \frac{2p}{1-p}, \\ b &= x(1-p) - 1 - \frac{3p}{1-p}, \\ x &= \frac{1+p}{(1-p)^3}. \end{aligned}$$

Note that the important long wavelength limit is given by $I_{HD}(0) = 1/x = (1-p)^3/(1+p)$. The expression in Eq. (D.1) should be compared with the structure factor for a model with the step-like pair correlation function [95, 94],

$$I_{SC}(q) = 1 - \frac{8p}{qr_c} J_1(qr_c), \tag{D.2}$$

which gives $I_{SC}(0) = 1 - 4p$.

Appendix E

Green's function for Poisson equation in Debye-Hückel approximation

We can express a solution of the Poisson equation in the presence of external charge distribution $\rho_{\text{ext}}(\mathbf{R})$ in terms of the Green's function as

$$\Phi(\mathbf{R}) = \iiint d^3\mathbf{R}' G(\mathbf{R}, \mathbf{R}') \rho_{\text{ext}}(\mathbf{R}'), \tag{E.1}$$

where $\mathbf{R} = (x, y, z)$. Due to translational invariance, we may use a 2D Fourier transform to write

$$G(\mathbf{R}, \mathbf{R}') = G(\mathbf{r} - \mathbf{r}'; z, z') = \iint \frac{d^2\mathbf{q}}{(2\pi)^2} \mathrm{e}^{-i\mathbf{q}\cdot(\mathbf{r}-\mathbf{r}')} \tilde{G}(\mathbf{q}; z, z') \tag{E.2}$$

where $\mathbf{r} = (x, y)$ and $\mathbf{q} = (q_x, q_y)$ so that

$$\widetilde{\Phi}(\mathbf{q}, z) = \int dz' \, \widetilde{G}(\mathbf{q}; z, z') \widetilde{\rho}_{\text{ext}}(\mathbf{q}, z') \tag{E.3}$$

So, the 2D FT of the fluctuating potential in the plane of graphene $\widetilde{\phi}_0(\mathbf{q})$ in Eq. (6.38) can be written as

$$\widetilde{\phi}_0(\mathbf{q}) = \int dz' \, \widetilde{G}(\mathbf{q}; 0, z') \widetilde{\rho}_{\text{ext}}(\mathbf{q}, z') \tag{E.4}$$

If the external charges are located in the region 1 and are represented by the charged impurities, $\text{ext}(\mathbf{q}, z) \equiv \text{ext}(\mathbf{q}, z)$, one may express the 2D FT of the fluctuating potential $\widetilde{\Phi}(z) \equiv \widetilde{\Phi}(\mathbf{q}, z)$ throughout the system by using the 2D FT $\widetilde{G}(z, z') \equiv \widetilde{G}(\mathbf{q}; z, z')$ of a full Green's function $G(\mathbf{r} - \mathbf{r}'; z, z')$ for the Poisson equation (6.4) with the source point located in region 1, $z' \leq 0$. By defining such a function in the piece-wise manner so that

$\widetilde{G}(z,z') = \widetilde{G}_j(z,z')$ with $j = 1$, 2, and 3 for z in regions 1, 2 and 3, its components may be found as solutions of the following equations that follow from Eqs. (6.33)-(6.35),

$$\frac{\partial^2}{\partial z^2}\widetilde{G}_1(z,z') - q^2\widetilde{G}_1(z,z') = -\frac{4\pi}{\epsilon_1}\,\delta(z-z'), \tag{E.5}$$

$$\frac{\partial^2}{\partial z^2}\widetilde{G}_2(z,z') - q^2\widetilde{G}_2(z,z') = 0, \tag{E.6}$$

$$\frac{\partial^2}{\partial z^2}\widetilde{G}_3(z,z') - \left(q^2+\kappa^2\right)\widetilde{G}_3(z,z') = 0. \tag{E.7}$$

As usual, one defines two components of the Green's function in region 1,

$$\widetilde{G}_1(z,z') = \begin{cases} \widetilde{G}_1^{<}(z,z'), & -t \le z \le z' \le 0, \\ \widetilde{G}_1^{>}(z,z'), & -t \le z' \le z \le 0, \end{cases} \tag{E.8}$$

which must satisfy the continuity and the jump conditions for $\widetilde{G}_1(z,z')$ at $z = z'$,

$$\widetilde{G}_1^{<}(z',z') = \widetilde{G}_1^{>}(z',z'), \tag{E.9}$$

$$\frac{\partial}{\partial z}\widetilde{G}_1^{>}(z,z')\bigg|_{z=z'} - \frac{\partial}{\partial z}\widetilde{G}_1^{<}(z,z')\bigg|_{z=z'} = -\frac{4\pi}{\epsilon_1}. \tag{E.10}$$

Moreover, the solutions of Eqs. (E.5)-(E.7) need to satisfy the same (linear and homogeneous) boundary and matching conditions as the potential components $\widetilde{\Phi}_j(z)$,

$$\widetilde{G}_1^{<}(-t,z') = 0, \tag{E.11}$$

$$\widetilde{G}_1^{>}(0,z') = \widetilde{G}_2(0,z'), \tag{E.12}$$

$$-\epsilon_2\,\frac{\partial}{\partial z}\widetilde{G}_2(z,z')\bigg|_{z=0} + \epsilon_1\,\frac{\partial}{\partial z}\widetilde{G}_1^{>}(z,z')\bigg|_{z=0} = 4\pi e^2\chi(q)\widetilde{G}_1^{>}(0,z'), \tag{E.13}$$

$$\widetilde{G}_2(h,z') = \widetilde{G}_3(h,z'), \tag{E.14}$$

$$\epsilon_2\,\frac{\partial}{\partial z}\widetilde{G}_2(z,z')\bigg|_{z=h} = \epsilon_3\,\frac{\partial}{\partial z}\widetilde{G}_3(z,z')\bigg|_{z=h}, \tag{E.15}$$

$$\widetilde{G}_3(\infty,z') = 0. \tag{E.16}$$

Note that all these conditions are of the Dirichlet or the Neumann type, except for the jump condition at $z = 0$ in Eq. (E.13), which is of the Robin type in conjunction with the continuity condition at $z = 0$ in Eq. (E.12). This type of matching condition is a consequence of the zero-thickness approximation for graphene, and we note that similar conditions arise in mathematical modeling of electrostatic phenomena involving other graphene-based structures, such as carbon nanotubes [104].

While it would be quite feasible to solve Eqs. (E.5)-(E.7) for the Green's function $\widetilde{G}(z,z')$ satisfying the full set of the boundary and matching conditions, Eqs. (E.11)-(E.16), we may take advantage of the linear-response treatment of graphene and the fact that its

presence in the system may be brought into the 2D FT of the Poisson equation (6.4) by including a homogeneous term of the form $\widehat{V}(z)\widetilde{\Phi}(z)$, where $\widehat{V}(z) \equiv -4\pi e^2\chi(q)\delta(z)$. Then, one may solve Eqs. (E.5)-(E.7) for the components of a Green's function $\widetilde{G}^{(0)}(z,z')$ for the system *without* graphene, which satisfies the same set of boundary and matching conditions as does $\widetilde{G}(z,z')$, Eqs. (E.11)-(E.16), except that the jump condition in Eq. (E.13) is to be changed to a Neumann type by setting $\chi(q) = 0$ (that is, by removing graphene) in the right-hand side of that equation,

$$-\epsilon_2 \left.\frac{\partial \widetilde{G}_2^{(0)}(z,z')}{\partial z}\right|_{z=0} + \epsilon_1 \left.\frac{\partial \widetilde{G}_1^{(0)}(z,z')}{\partial z}\right|_{z=0} = 0. \tag{E.17}$$

Clearly, it is easier to find the Green's function for the system without graphene, $\widetilde{G}^{(0)}(z,z')$, for example, by adapting the method used in the DH theory for slab geometries [105]. Then, the resulting Dyson-Schwinger equation for the full Green's function $\widetilde{G}(z,z')$ for the system in the presence of graphene in the plane $z = 0$,

$$\widetilde{G}(z,z') = \widetilde{G}^{(0)}(z,z') + \frac{1}{4\pi}\int dz''\, \widetilde{G}^{(0)}(z,z'')\widehat{V}(z'')\widetilde{G}(z'',z'), \tag{E.18}$$

may be easily solved owing to the Dirac delta function in the definition of the "potential" $\widehat{V}(z)$, giving

$$\widetilde{G}(z,z') = \widetilde{G}^{(0)}(z,z') - \frac{e^2\chi(q)\widetilde{G}^{(0)}(z,0)\widetilde{G}^{(0)}(0,z')}{1+e^2\chi(q)\widetilde{G}^{(0)}(0,0)}. \tag{E.19}$$

With the result in Eq. (E.19), we may express the FT of the fluctuating part of the in-plane potential as

$$\widetilde{\phi}_0 = \int_{-t}^{0} dz'\, \widetilde{G}_1(0,z')\widetilde{\rho}_{\rm imp}(z') = \frac{1}{1+e^2\chi(q)\widetilde{G}^{(0)}(0,0)}\int_{-t}^{0} dz'\, \widetilde{G}_1^{(0)}(0,z')\widetilde{\rho}_{\rm imp}(z'). \tag{E.20}$$

As each component of $\widetilde{G}_1^{(0)}$ satisfies Eq. (E.5), we may write the general solution as

$$\widetilde{G}_{1<}^{(0)}(z,z') = Ae^{qz} + Be^{-qz} \tag{E.21}$$

$$\widetilde{G}_{1>}^{(0)}(z,z') = Ce^{qz} + De^{-qz}, \tag{E.22}$$

where A, B, C, and D are some constants to be determined by boundary conditions (BCs). Similarly, the homogeneous DEs for $\widetilde{G}_2^{(0)}$ and $\widetilde{G}_3^{(0)}$ have the same form of general solutions as

$$\widetilde{G}_2^{(0)}(z,z') = Ee^{qz} + Fe^{-qz} \tag{E.23}$$

$$\widetilde{G}_3^{(0)}(z,z') = He^{-\sqrt{q^2+\kappa^2}z} \tag{E.24}$$

Now there are 7 constants A, B, C, D, E, F, and H to be determined by 7 BCs given by Eqs. (E.11), (E.12), (E.14)-(E.16), and (E.17).Therefore, substituting general solutions (Eqs. (E.21)-(E.24)) into BCs, we have

$$Ae^{qz'} + Be^{-qz'} = Ce^{qz'} + De^{-qz'} \tag{E.25}$$

$$Ae^{qz'} - Be^{-qz'} - Ce^{qz'} + De^{-qz'} = -\frac{4\pi}{q\epsilon_1} \tag{E.26}$$

$$C + D = E + F \tag{E.27}$$

$$Ee^{qh} + Fe^{-qh} = He^{-\sqrt{q^2+\kappa^2}h} \tag{E.28}$$

$$\epsilon_1(C - D) = \epsilon_2(E - F) \tag{E.29}$$

$$\epsilon_2 q(Ee^{qh} - Fe^{-qh}) = -\epsilon_3\sqrt{q^2+\kappa^2}He^{-\sqrt{q^2+\kappa^2}h} \tag{E.30}$$

We are interested only in the component of the graphene-free Green's function for $z \leq 0$ and $z' \leq 0$, for which we find

$$\widetilde{G}_1^{(0)}(z,z') = \frac{4\pi}{q}\sinh\left[q(z_< + t)\right]\frac{\cosh(qz_>) - \dfrac{\epsilon_2}{\epsilon_1}\Gamma(q)\sinh(qz_>)}{\epsilon_1\cosh(qt) + \epsilon_2\Gamma(q)\sinh(qt)}, \tag{E.31}$$

where $z_< = \min(z,z')$, $z_> = \max(z,z')$, and

$$\Gamma(q) = \frac{\epsilon_2 q\tanh(qh) + \epsilon_3\sqrt{q^2+\kappa^2}}{\epsilon_2 q + \epsilon_3\sqrt{q^2+\kappa^2}\tanh(qh)}. \tag{E.32}$$

For the sake of completeness, we also quote final results for the other two components of that function for $0 \leq z \leq h$ and $z \geq h$ (with $z' \leq 0$), which are respectively given by

$$\widetilde{G}_2^{(0)}(z,z') = \frac{4\pi}{q}\sinh\left[q(z' + t)\right]\frac{\cosh(qz) - \Gamma(q)\sinh(qz)}{\epsilon_1\cosh(qt) + \epsilon_2\Gamma(q)\sinh(qt)}, \tag{E.33}$$

$$\widetilde{G}_3^{(0)}(z,z') = \frac{4\pi}{q}\sinh\left[q(z' + t)\right]\frac{\cosh(qh) - \Gamma(q)\sinh(qh)}{\epsilon_1\cosh(qt) + \epsilon_2\Gamma(q)\sinh(qt)}\mathrm{e}^{-\sqrt{q^2+\kappa^2}(z-h)}. \tag{E.34}$$

Appendix F

Green's function for partially linearized Poisson equation

We generalize here the results of the previous section assuming that external charges exist in both the region 1, where they represent charged impurities with the density $\rho_{\rm imp}(\mathbf{r}, z)$ in the oxide layer, as well as in the region 3, where they represent charged biomolecules with the density $\rho_{\rm bio}(\mathbf{r}, z)$ in the electrolyte. In order to express the solution of the partially linearized Poisson-Boltzmann equation in terms of the 2D FT of its Green's function, we need to obtain all of its components, $\widetilde{G}_{jk}(\mathbf{q}; z, z')$, where the first index denotes the case when the point z is in the region j and the second index describes the case when the source point z' is in the region k. Thus, the FT of the fluctuating potential in the plane of graphene may be written as

$$\widetilde{\phi}_0(\mathbf{q}) = \int_{-t}^{0} dz'\, \widetilde{G}_{11}(\mathbf{q}; 0, z')\widetilde{\rho}_{\rm imp}(\mathbf{q}, z') + \int_{h}^{\infty} dz'\, \widetilde{G}_{13}(\mathbf{q}; 0, z')\widetilde{\rho}_{\rm bio}(\mathbf{q}, z'). \tag{F.1}$$

Here, the components of the GF $\widetilde{G}_{jk}$ in the presence of graphene layer at $z = 0$ (i.e., the boundary between the regions 1 and 2) may be expressed in terms of the GF $\widetilde{G}^{(0)}_{jk}$ *without* graphene, as described in the previous section,

$$\widetilde{G}_{jk}(z, z') = \widetilde{G}^{(0)}_{jk}(z, z') - \frac{e^2\chi(q)\widetilde{G}^{(0)}_{j1}(z, 0)\widetilde{G}^{(0)}_{1k}(0, z')}{1 + e^2\chi(q)\widetilde{G}^{(0)}_{11}(0, 0)}. \tag{F.2}$$

We deduce now a set of second-order, linear ODEs with non-constant coefficients for the components $\widetilde{G}^{(0)}_{jk}(z, z')$ of the FTGF corresponding to the partially linearized PB equations (7.47), (7.48) and (7.49) as

$$\frac{\partial^2}{\partial z^2}\widetilde{G}^{(0)}_{jk}(\mathbf{q}; z, z') - Q_j^2(z)\widetilde{G}^{(0)}_{jk}(\mathbf{q}; z, z') = -\frac{4\pi}{\epsilon_j}\,\delta_{jk}\,\delta(z - z'), \text{ for } z \in I_j \text{ and } z' \in I_k, \tag{F.3}$$

where

$$Q_j^2(z) \;=\; \begin{cases} q^2 & \text{for } j=1,2 \\ q^2+\kappa^2\left\{1+2\,\mathrm{csch}^2[\kappa\,(z+z_0)]\right\} & \text{for } j=3. \end{cases} \tag{F.4}$$

We see in Eq. (F.3) that, in comparison with the set of ODEs for the PB equation in the DH approximation, the main difference is that now the parameter $Q_3(z)$ in the region I_3 depends on distance z and includes, via the parameter z_0, all the information about the averaged features of the entire structure containing graphene in the regime of dual gating. All the functions FTGF $\widetilde{G}_{jk}^{(0)}(\mathbf{q};z,z')$ may be obtained analytically by solving Eq. (F.3) and applying the boundary and matching conditions given in Eqs. (E.11)-(E.16) (with the jump condition in Eq. (E.13) replaced by Eq. (E.17) in the absence of graphene) for $j=1,2,3$, respectively. At the same time, index k is assumed to only take values $k=1,3$ since no sources of charges are expected to reside in region I_2 representing the Stern layer.

In the following, we shall drop the superscript (0) and omit the variable $\mathbf{q}$ in the FTGF $\widetilde{G}_{jk}^{(0)}(\mathbf{q};z,z')$, and only list final expressions. The details of the derivation may be found in the Master thesis by Naijing Kang, University of Waterloo, 2015.

Source point in I_1 $(k=1)$

The final expressions for $\widetilde{G}_{11}(z,z')$, $\widetilde{G}_{21}(z,z')$ and $\widetilde{G}_{31}(z,z')$ may be written in a compact form if we define several parameters as;

$$\Delta_t \;=\; \mathrm{e}^{2qt}, \tag{F.5}$$

$$\Delta_h \;=\; \mathrm{e}^{-2qh}, \tag{F.6}$$

$$\lambda_\mathrm{b} \;=\; \frac{\epsilon_1-\epsilon_2}{\epsilon_1+\epsilon_2}, \tag{F.7}$$

$$\lambda_\mathrm{h} \;=\; \frac{\epsilon_3 U_-'(h)+\epsilon_2 q U_-(h)}{\epsilon_3 U_-'(h)-\epsilon_2 q U_-(h)}, \tag{F.8}$$

$$\gamma \;=\; \frac{-\lambda_\mathrm{h}\lambda_\mathrm{b}\Delta_h+1}{-\lambda_\mathrm{h}\Delta_h+\lambda_\mathrm{b}}, \tag{F.9}$$

$$\eta \;=\; \frac{\sinh(qt)-\frac{\epsilon_1}{\epsilon_2}\cosh(qt)}{\sinh(qt)+\frac{\epsilon_1}{\epsilon_2}\cosh(qt)}. \tag{F.10}$$

The final solution is:

$$\widetilde{G}_{11}(z,z') \;=\; \frac{4\pi}{q\epsilon_1}\sinh[q(z^<+t)]\,\frac{\mathrm{e}^{qz^>}+\gamma\mathrm{e}^{-qz^>}}{\mathrm{e}^{qt}\gamma+\mathrm{e}^{-qt}} \tag{F.11}$$

$$\widetilde{G}_{21}(z,z') \;=\; \frac{4\pi}{q\bar{\epsilon}_{12}}\,\frac{\sinh[q(z'+t)]}{-\lambda_\mathrm{h}\Delta_h+\lambda_\mathrm{b}}\,\frac{-\mathrm{e}^{qz}\lambda_\mathrm{h}\Delta_h+\mathrm{e}^{-qz}}{\mathrm{e}^{qt}\gamma+\mathrm{e}^{-qt}} \tag{F.12}$$

$$\widetilde{G}_{31}(z,z') \;=\; \frac{4\pi}{q\bar{\epsilon}_{12}}\,\frac{\sinh[q(z'+t)]}{-\lambda_\mathrm{h}\Delta_h+\lambda_\mathrm{b}}\,\frac{\mathrm{e}^{-qh}(1-\lambda_\mathrm{h})}{\mathrm{e}^{qt}\gamma+\mathrm{e}^{-qt}}\,\frac{U_-(z)}{U_-(h)}. \tag{F.13}$$

Source point in I_3 ($k = 3$)

In order to write the solutions for the GF components in a compact form, we introduce some additional parameters:

$$\Gamma_{1\pm} = \epsilon_2 q U_\pm(h) - \epsilon_3 U'_\pm(h) \tag{F.14}$$

$$\Gamma_{2\pm} = \epsilon_2 q U_\pm(h) + \epsilon_3 U'_\pm(h) \tag{F.15}$$

$$\Omega_\pm = \Gamma_{1\pm} - \Gamma_{2\pm}\Delta_h\eta. \tag{F.16}$$

In this way, we obtain the final solution of $\widetilde{G}_{13}$,$\widetilde{G}_{23}$,$\widetilde{G}_{33}$ as:

$$\widetilde{G}_{13}(z,z') = 4\pi \frac{(1+\eta)\mathrm{e}^{-qh}}{\sinh(qt)\,\Omega_-} \sinh[q(t+z)] U_-(z') \tag{F.17}$$

$$\widetilde{G}_{23}(z,z') = \frac{4\pi \mathrm{e}^{-qh}}{\Omega_-} \left(\mathrm{e}^{qz} + \eta\, \mathrm{e}^{-qz}\right) U_-(z') \tag{F.18}$$

$$\widetilde{G}_{33}(z,z') = \frac{4\pi}{\epsilon_3 W} \left[\frac{\Omega_+}{\Omega_-} U_-(z)U_-(z') - U_+(z^<)U_-(z^>)\right]. \tag{F.19}$$

In the above expressions we have defined $z^< = \min(z,z')$ and $z^> = \max(z,z')$.

References

[1] A. H. Castro Neto, F. Guinea, N. M. Peres, K. S. Novoselov, and A. K. Geim. The electronic properties of graphene. *Rev. Mod. Phys.*, 81:109, 2009.

[2] T. Izraeli. Temperature dependence of conductivity in graphene. *Final Project in the Computational Physics Course (Fall Semester 2012-13), http://phelafel.technion.ac.il/ tzipora/.*

[3] M. Z. Bazant, M. S. Kilic, B. D. Storey, and A. Ajdari. Towards an understanding of induced-charge electrokinetics at large applied voltages in concentrated solutions. *Advances in Colloid and Interface Science*, 152:48, 2009.

[4] S. Gavryushov and P. Linse. Polarization deficiency and excess free energy of ion hydration in electric fields. *J. Phys. Chem. B*, 107:7135–7142, 2003.

[5] E. Gongadze, U. van Rienen, V. Kralj-Iglic, and A. Iglic. Spatial variation of permittivity of an electrolyte solution in contact with a charged metal surface: a mini review. *Computer Methods in Biomechanics and Biomedical Engineering*, 16:463, 2013.

[6] P. R. Wallace. The band theory of graphite. *Phys. Rev.*, 71:622, 1947.

[7] Y. Liu, X. Dong, and P. Chen. Biological and chemical sensors based on graphene materials. *Chem. Soc. Rev.*, 41:2283, 2012.

[8] K. Balasubramanian and K. Kern. 25th anniversary article: Label-free electrical biodetection using carbon nanostructures. *Adv. Mater.*, 26:1154, 2014.

[9] D. Jariwala, V.K. Sangwan, L. J. Lauhon, T. J. Marksab, and M. C. Hersam. Carbon nanomaterials for electronics, optoelectronics, photovoltaics, and sensing. *Chem. Soc. Rev.*, 42:2824, 2013.

[10] L. H. Hess, M. Seifert, and J. A. Garrido. Graphene transistors for bioelectronics. *Proc. IEEE*, 101:1780, 2013.

[11] Y. Yang, A. M. Asiri, Z. Tang, D. Du, and Y. Lin. Graphene based materials for biomedical applications. *Materials Today*, 16:365, 2013.

[12] M. W. Shinwari, M. J. Deen, and D. Landheer. Study of the electrolyte-insulator-semiconductor field-effect transistor (eisfet) with applications in biosensor design. *Microelectron. Reliab.*, 47:2025, 2007.

[13] F. Chen, Q. Qing, J. Xia, and N. Tao. Graphene field-effect transistors: Electrochemical gating, interfacial capacitance, and biosensing applications. *Chem. Asian J.*, 5:2144, 2010.

[14] Ph. Avouris and F. Xia. Graphene applications in electronics and photonics. *MRS Bulletin*, 37:1225, 2012.

[15] D. Chen, L. Tang, and J. Li. Critical review: Graphene-based materials in electrochemistry. *Chem. Soc. Rev.*, 39:3157, 2010.

[16] A. J. Bard and L. R. Faulkner. *Electrochemical Methods: Fundamentals and Applications*. Willey, 2nd ed. edition, 2001.

[17] I. Heller, S. Chatoor, J. Mannik, M. A. G. Zevenbergen, C. Dekker, and S. G. Lemay. Influence of electrolyte composition on liquid-gated carbon nanotube and graphene transistors. *J. Am. Chem. Soc.*, 132:17149, 2010.

[18] B. Mailly-Giacchetti, A. Hsu, H. Wang, V. Vinciguerra, F. Pappalardo, L. Occhipinti, E. Guidetti, S. Coffa, J. Kong, and T. Palacios. ph sensing properties of graphene solution-gated field-effect transistors. *J. Appl. Phys.*, 114:084505, 2013.

[19] S. Chen, Z.-B. Zhang, L. Ma, P. Ahlberg, X. Gao, Z. Qiu, D. Wu, W. Ren, H.-M. Cheng, and S.-L. Zhang. A graphene field-effect capacitor sensor in electrolyte. *Appl. Phys. Lett.*, 101:154106, 2012.

[20] H. Gerischer, R. McIntyre, D. Scherson, and W. Storck. Density of the electronic states of graphite: derivation from differential capacitance measurements. *J. Phys. Chem.*, 91:1930, 1987.

[21] A. Hartl, J. A. Garrido, S. Nowy, R. Zimmermann, C. Werner, D. Horinek, R. Netz, and M. Stutzmann. The ion sensitivity of surface conductive single crystalline diamond. *J. Am. Chem. Soc.*, 129:1287, 2007.

[22] J. A. Garrido, S. Nowy, A. Hartl, and M. Stutzmann. The diamond/aqueous electrolyte interface: an impedance investigation. *Langmuir*, 24:3897, 2008.

[23] T. Fang, A. Konar, H. L. Xing, and D. Jena. Carrier statistics and quantum capacitance of graphene sheets and ribbons. *Appl. Phys. Lett.*, 91:092109, 2007.

[24] J. Xia, F. Chen, J. Li, and N. Tao. Measurement of the quantum capacitance of graphene. *Nat. Nanotechnol.*, 5:505, 2009.

[25] J.-H. Zhong, J.-Y. Liu, Q. Li, M.-G. Li, Z.-C. Zeng, S. Hu, D.-Y. Wu, W. Cai, and B. Ren. Interfacial capacitance of graphene: Correlated differential capacitance and in situ electrochemical raman spectroscopy study. *Electrochimica Acta*, 110:754, 2013.

[26] Y. Y. Wang, T. D. Pham, K. Zand, J. Li, and P. J. Burke. Charging the quantum capacitance of graphene with a single biological ion channel. *ACS Nano*, 8:4228, 2014.

[27] M. Dankerl, M. V. Hauf, A. Lippert, L. H. Hess, S. Birner, I. D. Sharp, A. Mahmood, P. Mallet, J.-Y. Veuillen, M. Stutzmann, and J. A. Garrido. Graphene solution-gated field-effect transistor array for sensing applications. *Adv. Funct. Mater.*, 20:3117, 2010.

[28] J. Ristein, W. Zhang, F. Speck, M. Ostler, L. Ley, and Th. Seyller. Characteristics of solution gated field effect transistors on the basis of epitaxial graphene on silicon carbide. *J. Phys. D: Appl. Phys.*, 43:345303, 2010.

[29] Z. L. Mišković and N. Upadhyaya. Modeling electrolytically top-gated graphene. *Nanoscale Res. Lett.*, 5:505, 2010.

[30] Z. L. Mišković, P. Sharma, and F. O. Goodman. Ionic screening of charged impurities in electrolytically gated graphene. *Phys. Rev. B*, 86:115437, 2012.

[31] P. Sharma and Z. L. Mišković. Effects of finite ion size and dielectric saturation of water in electrolytically top-gated graphene. *The International Conference on Applied Mathematics, Modeling and Computational Science*, page 334, 2013.

[32] P. Sharma and Z. L. Mišković. Ionic screening of charged impurities in graphene. *The International Conference on Applied Mathematics, Modeling and Computational Science*, page 230, 2011.

[33] P. Sharma and Z. L. Mišković. Capacitance of graphene in aqueous electrolytes:the effects of dielectric saturation of water and finite size of ions. *Phys. Rev. B*, 90:125415, 2014.

[34] P. Sharma and Z. L. Mišković. Ionic screening of charged impurities in electrolytically gated graphene using green's function approach. *The 2015 AMMCS-CAIMS Congress*, page 199, 2015.

[35] H. Boroudjerdi, Y.-W. Kim, A. Naji, R. R. Netz, X. Schlagberger, and A. Serr. Statics and dynamics of strongly charged soft matter. *Phys. Reports*, 416:129, 2005.

[36] M. V. Fedorov and A. A. Kornyshev. Ionic liquids at electrified interfaces. *Chem. Rev.*, 114:2978, 2014.

[37] F. Chen, J. Xia, and N. Tao. Ionic screening of charged-impurity scattering in graphene. *Nano Letters*, 9:1621, 2009.

[38] E. H. Hwang and S. D. Sarma. Screening-induced temperature-dependent transport in two-dimensional graphene. *Phys. Rev. B*, 79:165404, 2009.

[39] S. D. Sarma, S. Adam, E. H. Hwang, and E. Rossi. Electronic transport in two-dimensional graphene. *Rev. Mod. Physics*, 83:407, 2011.

[40] J. J. Bikerman. Structure and capacity of electrical double layer. *Philos. Mag.*, 33:384, 1942.

[41] V. Freise. Zur theorie der diffusen doppelschicht. *Z. Elektrochem.*, 56:822, 1952.

[42] M. S. Kilic, M. Z. Bazant, and A. Ajdari. Steric effects in the dynamics of electrolytes at large applied voltages. i. double-layer charging. *Phys. Rev. E*, 75:021502, 2007.

[43] A. A. Kornyshev. Double-layer in ionic liquids: paradigm change? *J. Phys. Chem. B*, 111:5545, 2007.

[44] A. Abrashkin, D. Andelman, and H. Orland. Dipolar poisson-boltzmann equation: ions and dipoles close to charge interfaces. *Phys. Rev. Lett.*, 99:077801, 2007.

[45] D. C. Grahame. Effects of dielectric saturation upon the diffuse double layer and the free energy of hydration of ions. *J. Chem. Phys.*, 18:903, 1950.

[46] F. Booth. The dielectric constant of water and the saturation effect. *J. Chem. Phys.*, 19:391, 1951.

[47] H. Wang, J. Varghese, and L. Pilon. Simulation of electric double layer capacitors with mesoporous electrodes: Effects of morphology and electrolyte permittivity. *Electrochimica Acta*, 56:6189, 2011.

[48] H. Wang and L. Pilon. Accurate simulations of electric double layer capacitance of ultramicroelectrodes. *J. Phys. Chem. C*, 115:16711, 2011.

[49] V. N. Puanov, R. I. Dimova, P. A. Kralchevshy, G. Broze, and A. Mehreteab. The hydration repulsion between charged surfaces as an interplay of volume exclusion and dielectric saturation effects. *J. Colloid Interface Sci.*, 182:239, 1986.

[50] M. Aguilella-Arzo, A. Andrio, V. M. Aguilella, and A. Alcaraz. Dielectric saturation of water in a membrane protein channel. *Phys. Chem. Chem. Phys.*, 11:358, 2009.

[51] I.-C. Yeh and M. L. Berkowitz. Dielectric constant of water at high electric fields: Molecular dynamics study. *J. Chem. Phys.*, 110:7935, 1999.

[52] J. Toulouse, G. Jansen I. C. Gerber, A. Savin, and J. G. Angyan. Adiabatic-connection fluctuation-dissipation density-functional theory based on range separation. *Phys. Rev. Lett.*, 102:096404, 2009.

[53] R. Scherrer. *Quantum Mechanics: An Accessible Introduction*. Addison-Wesley Publishing Company, 2005.

[54] Z. Xu (Editor). *Graphene: Properties, Synthesis and Applications*. Nova Science Publishers Inc., 2011.

[55] S. Reich, J. Maultzsch, C. Thomsen, and P. Ordejon. Tight-binding description of graphene. *Phys. Rev. B*, 66:035412, 2002.

[56] J. Jung and A. H. MacDonald. Tight-binding model for graphene π-bands from maximally localized wannier functions. *Phys. Rev. B*, 87:195450, 2013.

[57] K. S. Novoselov, A. K. Geim, S. V. Morozov, D. Jiang, M. I. Katsnelson, I. V. Grigorieva, S. V. Dubonos, and A. A. Firsov. Two-dimensional gas of massless dirac fermions in graphene. *Nature*, 438:197, 2005.

[58] Y. Zhang, Y.-W. Tan, H. L. Stormer, and P. Kim. Experimental observation of the quantum hall effect and berry's phase in graphene. *Nature*, 438(7065):201, 2005.

[59] M. Katsnelson. *Graphene: Carbon in two dimensions*. Cambridge University Press, New York, 2012.

[60] J. P. Hobson and W. A. Nierenberg. The statistics of a two-dimensional, hexagon net. *Phys. Rev.*, 89:662, 1953.

[61] M. Abramowitz and I. A. Stegun. *Handbook of Mathematical Functions*. National Bureau of Standards, Washington, DC, 1965.

[62] M. Ghaznavi, Z. L. Mišković, and F. O. Goodman. Nonlinear screening of external charge by doped graphene. *Phys. Rev. B*, 81:085416, 2010.

[63] M. Polini, A. Tomadin, R. Asgari, and A. H. MacDonald. Density functional theory of graphene sheets. *Phys. Rev. B*, 78:115426, 2008.

[64] N. W. Ashcroft and N. D. Mermin. *Solid State Physics*. Thomson Learning, Toronto, 1976.

[65] S. Das Sarma, B. Yu-Kuang Hu, E. Hwang, and W. Tse. Electron-electron interactions in graphene. *arXiv:0708.3239 [cond-mat.mtrl-sci]*, 2007.

[66] E. G. Mishchenko. Effects of electron-electron interactions on the conductivity of clean graphene. *Phys. Rev. Lett.*, 98:216801, 2007.

[67] D. Bohm and D. Pines. A collective description of electron interactions: Iii. coulomb interactions in a degenerate electron gas. *Phys. Rev.*, 92:609, 1953.

[68] K. W. K. Shung. Dielectric function and plasmon structure of stage-1 intercalated graphite. *Phys. Rev. B*, 34:979, 1986.

[69] E. H. Hwang and S. D. Sarma. Dielectric function, screening, and plasmons in two-dimensional graphene. *Phys. Rev. B*, 75:205418, 2007.

[70] B. Wunsch, T. Stauber, F. Sols, and F. Guinea. Dynamical polarization of graphene at finite doping. *New J. Phys.*, 8:318, 2006.

[71] T. Ando. Screening effect and impurity scattering in monolayer graphene. *J. Phys. Soc. Jpn.*, 75:074716, 2006.

[72] S. Adam, E. H. Hwang, V. M. Galitski, and S. D. Sarma. A self-consistent theory for graphene transport. *Proceedings of the National academy of Sciences, USA*, 104:18392, 2007.

[73] M. I. Katsnelson and A. K. Geim. Electron scattering on microscopic corrugations in graphene. *Philos. Trans. R. Soc. London, Ser. A*, 366:195, 2008.

[74] R. Anicic and Z. L. Mišković. Effects of the structure of charged impurities and dielctric environment on conductivity of graphene. *Phys. Rev. B*, 88:205412, 2013.

[75] R. Anicic and Z. L. Mišković. Potential fluctuations in graphene due to correlated charged impurities in substrate. *Appl. Phys. Lett.*, 103:171606, 2013.

[76] I. Borukhov, D. Andelman, and H. Orland. Steric effects in electrolytes: A modified poisson-boltzmann equation. *Phys. Rev. Lett.*, 79:435, 1997.

[77] I. Borukhov, D. Andelman, and H. Orland. *(unpublished).*

[78] E. Gongadze, U. V. Rienen, and A. Iglić. Generalized stern models of the electric double layer considering the spatial variation of permittvity and finite size of ions in saturation regime. *Cell. Mol. Biol. Lett.*, 16:576, 2011.

[79] I. Borukhov, D. Andelman, and H. Orland. Polyelectrolyte solutions between charged surfaces. *Europhys. Lett.*, 32:499, 1995.

[80] J. O. Bockris and A. K. N. Reddy. *Modern Electrochemistry.* Plenum, New York, 1970.

[81] E. Gongadze, U. V. Rienen, V. K. Iglić, and A. Iglić. Spatial variation of permittivity near the charged membrane in contact with electrolyte solution. *Advances in planar lipid bilayers and liposomes*, 11:101, 2010.

[82] A. Iglić, E. Gongadze, and K. Bohinc. Excluded volume effect and orientational ordering near charged surface in solution of ions and langevin dipoles. *Bioelectrochemistry*, 79:223, 2010.

[83] E. Gongadze, U. V. Rienen, V. K. Iglić, and A. Iglić. Langevin poisson-boltzmann equation: point-like ions and water dipoles near a charged membrane surface. *Gen. Physiol. Biophys.*, 30:130, 2011.

[84] E. Gongadze and A. Iglić. Decrease of permittivity of an electrolyte solution near a charged surface due to saturation and excluded volume effects. *Bioelectrochemistry*, doi:10.1016/j.bioelechem.2011.12.001, 2012.

[85] B. Pettinger and K. Doblhofer. A practical approach to modeling the electrical double layer in the presence of specific adsorption of ions. *Can. J. Chem.*, 75:1710, 1997.

[86] A. Kretinin, G. L. Yu, R. Jalil, Y. Cao, F. Withers, A. Mishchenko, M. I. Katsnelson, K. S. Novoselov, A. K. Geim, , and F. Guinea. Quantum capacitance measurements of electron-hole asymmetry and next-nearest-neighbor hopping in graphene. *Phys. Rev. B*, 88:165427, 2013.

[87] S. Szunerits, N. Maalouli, E. Wijaya, J.-P. Vilcot, and R. Boukherroub. Recent advances in the development of graphene-based surface plasmon resonance (spr) interfaces. *Anal. Bioanal. Chem.*, 405:1435, 2013.

[88] J. G. Champlain. A first principles theoretical examination of graphene-based field effect transistors. *J. Appl. Phys.*, 109:084515, 2011.

[89] F. Chen, Q. Qing, J. Xia, J. Li, and N. Tao. Electrochemical gate-controlled charge transport in graphene in ionic liquid and aqueous solution. *J. Am. Chem. Soc.*, 131:9908, 2009.

[90] P. K. Ang, S. Wang, Q. Bao, J. T. L. Thong, and K. P. Loh. High-throughput synthesis of graphene by intercalation-exfoliation of graphite oxide and study of ionic screening in graphene transistor. *ACS Nano*, 3:3587, 2009.

[91] Y. Wu and M. A. Shannon. Theoretical analysis of the effect of static charges in silicon-based dielectric thin films on micro- to nanoscale electrostatic actuation. *J. Micromech. Microeng.*, 14:989, 2004.

[92] A. Deshpande, W. Bao, Z. Zhao, C. N. Lau, and B. J. LeRoy. Imaging charge density fluctuations in graphene using coulomb blockade spectroscopy. *Phys. Rev. B*, 83:155409, 2011.

[93] A. Castellanos-Gomez, R. H. M. Smit, N. Agrait, and G. Rubio-Bollinger. Spatially resolved electronic inhomogeneities of graphene due to subsurface charges. *Carbon*, 50:932, 2012.

[94] E. Rossi Q. Li, E. H. Hwang and S. Das Sarma. *Phys. Rev. Lett.*, 107:156601, 2011.

[95] J. Yan and M. S. Fuhrer. Temperature dependence of conductivity in graphene. *Phys. Rev. Lett.*, 107:206601, 2011.

[96] A. K. M. Newaz, Y. S. Puzyrev, B. Wang, S. T. Pantelides, and K. I. Bolotin. Probing charge scattering mechanisms in suspended graphene by varying its dielectric environment. *Nat. Commun.*, 3:734, 2012.

[97] I. Radovic, L. J. Hadzievski, and Z. L. Mišković. Polarization of supported graphene by slowly moving charges. *Phys. Rev. B*, 77:075428, 2008.

[98] T. Iwaki, C.-Y. Shew, and G. Gumbs. The effect of salt concentration on the optical modes of charged cylindrical nanotubes. *J. Appl. Phys.*, 97:124307, 2005.

[99] M. Jablan, H. Buljan, and M. Soljacic. Plasmonics in graphene at infrared frequencies. *Phys. Rev. B*, 80:245435, 2009.

[100] Y. Rosenfeld. Free-energy model for the inhomogeneous hard-sphere fluid in d dimensions: Structure factors for the hard-disk (d =2) mixtures in simple explicit form. *Phys. Rev. A*, 42:5978, 1990.

[101] J.-P. Hansen and I. McDonald. *Theory of Simple Liquids*. Academic, London, 1986.

[102] C. H. Mak. Large-scale simulations of the two-dimensional melting of hard disks. *Phys. Rev. E*, 73:065104(R), 2006.

[103] X. Guoa and U. Riebel. Theoretical direct correlation function for two-dimensional fluids of monodisperse hard spheres. *J. Chem. Phys.*, 125:144504, 2006.

[104] D. J. Mowbray, Z. L. Mišković, and F. O. Goodman. Ion interactions with carbon nanotubes in dielectric media. *Phys. Rev. B*, 74:195435, 2006.

[105] R. R. Netz. Debye-Hückel theory for slab geometries. *Eur. Phys. J. E*, 3:131, 2000.